VIBRATION CHARACTERIZATION AND NUMERICAL MODELING OF A PNEUMATIC IMPACT HAMMER

Rahul Kadam

Thesis submitted to the faculty of the Virginia Polytechnic Institute and State University in partial fulfillment of the requirements for the degree of

Master of Science

in

Mechanical Engineering

Approved:

Dr. Martin E. Johnson (Committee Chair)

Dr. Ricardo A. Burdisso

Dr. Daniel J. Inman

July 20, 2006

Blacksburg, Virginia

Keywords: Pneumatic Impact Hammer, Numerical Modeling, Vibration and Acoustic Characterization, State-space Modeling, Hand Transmitted Vibrations

Vibration Characterization and Numerical Modeling of a Pneumatic Impact Hammer

Rahul Kadam

ABSTRACT

Hand transmitted vibration (HTV) is one of the most common hazards faced by workers in the construction industry. A major source of HTV is hand held percussion tools, such as pneumatically driven chipping hammers and rock drills. This thesis presents a new approach to measuring the vibration from these tools using an experimental hand arm model to which the tools are attached. The experimental hand-arm model has been designed to have similar dynamic characteristics to that of a human hand-arm system. This approach addresses the issue of repeatability as HTV measurements suffer from variability between cases. The measured acceleration of the hand-arm system is in range or close to range of the measured accelerations of the test subjects with superior repeatability. Further, the thesis presents a nonlinear numerical model of a pneumatic impact hammer. Fundamentally, the numerical model was made up of two different sub-models, 1) a fluid flow model and 2) a structural dynamic model. The fluid flow model was based on the equations for mass flow rate of air though a bleed orifice assuming an isentropic process. The second sub-model deals with modeling the structural components of the impact hammer consisting of the major hammer like the center body, handle, piston and chisel as well as the human hand and the ground. Time domain simulations of the hammer were carried out by using a state space formulation to get displacements, velocities and accelerations of the each component as well as the exhaust jet velocities. Experiments were carried out to measure the handle response and exhaust jet velocities as well as pressure profiles. The results obtained from the numerical model were then validated using these experimental results. Finally, a

parametric study using the numerical model was carried out to explore different vibration control techniques.

Acknowledgements

I would like to thank my advisor, Dr. Marty Johnson, who has given me the opportunity to work on this project. I appreciate the many hours you have willingly given to me. Thank you also for providing me excellent guidance; offering insight on test results and helping me solve problems as they came up. Much of the credit for this work goes to you.

I would like to thank Dr. Ricardo Burdisso for your knowledge, enthusiasm, encouragement and time. Your guidance and suggestions are invaluable to my research work. I would also like to thank Dr. Daniel Inman for your willingness to serve on my committee. Thanks also to Dr. Mary Kasarda for agreeing to attend my defense in place of Dr. Daniel Inman.

I would like to thank you to Dr. James Carneal for helping me on numerous occasions. There were several others who assisted in the work, and to whom thanks are due: Kyle Schwartz, Kiran Konde and Jorge Muract for your help and support throughout. Thanks also to all of my VAL friends and support staff who provided me an excellent and friendly work environment.

In addition, I would like to thank my mom and dad. Your never-ending prayers and support have helped keep me going throughout this entire process.

Table of Contents

List of Figures

List of Tables

Nomenclature

m_{hd}	Mass of operator hand
m_{hdl}	Mass of tool handle
m_{cb}	Mass of center body
m_{pst}	Mass of piston
m_{ch}	Mass of chisel
k_{hd}	Stiffness of human hand-arm system
k_{hd_hdl}	Stiffness between hand and tool-handle
k_{hdl_cb}	Stiffness between tool-handle and center body
k_{cb_ch}	Stiffness between center body and chisel
k_{ch_gd}	Stiffness between chisel and ground
k_{imp_high}	Stiffness for impact between piston and center body
k_{imp_low}	Stiffness for impact between piston and chisel
c_{hd}	Damping ratio of human hand
c_{hd_hdl}	Damping ratio between hand and tool-handle
c_{hdl_cb}	Damping ratio between tool-handle and center body
c_{cb_ch}	Damping ratio between center body and chisel
c_{chi_gd}	Damping ratio between chisel and ground
$c_{friction}$	Damping ratio due to friction between piston and center body
$\dot{m}$	Mass flow rate, m/s
C	Discharge coefficient (dimensionless, usually about 0.65 to 0.72)
A	Discharge hole area, m^2

g_c	Gravitational conversion factor of 1 kg m / N-s^2
γ	Specific heat ratio of the air =1.4 (specific heat at constant pressure) / (specific heat at constant volume)
ρ	Air density, kg/ m^3
M	Air molecular weight =29e-3 kg
R	Universal Gas Law Constant = 1545.3 (ft-lb) / (lbmol) (°K)
T	Gas temperature, °K
Z	Gas compressibility factor at P and T (dimensionless) = 1 for ideal gas
A_{port1}	Area of port1, m^2
A_{port2}	Area of port2, m^2
$A_{exhaust\_port}$	Area of exhaust port, m^2
A	Cross sectional area of control volume
P_u	Absolute upstream pressure, N / m^2
P_d	Absolute downstream pressure, N / m^2
P_{supply}	Absolute supply pressure, N / m^2
P_{atm}	Absolute atmospheric pressure, N / m^2
P_{supply_uc}	Absolute supply pressure to upper chamber, N / m^2
P_{supply_lc}	Absolute supply pressure to lower chamber, N / m^2
P_{uc}	Absolute pressure in upper chamber N / m^2
P_{lc}	Absolute pressure in lower chamber. N / m^2
V_{uc}	Volume of upper chamber, m^3
V_{lc}	Volume of lower chamber, m^3
L	Length of closed volume, m

l_p	Length of the piston, m

Chapter 1. Introduction

In this chapter, a general overview of the thesis is given. The chapter also discusses the objectives and the motivation behind the research and presents a literature review and highlights the author's contribution towards the overall research.

1.1 Summary

The issue of human comfort when faced with machine interaction has acquired a lot of interest in the recent past. Particularly in a severe work environment like construction, human comfort is directly related to operator's health, work efficiency and work quality. Hand transmitted vibration (HTV) is one of the most common hazards faced by workers in the construction industry. A major source of HTV are the hand held impact hammers, such as pneumatically driven impact hammers which include impact hammers, pavement breakers and rock drills. This work primarily consists of two different parts associated with the pneumatic impact hammers. The first part of the thesis deals with the vibration characterization and development of an experimental hand arm rig for the impact hammer. Incidentally, finite element based and experimental modal analysis of the individual hammer components was completed as explained in Chapter 2. Chapter 3 presents a new approach to measuring the vibration from these tools using an experimentally simulated hand-arm rig to which the tools are attached. The simulated rig has been designed to capture the average dynamic characteristics of a human hand-arm system. This approach addresses the issue of repeatability as HTV measurements suffer from variability between cases and from user to user. The performance and repeatability of the tool response for the simulated rig was then compared to the performance and repeatability of the tool response for three

human subjects over a range of preloads. The measured accelerations of the tool for the simulated rig are shown to be representative of the measured accelerations of the tool for the human subjects with superior repeatability. However given the nonlinear nature damping added to the rig, there exists a small degree of uncertainty (of the order of 2 dbA) in the measurements.

Further, the thesis proposes a novel nonlinear numerical model for a pneumatic impact hammer that simulates the structural response, the pressure profiles in different chambers of the tool and the exhaust jet profiles and levels. The model could also be extended to predict the sound radiated from the tool since the sound generated from the impact hammer is a combination sound radiated from the exhaust jet velocities of the tool as well as the structural (impact) noise generated by the tool. The nonlinear numerical model consisted of two sub models; one of them deals with the structural dynamic modeling while the other deals with the time varying forcing input given to the hammer by means of the pneumatic pressure from an external compressor. The model also takes into account the dynamics of the human hand and the ground and their effect on the vibration. Finally a comprehensive parametric study has been carried out on the numerical model in order to explore the various vibration control methods. Although the scope of this thesis is limited to the vibration control, the model can be easily extended to devise new noise control techniques as well. The results of the parametric study are presented in Chapter 5.

1.2 Motivation

As mentioned before, the thesis consists of two different parts; an experimental hand-arm rig and a numerical model of pneumatic impact hammer. The motivation and objectives behind these two different aspects are illustrated below in detail.

1.2.1 Motivation behind the Experimental Hand-Arm Rig

Occupational exposure to hand transmitted vibration (HTV) arises from the hand held powered tools extensively used in the mining and construction industry such as rock drills, impact hammers, chain saws etc. Regular exposure to HTV is the major cause of a range of permanent injuries to human hands and arms which are commonly referred to as hand-arm vibration syndrome (HAVS). Most common hazards include the reduced grip strength and numbness and temperature insensitivity of the fingers better known as vibration white finger (VWF) can be seen from Figure 1- 1. Problems such as cyst formation in the carpal bones, tennis elbow, pitcher's shoulder etc. can also result in the hand-arm. Some minor problems like numbness, pain, loss of grip and touch can occur in the fingers [15].

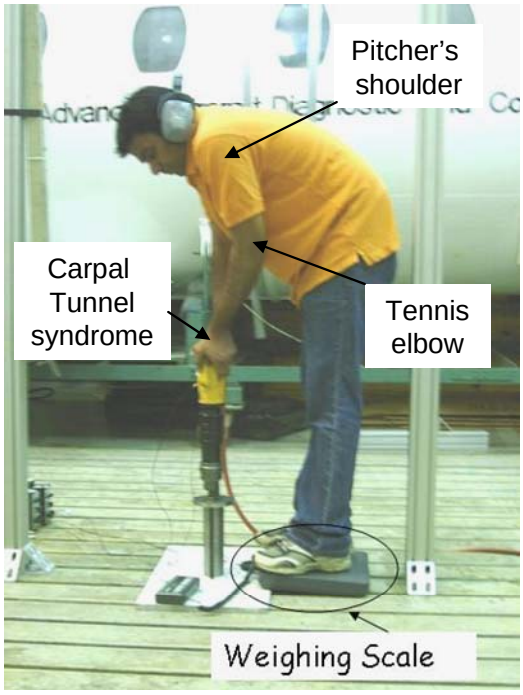

Figure 1- 1: Effects of HTV on human hand and arm Error! Reference source not found.

A human hand is very complex biological system consisting of number of different elements. The layers of skin, nervous system, muscles and bones are found to be the most

susceptible parts to the HTV. In the past, a large amount of research has been carried out by many investigators to measure the acceleration levels of the pneumatic impact hammers. They also took a number of human subjects' tests. However the problem with the human test is the repeatability of the tests results given the nonlinear nature of the human hand-arm system. The response of the tool depends on various factors such as grip force, push force, position of the hand-arm etc. while the operator is holding the tool. ISO 8662-2 defines the procedure for the human tests [28]. As per the standards, the tests should include three skilled operators. Each operator should perform five test runs on the energy absorber. Each test should be carried not less than 8 seconds. It is clear that the whole procedure to carry out the human test is cumbersome and takes lot of time. Arranging for the three skilled operators could a problem to conduct the test each time. Dong et al [14] reevaluated the standards in 2003 and concluded that the vibration responses of the impact hammers do vary with the operators.

The principal objective of this part of the thesis was to address these issues. Therefore it was decided to develop, build and test an experimental rig which could simulate the average dynamics of the hand-arm system while operating the hammer drill. The rig could be used to carry out the vibration tests and measure the vibration levels generated by the tools. Also, the rig should respond in the same way for the different preload conditions as that of the human subjects. However the rig performance needs to be dependable in terms of the repeatability of the results. Consequently, a mechanical rig was designed and built. The impact hammer tool was mounted on the rig and extensive vibration tests were carried out to validate the performance of the rig. The rig was tested for different preload conditions.

Similar tests were carried out on three human subjects. The response of the tool for the rig was compared to that for human subjects on various parameters.

1.2.2 Motivation behind the Development of Numerical Model of the Pneumatic Impact Hammer

The pneumatic impact hammers are very complex and compact machines consisting of large number of hardened steel parts. Given this background, the objectives behind numerically modeling the impact hammer was to be able to test various vibration and noise control techniques numerically and then evaluate their performance by comparing with respect to each other in order to choose the best possible techniques. The best possible techniques can then be physically tested on the impact hammer. Thus the numerical model would help reduce the need to conduct extensive laboratory tests which are both time consuming and laborious. The model would also help to better understand the contribution of each component towards the dynamics of the process which otherwise would not be possible. In addition to this, the numerical model can be utilized to optimize the impact hammer process in order to reduce the vibration and noise levels reductions.

1.3 Literature Review

A large amount of research has been done in the area of the hand transmitted vibrations. Researchers investigated various aspects such as medical, epidemiological and analytical models of the hand-arm. In addition to this, the attempts to build the analytical models of the pneumatic impact hammer were also studied. An extensive literature search on the research carried out in this area has been done and a detailed account is presented here.

1.3.1 Medical and Physiological Studies of the Hand Transmitted Vibrations

G Jancik[8] studied the effect of long term use of hand held power tool vibrations on blood circulation. Jancik thought that the vibration exposure due to pneumatic power tools led to constricted blood supply only in certain ranges. For example vibration around 700 Hz led to blood disturbances whereas vibration around 2000 Hz didn't. Koradecka [10] examined blood circulation changes under the influence of occupational exposure to HTV in different human groups. According to Koradecka, in the context of the blood flow the construction industry worker's reaction to the vibration stimuli was much less as compared to the healthy human subjects. In a similar study, Nerem [11] concluded that the changes in the blood flow in the workers may be due to one of two different factors, increased friction of the arterial wall to the blood flow and the pressure pulsation of the vibrating tool. Louda et al. [13] studied the hygienic aspects of the occupational hand-arm vibration.

1.3.2 Epidemiological Aspects of Hand-Arm Vibrations

Taylor et al. [17] studied the Raynuad's phenomenon in a group of chain saw operators (44-46) over the length of 5 years. Raynaud's phenomenon is a disorder that affects the blood vessels in the fingers. According to Taylor et al. the prevalence of Raynaud's phenomenon was decreased from 85% to 73% by the use of anti-vibration chain saws. Lindstorm [18] studied the vibration injuries in the operators using rock drills and grinders. Lindstorm maintained that the energy absorbed per unit time by the operator was correlated to the injury frequency. In a similar study Refalski et al. [19] reported occurrence of the vibration related disease in the 26.9% of all motor saw operators studied by him. Refalski concluded that the occurrence of vibration disease in the operator were dependent on the factors like

age, number of years of employment etc. Leonida [20] compared the effect of HTV on impact hammer operators versus grinder operators. Leonida observed that the occurrence of VWF in the impact hammer operators is greater than that of grinder operators.

1.3.3 Vibration Test Measurements

Reynolds [20] studied the factors influencing the individual operators' subjective response to the HTV. Reynolds thought that there was a questionable creditability in respect to using the subjective response data in order to evaluate hazardous hand-transmissibility criteria. Reynolds also inferred that the vibration above 100 Hz were also partly responsible for the HAVS. Miwa presented the threshold, unpleasant, and tolerance limit levels for hand transmitted vibration in terms of accelerations. Hempstock et al. [22] studied the difficulties involved in measuring the hand transmitted vibrations. Hempstock et al. also evaluated various available standards. Hempstock et al. pointed out that it was necessary to carry out a sufficient number of sample tests when the time duration of the vibration exposure was not certain. Suggs et al. [4] proposed 3-DOF analytical model of the hand arm system based on the measured hand impedance data. Suggs et al. suggested that the energy absorption increases with the frequency. Suggs et al. concluded that reduced transmissibility at higher frequencies was due to the power absorption near the area of input. Frood [25] studied the test methods and the problems involved in measuring the vibration of hand-held pneumatics tools such as grinders and impact hammers. Frood suggested use of mechanical filters to avoid the DC shifts and also advice to continuously observe the acceleration levels.

1.3.4 Analytical Models of the Human Hand

Over the years, different investigators had proposed different mathematical models for the hand-arm system. Most of them were lumped mass approximation models. These varied from single DOF to multiple DOF. Abrams [27] proposed a single DOF model lumped-mass model for each of he three orthogonal axes. The frequency range of the study was 70 Hz to 1650 Hz. Reynolds [20] developed a mathematical 3-DOF model of the hand-arm system with three lumped masses. Each mass of model represented a particular part of the hand skin like dermis and subcutaneous tissues and muscle tissues. Reynolds compared his model with the experimental data obtained from the human subjects' tests. Reynolds observed that the below 100 Hz the energy dissipated in the fingers and hand. All the vibration energy above 100 Hz was stored in epidermis, dermis and subcutaneous tissues. Suggs et al. [4] proposed 3-DOF analytical model of the hand arm system based on the measured hand impedance data. Reynolds et al. [2] improved the 3-DOF hand-arm model to 4-DOF hand-arm model. An additional DOF was assigned for epidermis between the dermis and subcutaneous tissues. Reynolds et al. also suggested that different single DOF models could be used for different frequency ranges to fit the hand impedance data. So Reynolds et al. divided 20-500 Hz frequency range at 73 Hz. Wood et al [24] proposed a distributed parameter model for the hand arm system. Further a 6-DOF model was developed by Reynolds et al [6] in which every 2-DOF were assigned to each of the three diagonal axes. Fritz [1] proposed a very different 4-DOF model of the hand-arm system as compared to the 4-DOF model proposed be Reynolds [2]. In this particular model, the four degrees of freedom were interpreted as fingers, palm, forearm, and shoulder-arm. There were two main approaches followed by investigator to characterize the HTV. Some of them measured the transfer function between the driving

point and other locations on the hand arm system [3, 4] while others measured the driving point accelerations and force to calculate the driving point mechanical impedance [2, 5, 6]. They compared the human subject test data to the results obtained from the corresponding analytical models for validation

1.3.5 Numerical Modeling of a Pneumatic Impact Hammer

Pang, Goldsmith et al (1992) [31] developed a model for pneumatic impact hammer. However the model was a combination of experimental results and an analytical model. S. S. Pang, W. Goldsmith et al measured the pressure build up in the different chambers of the pneumatic hammer experimentally and then used these results in the numerical model. This is the biggest limitation of the model i.e. on every occasion it is required to experimentally measure the chambers' pressures. Apart from that drilling holes in the body of the impact hammer can be very expensive and difficult thing.

Golycheva, Babitsky (2003) [33] proposed a lumped-mass approximation model for 'electro-pneumatically' driven impact model. For the model development in this thesis, the idea of modeling the impact hammer as a lumped mass model is taken from their work. However their model is fundamentally different from the model developed here with regard to the calculation of the time varying forcing input given to the impact hammer. In their case, the forcing is calculated by using kinematical equation of the crank and connecting rod.

Wang, Singh,(1984) [34] proposed a numerical model of a shock absorbing pneumatic cylinder which calculates the pressure build up inside the pneumatic cylinder chambers using equations of isentropic mass flow rates through a bleed orifice. This paper forms the basis for the fluid flow model for the pneumatic impact hammer model. However the

hammer model has 12 exhaust ports and a pneumatic valve which weren't there in the pneumatic cylinder model.

1.3.6 Vibration Control of a Pneumatic Impact Hammer

Vibration control of pneumatic impact hammers has become an important research topic in recent years. Researchers have used different techniques to control the vibration levels. Miwa et al (1979) [36] worked on the rock drill machines. Miwa tried to isolate the rock drill handle from the rest of the body by using rubber bearings in the handle. He also developed a prototype using the above technique. However the use of a rubber bearing resulted in the loss of the control at the operator's hand. To effectively control these vibrations the vibration isolators need be tuned to the impact frequency of the hammer. In addition to that this method is difficult to implement in the actual tools. Strydom (2002)[37] et al. worked on the rock drill vibration control. They used the liquid inertia dampers where used to isolate the handle from the main drill body. They also developed a prototype using liquid inertia dampers. However durability of these dampers remains a concern given the fact that the rock drills create huge amount of forces and operate in rough working conditions. Besides this the dampers do not offer tuning to varying impact frequency and they are difficult to implement. Oddo, Loyau (2004) [38] isolated the rock drill handle by using the helical spring and visco-elastic mounts and also the developed a prototype. However the implementation of these methods remains a worry because of the size of the helical springs and fragility of the rubber bearings. Also the tuning of the helical spring and visco-elastic mounts is questionable.

Prajapati et al (2002) [39] developed a prototype of vibration damping handle by means of the addition of visco-elastic material to dampen the vibrations and actually tested the prototype

on the tools. The main disadvantage was that the method was effective above 100 Hz. Attala et al (2002)[40] researched a commercially available chisel which can reduce vibration levels. He concluded that these chisels are found ineffective as far as vibration reduction was concerned. Many researchers such as Griffin (1990)[15] have worked on developing vibration protective hand gloves. It has been found that the gloves are not useful for the low frequency vibrations (<200Hz) which are most hazardous in this case. These anti-vibration gloves are commercially available in the market.

1.3.7 Frequency Weighting for Hand-Arm Vibration

ISO 5349 [29] specifies general requirements for measuring and reporting hand transmitted vibration exposure in three orthogonal axes. It also defines a frequency weighting band limiting filters to allow uniform comparison of measurements. The values predict adverse effects of hand transmitted vibration over the frequency range covered by the octave bands from 8 Hz to 1000 Hz. The weighting is based on the premise that the low frequency causes the maximum damage to the hand-arm system. According to the weighting the maximum effect of the vibration is realized at 6-8 Hz. However the weighting has been in question recently with some investigators[16] arguing that there should be separate weightings for the fingers and for the rest of the hand-arm. But for the purpose of the study, ISO 5349 frequency weighting has been used to measure the effective hand-arm vibration.

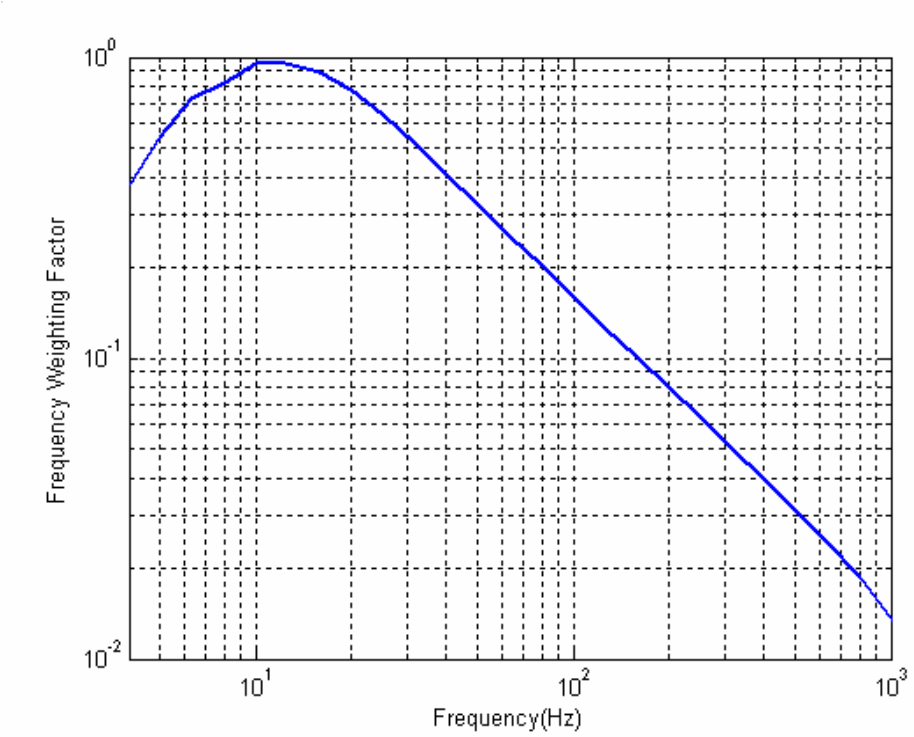

Figure 1- 2 : Frequency weighting for hand-arm vibration

1.4 Contributions

This section lists the author's contributions in the overall research.

1) The set-up for the experimental hand-arm rig was developed and built successfully in the laboratory to capture the average hand-arm dynamics (along with Jorge Muract).
2) Vibration characterization of the pneumatic impact hammer was completed using experimental modal analysis, finite element modeling and acceleration measurements on a running tool (along with Jorge Muract).
3) Experiment hand-arm rig was validated using human tests' results on a range of different criteria (along with Jorge Muract).

4) Time history tracking analysis of the impact hammer's operation was performed using hot-film measurement and accelerometer measurements to better understand hammer working process.
5) A novel nonlinear numerical model for a pneumatic impact hammer was formulated to simulate structural response and fluid flow process in the pneumatic impact hammer. The model can also be used to predict the sound radiated from the impact hammer. This model is being used to develop the vibration and noise control techniques.
6) The mathematical model of the hammer was validated using hot-film and chisel accelerometer measurements.
7) Various possible vibration control techniques were explored using the numerical model.

Chapter 2. Vibration Characterization and Time History Tracking of a Pneumatic Impact Hammer Operation

In this chapter, a general introduction to the pneumatic impact hammers and its operational aspects are given. The chapter presents a novel methodology used to comprehend the underlying principles of the operation of the tools and explains the experiments carried in order to achieve this. The modern power-driven impact hammers have been in use for more than a hundred years. Impact hammers are used in the construction, mining industry etc. for different purposes such as breaking pavements, drilling rocks, removing rust layers on metals etc. These tools can be hydraulically driven, pneumatically driven or electrically driven. The impact hammers used in conjunction with this work are commercially available, pneumatically driven impact hammers, manufactured by Atlas Copco and Ingersoll-Rand. Figure 2- 1 and Figure 2- 2 shows some of the tools donated to Virginia Tech and available for the testing. All of these hammers work on the same principle.

(a) **(b)** **(c)**

Figure 2- 1: Ingersoll-Rand pneumatic impact hammers, (a) Impact hammer, (b) Pavement breaker and (c) Rock drill

(a) **(b)** **(c)**

Figure 2- 2 : Atlas Copco pneumatic impact hammers, (a) Impact hammer, (b) Pavement breaker and (c) Rock drill

2.1. Principle of Operation of a Pneumatic Impact Hammer

This section explains the general configuration and the principle of operation of a general pneumatically driven impact hammer. Since this thesis work is based on a particular Atlas Copco impact (chipping) hammer –Tex 317, the specifications of the hammer are also provided here.

2.1.1. General Pneumatically Driven Impact Hammer

The main pneumatic impact hammer components are the handle, the center body, the piston and the chisel. Figure 2- 3 shows a schematic of the impact hammer. The impact hammer has many other smaller parts which are used to assemble the major components. The center body has a cylindrical bore inside it which runs through its length. A piston fits inside the bore and is free to move up and down impacting the chisel at the bottom of its stroke. The handle is screwed on to the top of the center body. The compressed air required to operate the hammer is supplied to the hammer through a connection at the top of the machine. The machine has a pneumatic valve that is situated between the handle and center body that is used to regulate the air supply either to the chamber above the piston or the chamber below

the piston. The pressure in both chambers change continuously as the piston moves up and down. There is exhaust ports drilled at two positions (six each at one position) into the center body. All of them have equal dimensions and they are equally spaced around the circumference of the center body. The dotted lines in the center body (Figure 2- 3) indicate the exact positions of the exhaust ports as in the actual hammer (Atlas –Copco impact hammer Figure 2- 2 (a)). The chisel shank sits in the tapered portion of the center body. It is fixed to the body by means of an oval retainer not shown in the schematic. Opening of the exhaust ports to atmospheric pressures allows the air in the chambers to be released, changing the pressure in turn forcing the piston.

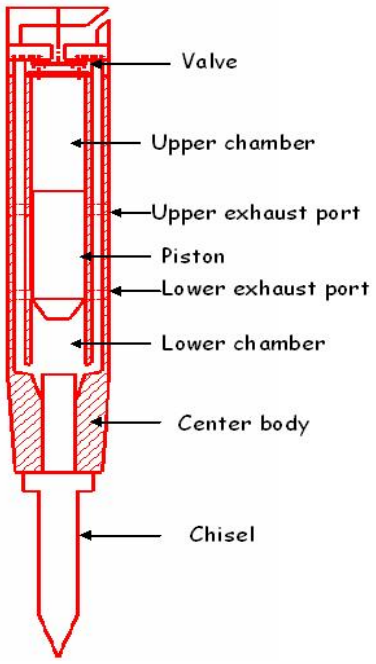

Figure 2- 3: Schematic of the impact hammer

2.1.2. Atlas Copco TEX-317 Chipping Hammer

The components of the Atlas Copco impact hammer can each be seen in Figure 2- 4 and the specifications of the hammer are given in the Table 2 - 1. The dimensions of the chisels can

be seen in Figure A- 1. In these tests, the impact hammer was operated by a supply pressure of 90 psi and the piston impacts the chisel at a rate of approximately 2200 beats per minute. This impact rate can vary depending on the supply pressure. A rubber sleeve, with two holes, is installed on the center body blocking the original 12 exhaust ports. This rubber sleeve can be positioned to either block all 12 holes or exposes two holes. For clarification, Figure 2- 5 (c) shows the rubber sleeve in the position which exposes two of the original exhaust ports. It was also observed that the rubber sleeve rotates during operation of the impact hammer.

Table 2 - 1: Specification of the Atlas-Copco Tex 317

Specifications
– Net weight 6.4 kg – Length 387 mm – Stroke 102 mm – Air consumption 31.5 cfm

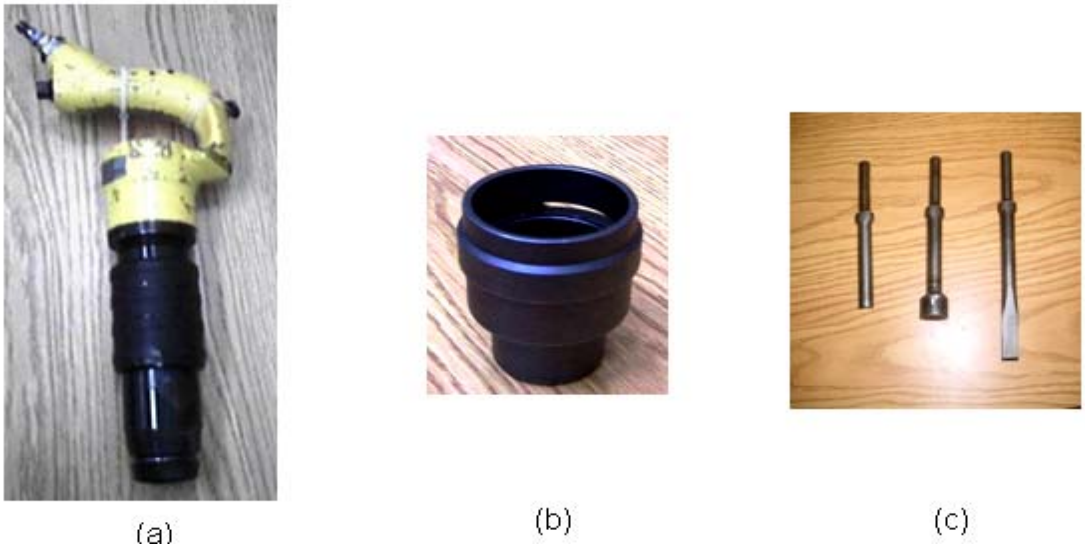

Figure 2- 4: (a) Center body and handle of the impact hammer. (b) Oval retainer and (c) the truncated, modified and taper chisel

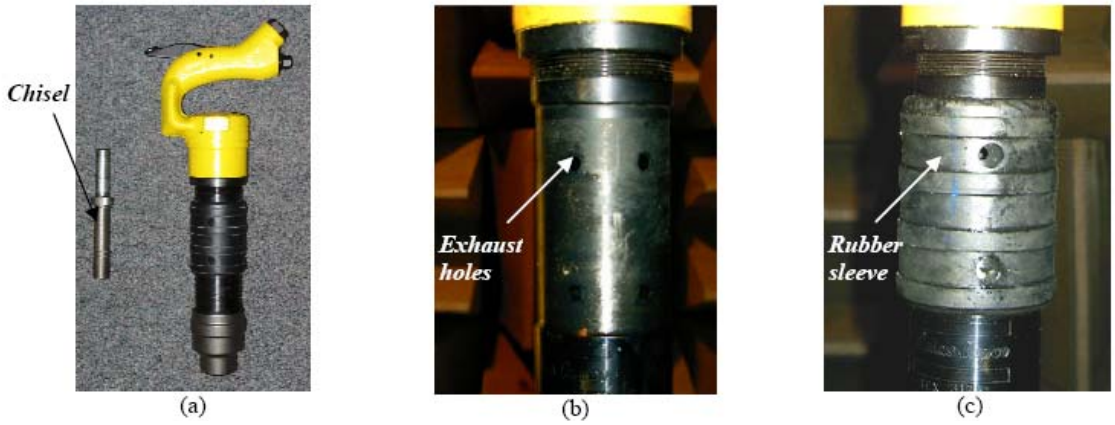

Figure 2- 5 : (a) Impact hammer (b) without sleeve and (c) with rubber sleeve

2.2. Time History Tracking of the Impact Hammer Operation

The impact hammer components were drawn to scale in order to map out the piston movement with respect to the exhaust ports and chisel positions. These dimensions were later used in the numerical model. Here, one complete cycle of the piston from an impact to the subsequent impact is analyzed. Generally this type of hammers run at around 30 Hz, therefore one cycle of piston takes around 0.03 seconds. There are many events which happen during one cycle of the piston such as the impact between the chisel and piston, opening and closing of the upper exhaust ports and openings and closing of the lower exhaust ports due to the moving piston. All these events happen in a particular sequence. Therefore, it was important to know the exact and relative timings of opening and closing of the upper and lower exhaust ports and the impact between chisel and piston during a cycle. The opening or closing of the exhaust ports would produce very sharp changes in the exhaust jet velocities and therefore measuring these velocities would tell the exact time of closing and opening of the exhaust ports.

2.2.1. Exhaust Jet Velocity Measurements using the Hot Film Anemometer

Initially, pressure probes were used to measure the velocity of the exhaust exit flow and found to be difficult due to signal processing issues. The alternative to the pressure probes was to directly measure the velocity through hot wire anemometry. Hot wire anemometry is able to provide accurate measurements of the instantaneous fluid velocity. The hot wire transducer was setup with a DANTEC type 55M01 power supply. The hot wire was calibrated with a TSI calibrator model 1125 as shown in Figure 2- 6 a and b. This work is explained in detail by Schwartz [41].

(a) (b)

Figure 2- 6 : a) Power supply used to power and regulate the hot wire anemometer b) TSI Calibrator model 1125 used to calibrate the output of the hot wire anemometer.

As shown in Figure 2- 7, the velocity measurements were performed in a vibration isolation rig so that the movement of the body was negligible. The hot wire transducer was placed horizontal to the ground and perpendicular to the tool and was always parallel to the measured exhaust port. Measurements were taken at 4 radial positions as well as 11 to 16 angular or tangential positions for both the upper and lower exhaust ports. Spatial measurement location error was ±0.1mm. The measurements described in this paragraph yield a velocity profile in the two dimensional spatial domain as well as in the time domain.

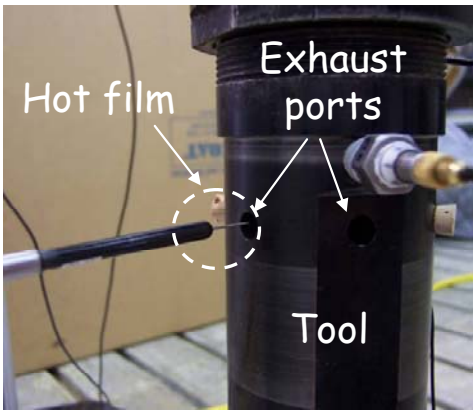

Figure 2- 7: Experimental setup for hot wire anemometer measurements.

The average of exhaust jet velocity was in this region of 10 to 30 m/s. However, the magnitudes of the jets fall off sharply away from the exhaust orifices implying that the mixing region is relatively small. More useful are the time histories of the exhaust jet velocities as shown in Figure 2- 8. This figure shows the velocity versus time for one operating cycles of the impact hammer for both ports. These signals were time synchronized through an accelerometer attached to the chisel in both measurements.

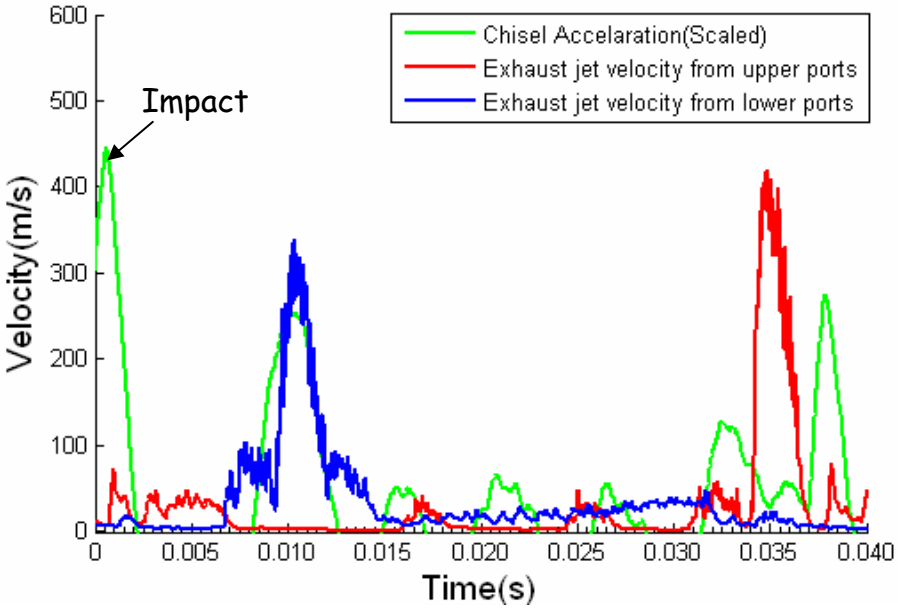

Figure 2- 8: The time variation of velocities for both the low and high port showing velocities that reach Mach 1.0 or greater.

The displacement of the piston at the time of impact was considered as x=0. All other displacements are measured with respect to the impact position. The highest displacement of the piston is 102 mm. A number of CAD drawings of the impact hammer consisting of all the major components were prepared to scale as shown in Figure 2- 9 (a)-(i). Each drawing has the piston in a different position. The specific position of the piston was chosen very carefully by considering the positions of the exhaust ports as will be explained further. The different positions of the piston are cyclic in nature. Figure 2- 10 illustrates the time history tracking operation of the impact hammer from experimental measurements of the exhaust jet velocities from the upper and lower ports and the chisel accelerations. Black vertical markers named as (a)-(i) drawn on Figure 2- 10 validate the operation of the impact hammer as explained below.

Event (a): Impact (x=0)

Impact between the chisel and piston was chosen to be the first event. This was an obvious choice since data from the accelerometers clearly indicate the timings of the impact as can be seen from the instantaneous increase in the chisel accelerations in Figure 2- 10-(a). Secondly the displacement of the piston (displacement at x=0) at the time of impact was also known. Also it was known that the piston moves upward after the impact. Figure 2- 9 (a) shows the position of piston and dynamic fluid flows routing in the impact hammer at the time of impact. At this point the lower exhaust ports are blocked by the piston, therefore the air jet velocity from lower exhaust ports is almost zero. The upper exhaust ports are open to upper chamber, however the pressure in the upper port is slightly more than atmospheric pressure, and therefore only a small amount of air is coming from the upper ports. At this position the air pressure is being supplied to the lower chamber. During

impact, part of kinetic energy of the piston is transferred to the chisel which is then used in the impact process. It should be noted that there is fluid flow leakage around the as shown in Figure 2- 9.

Event (b): Upper exhaust ports close (x=0.035m)

Due to impact the piston is rebounds and starts to move upwards. The supply pressure is still applied to the lower chamber. This high pressure in the lower chamber accelerates the piston in the upward direction. Therefore the piston eventually blocks the upper exhaust ports and the jet velocity through upper exhaust ports drop to zero instantaneously as seen in Figure 2- 10 (b). Figure 2- 9 (b) shows the position of the piston and the corresponding dynamic fluid flow routing. Since the upper exhaust ports get blocked the upper chamber becomes a closed volume. After this point the upward moving piston will compress the air inside upper chamber and therefore increase the pressure. The lower exhaust ports are still blocked by the piston. As a result, the jet velocity through the lower ports remains almost equal to zero.

Event (c): Lower exhaust ports open and pneumatic valve flips to apply pressure to upper chamber (x=0.04m)

Lower exhaust port opens up as the piston moves past it. Since the lower chamber is open to the supply pressure, the pressurized air exhausts through the lower ports very quickly and pressure in lower chamber exponentially decays down to atmospheric pressure. as can be seen from Figure 2- 10 (c) By this time the pressure in the upper chamber already started to increase due upward moving piston as explained earlier. The increase in upper chamber pressure and decrease in the lower chamber pressure causes the pneumatic valve to flip and now the supply pressure gets applied to the upper chamber. The position of the piston and fluid flow routing is explained in Figure 2- 9 (c)

Event (d): Upper exhaust ports open (x=0.09m)

By this time piston has obtained enough momentum that it moves upwards against the supply pressure in the process increasing the pressure in the upper chamber above supply pressure. The upper exhaust valve opens up to the lower chamber releasing very small amount of air to atmosphere as shown in Figure 2- 10 (d). Sometimes the piston may not able to move past the upper ports. Figure 2- 9 (d) graphically represents the position of the piston and flow routing.

Event (e): Piston attains top position and stars to move down

The piston reaches the top position when its velocity goes to zero due to the resistance from increasing supply pressure, friction between piston and center body and gravity. Immediately it starts to move downwards. Figure 2- 10 (e) represents the approximate timing of the piston reaching the top. The upper and lower exhaust ports remain uncovered at this time. The pressure inside the upper chamber reaches the maximum. The experimental results show that the piston never hits the top. Therefore the volume of the upper chamber never goes to zero which allows the pressure values to remain finite although slightly more than the supply pressure. Figure 2- 9 (e) graphically represents the position of the piston and flow routing.

Event (f): Upper exhaust ports close (x=0.09)

The piston accelerates downwards and forces small amount of air out when it passes upper exhaust ports. Then it blocks the upper exhaust ports as shown in Figure 2- 10(f). The lower exhaust ports are still open. The downward moving piston starts to compress the air

gradually in the lower chamber. So there is build up of pressure in the lower chamber. The position of the piston and fluid flow routing is explained in Figure 2- 9 (f).

Event (g): Lower exhaust ports close (x=0.04m)

As the piston moves down the pressure in the lower chamber increases causing more and more air to be released from the lower ports. Finally the lower ports get blocked by the piston and immediately the exhaust jet velocity goes to zero as shown in Figure 2- 10(g). After this point the lower chamber becomes a closed volume. The downward moving piston compresses the air in the chamber and therefore increases the pressure. The upper ports remain blocked during this time. As a result the jet velocity from both ports is almost zero. Figure 2- 9(g) shows the position of the piston and dynamic fluid flow routing at the same time.

Event (h): Upper exhaust ports open and pneumatic valve flips to apply pressure to the lower chamber (x=0.035m)

Pressure at the top of the piston continues to accelerate it downwards. Upper exhaust ports now get uncovered. Therefore the extremely high pressure in the upper chamber gets released to the atmosphere and the air in the chamber charges out with very high velocity. The pressure in the upper chamber then drops to atmospheric instantaneously as seen in Figure 2- 10(h). At this point the pressure in the lower chamber already started to increase rapidly is high due to piston moving at high velocity. This creates a back pressure on the pneumatic valve causing it to flip. Therefore the supply pressure gets applied to the lower chamber. Figure 2- 9 (h) graphically represents the position of the piston and flow routing.

Event (i): Impact (x=0)

By this point the piston attains very high velocity which allows it to overcome the resistance of the high pressure air in lower chamber. Finally it reaches the lowest point in its travel when it hits the chisel. As can be seen from the Figure 2- 9(i), the volume of the lower chamber doesn't go to zero at the time of impact due to the geometry of center body which keeps the pressure in the chamber to finite values.

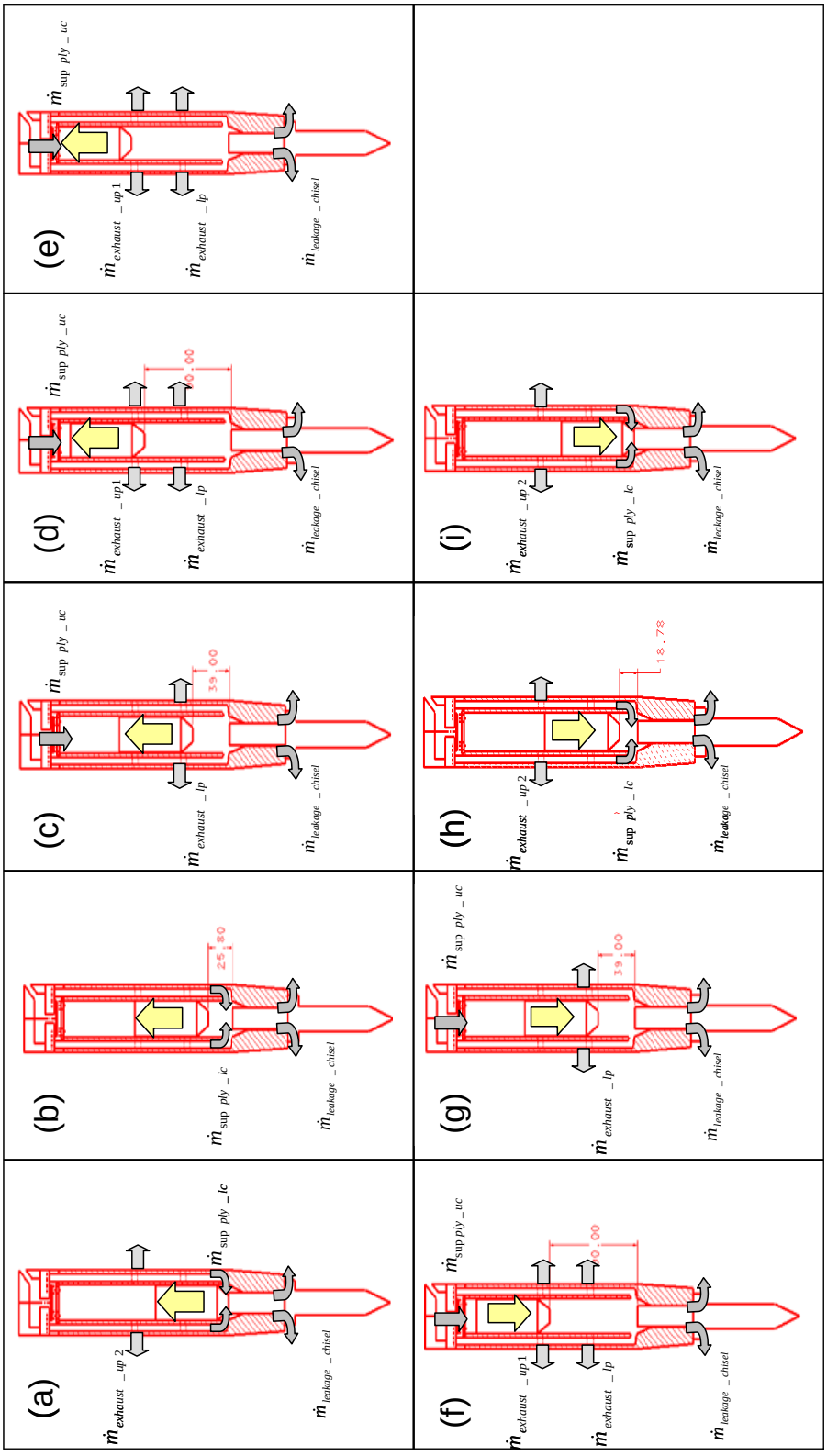

Figure 2- 9 : Impact hammers schematic showing its Time history tracking operation from event (a) to (i) and related fluid flow routing

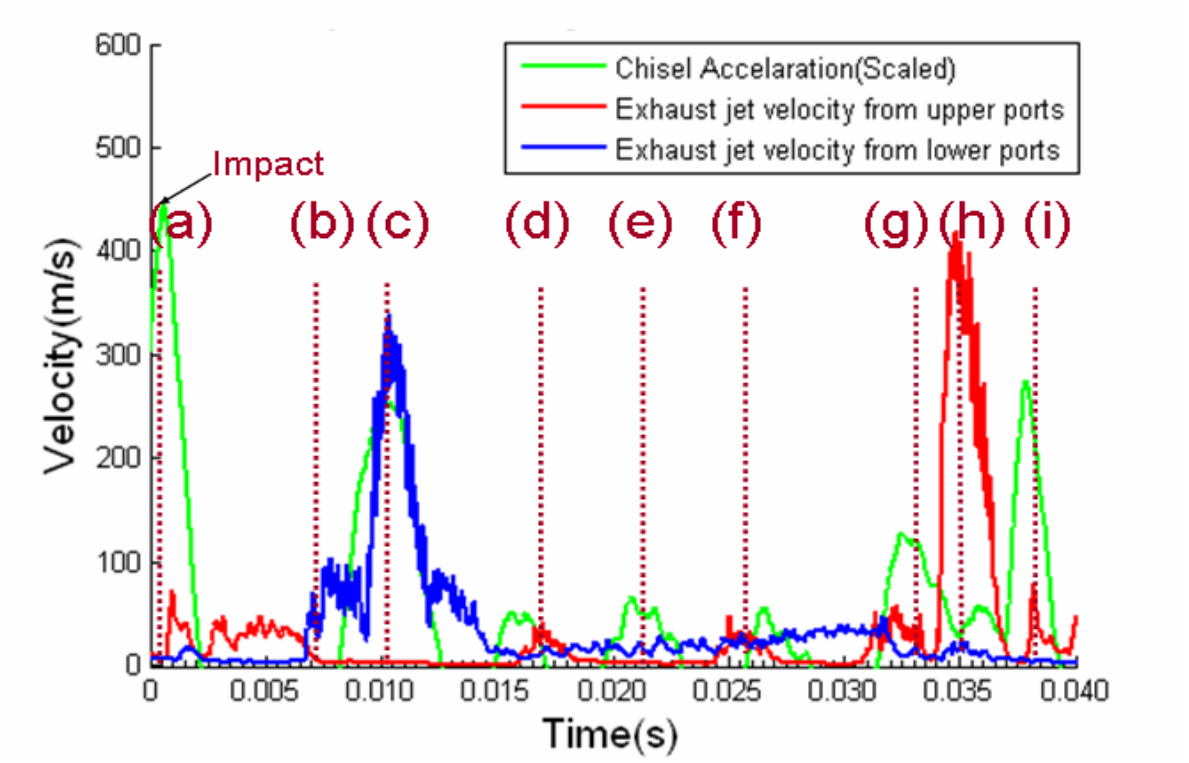

Figure 2- 10: Experimental measurements (exhaust jet velocities and chisel accelerations) of impact hammer showing its Time history tracking operations from event (a) to (i)

2.3. Modal Analysis

Vibration characterization of the dynamic system was the first step towards the ultimate goal of devising the vibration control techniques. Detailed modal analysis determines the fundamental vibration mode shapes and corresponding frequencies. This can be relatively simple for basic components of a simple system, and extremely complicated when qualifying a complex mechanical device or a complicated structure. These systems require accurate determination of natural frequencies and mode shapes using techniques such as Finite Element Analysis. Apart from that the finite element models could be used for the development of the vibration and noise control techniques in future.

2.3.1. Finite Element Based Modal Analysis

The Atlas-Copco impact hammer consists of four major parts, 1) the center body, 2) the handle, 3) the retainer and 4) the chisel. The center body and the handle can be modeled as a single part because in the 0-1000 Hz frequency range, the handle appears to be a small cantilever attached to the large mass (cylinder) of the center body. Finite element model of all the three components, the center body with handle, the chisel and the retainer were developed. The CAD models were built geometrically similar to the actual models in IDEAS and later exported to the ANSYS for modal analysis. Figure 2- 11-a, b, c shows the finite element models of the center body, the retainer and chisel respectively. The modal analyses of each of the models were carried out. The experimental modal analysis results were used to validate the FEM models.

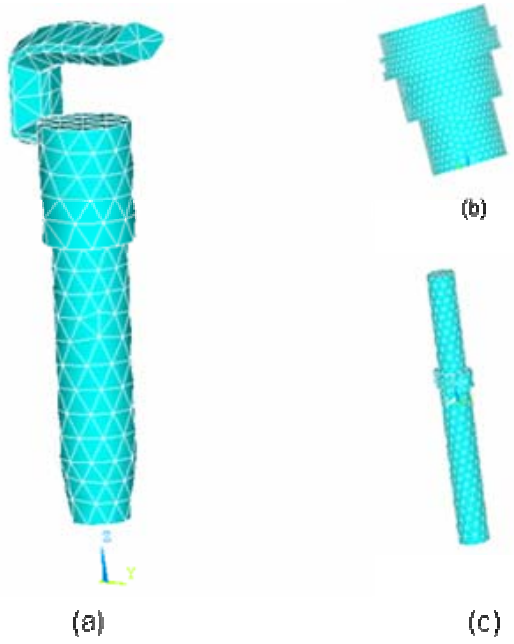

Figure 2- 11 : Finite element models of (a) center body with handle (b) retainer (c) chisel

The results for each individual component are given as following,

Center body

The modal analysis of the model shows that the first and second natural frequency of the handle lies at 574 and 841 Hz as shown in Table 2- 1. Both of these modes are associated with the handle where the operator grips the tool. Therefore their influence on the hand vibration is significant. First mode is the bending of the handle while second is twisting of handle as shown Figure 2- 12-a and Figure 2- 12-b respectively. In the first mode, the handle acts like a cantilever attached to the cylindrical portion of the center body. In the second mode the handle twists about the vertical axis of the tool. Figure 2- 12 (c) and Figure 2- 12 (d) illustrates the next two modes of the center body. These are bending modes of the center body. However the frequency of the both modes was the far greater 1000 Hz and therefore in the context of the hand-arm vibrations they aren't important.

Table 2- 1: FEM natural frequency for center body

Mode	Natural frequency (Hz)
1	574.59
2	841.89
3	1871.3
4	2348.1

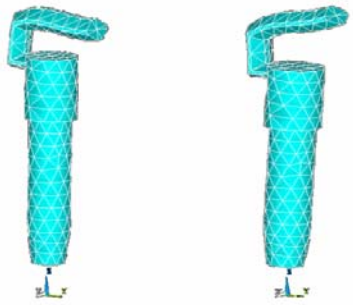

(a)

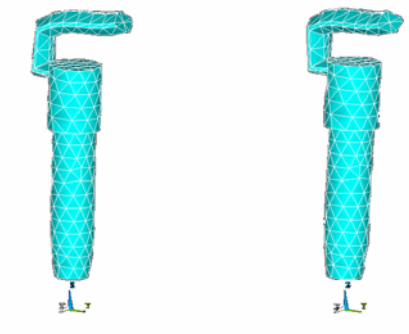

(b)

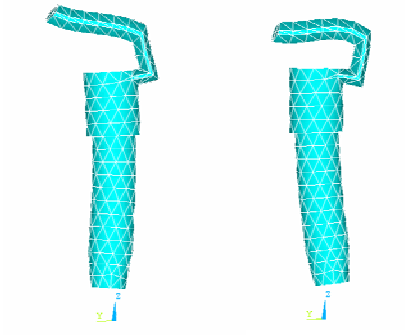

(c)

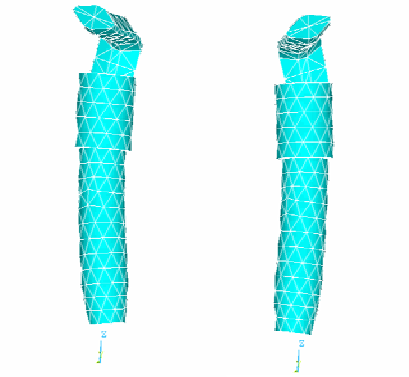

(d)

Figure 2- 12 : Mode shapes of the impact hammer (a) bending mode shape of the handle, (b) twisting mode shape of the handle, (c) and (d) higher bending modes of the impact hammer

Retainer

Table 2- 2 lists the first two FEM modal analysis natural frequencies for the retainer. However the natural frequencies of the chisel are too high (>>1000 Hz) to consider as far as the hand arm vibrations are concerned as discussed previously. The first two mode-shapes are breathing modes as shown in the Figure A- 2 and Figure A- 3 respectively. However

these higher frequencies might be playing an important role as far as structural noise emission is considered.

Table 2- 2: FEM natural frequency for retainer

Mode	FEM (Hz)
1	6072.8
2	6151.8

Chisel

The results for the numerical modal analysis of the chisel model are on the same line as that of the retainer. Table 2- 3 lists the first two FEM natural frequencies for the chisel. Both of the modes are bending modes of the chisel as shown in Figure A- 4 and Figure A- 5. The natural frequencies obtained from the finite element model are far more than 1000 Hz. As mentioned before higher frequencies might be important in the context of the structural noise emission.

Table 2- 3: FEM natural frequency for chisel

Mode No.	Natural frequency (Hz)
1	3210
2	3459

2.3.2. Experimental Modal Analysis of the Pneumatic Impact Hammer Components

Experimental modal analysis of the individual impact hammer components was carried out to validate the natural frequencies obtained from the FEM modal analysis. In this method, an impulse hammer was used to impart sufficient energy in the structure as shown in Figure 2- 13-a, b and c so as to excite it in the frequency range of interest. The frequency range was decided to be 0-1000 Hz since this is the most perceivable vibration frequency range for

human hand-arm system. Vibration frequency weighting factor [29] for 1/3 octave band with center frequency 1000Hz is 0.0135 compared maximum of 0.958 for 1/3 octave band with center frequency 11 Hz. Therefore frequency more than 1000Hz cause no or little effect for the hand-arm system. An accelerometer was attached to the tool handle in the vertical direction as shown in the Figure 2- 13-b. The accelerations was taken in the direction of drilling operation as specified in ISO-8662-2 [28], the vibration levels in the vertical direction are most hazardous as far as the HAVS are concerned whereas the vibration in the other directions can be estimated from the vertical direction vibrations.

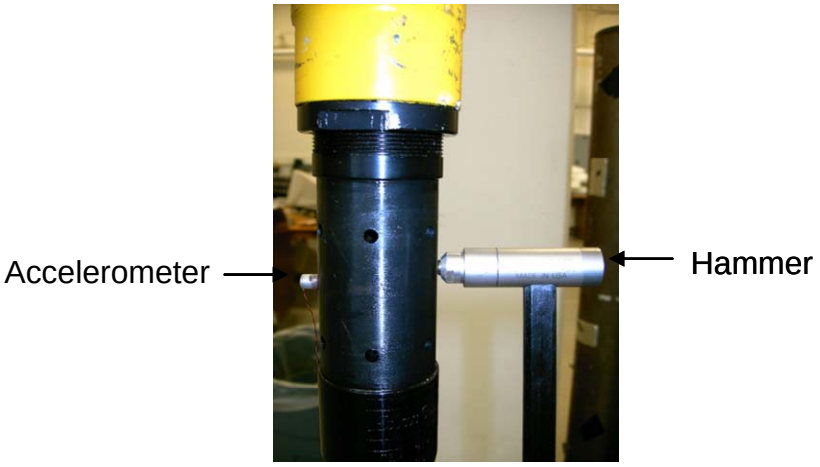

(a)

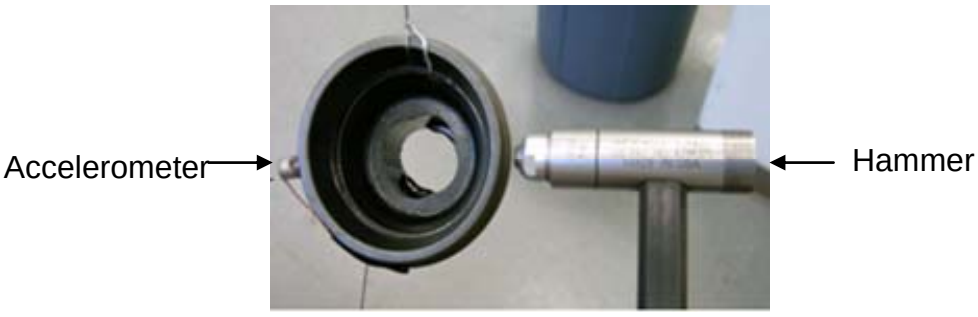

(b)

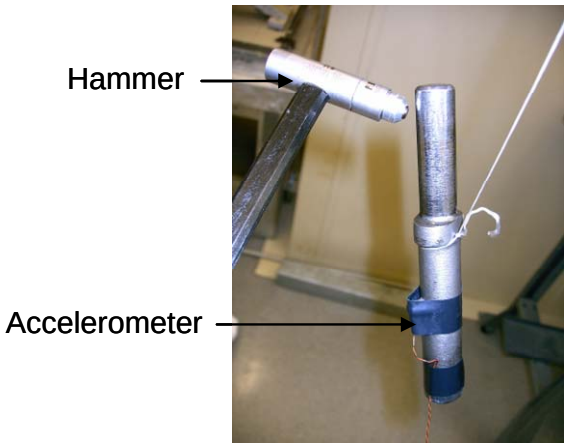

(c)

Figure 2- 13 : Impulse hammer test for (a) center body with handle, (b) retainer and (c) chisel

Following section will discuss particularly the experimental results obtained from the modal analyses of impact hammer components i.e. the center body, retainer and chisel and compare the frequencies with the FEM frequencies. For each of the transfer function result the accompanying picture shows the position of the accelerometer.

Center body

Figure 2- 14 and Figure 2- 16 demonstrate the transfer function of the center body for the accelerometer position shown in Figure 2- 15 and Figure 2- 17 respectively. The modal analysis of the center body at different accelerometer locations were done to explore all the natural frequencies of the center body. For example, in Figure 2- 15 the accelerometer is attached to the handle so it can be safely said that the two resonant frequencies appear in the Figure 2- 14 are associated with the handle. The comparison between the first five natural frequencies of FEM and experimental modal analysis for the center body has been listed in the Table 2- 4. It has been previously mentioned that the frequency range of interest in the context of HAVS is 0-1000 Hz.

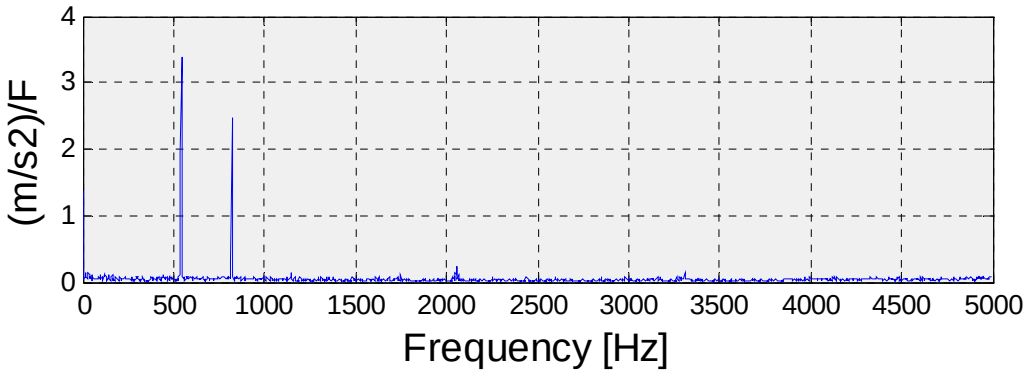

Figure 2- 14 : Transfer function of from the impact location to accelerometer on handle

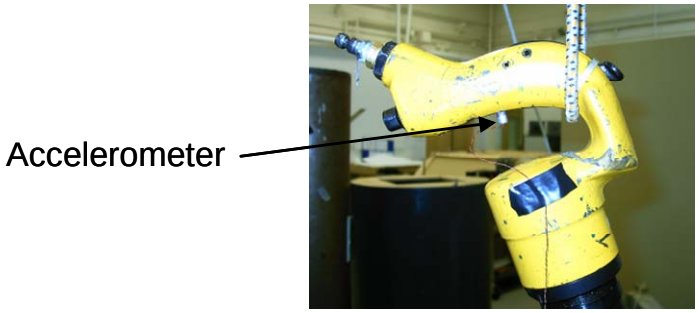

Figure 2- 15 : Modal test of center body with accelerometer at handle

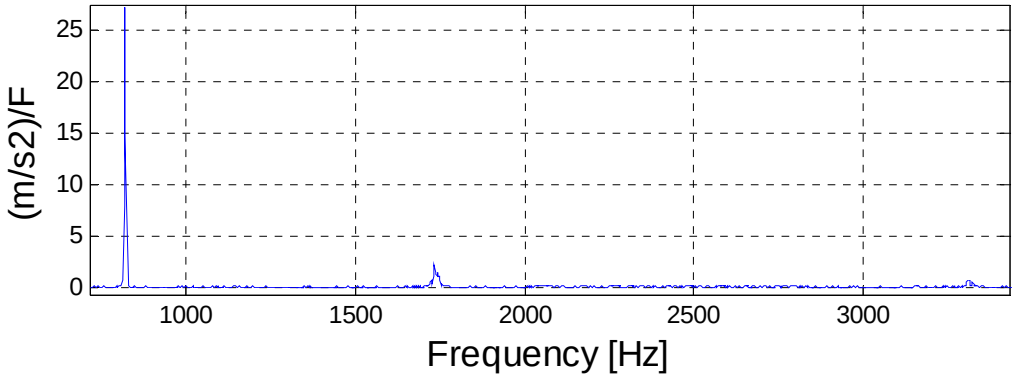

Figure 2- 16 : Transfer function of center body from the impact location to accelerometer on center body (at bottom of body)

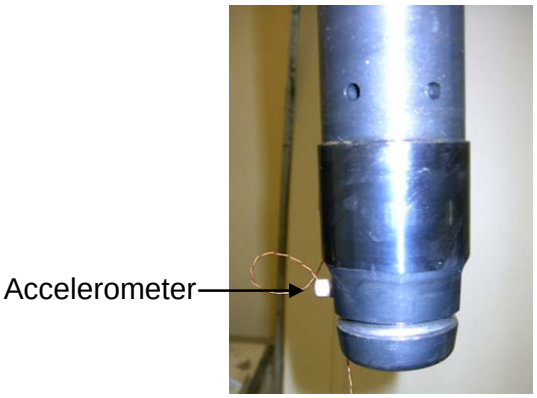

Figure 2- 17: Modal test of center body with accelerometer at bottom

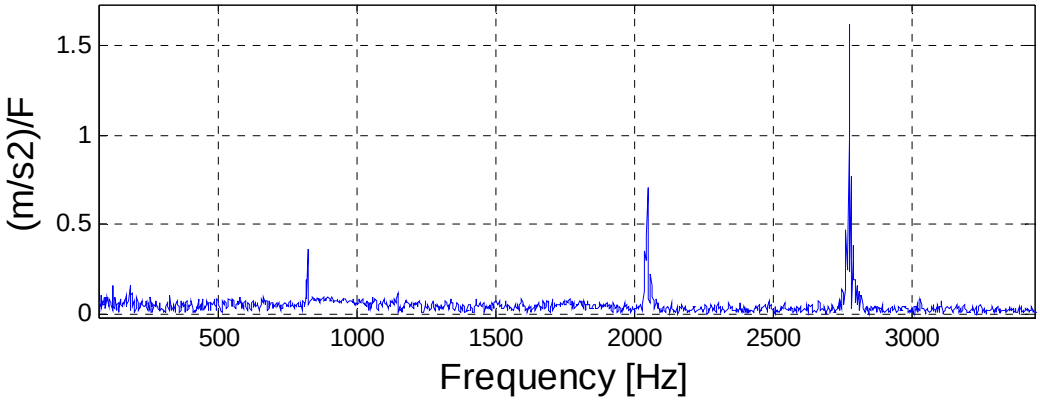

Figure 2- 18: Transfer function of center body from the impact location to accelerometer on the center body (at the middle of body)

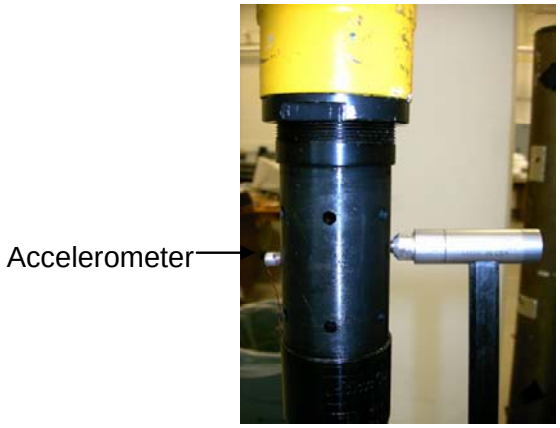

Figure 2- 19: Modal test of center body with accelerometer at the middle

Table 2- 4 : Comparison of fem and experimental modal analysis for center body

Mode	FEM (Hz)	Experiment (Hz)
1	574.59	540
2	841.89	822
3	1871.3	1733
4	2348.1	2046

Retainer

Figure 2- 20 shows the transfer function for the retainer for the accelerometer position shown in Figure 2- 21. Only comparison between the first five natural frequencies of FEM and experimental modal analysis for the retainer has been listed in the Table 2- 5 . It can be seen that the first frequency of the retainer starts from 6411 Hz which is far greater than the frequency range of interest. Human hand arm perception of vibration levels at such high frequencies is negligible. Therefore it is safe to assume that the dynamics of the retainer contributes very little in the 0-1000 Hz frequency range as far as HAVS is concerned.

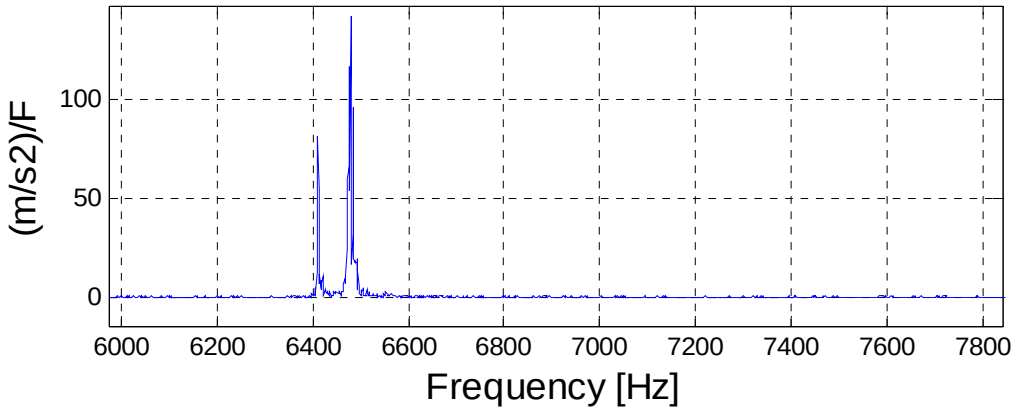

Figure 2- 20 : Transfer function of the retainer from the impact location to accelerometer on retainer

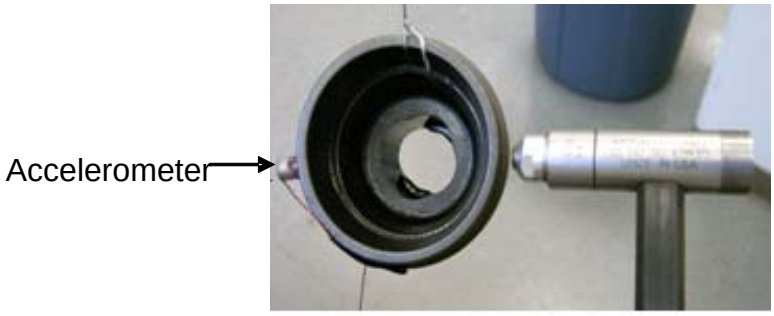

Figure 2- 21: Modal test of retainer

Table 2- 5: Comparison of FEM and experimental modal analysis results for retainer

Mode	FEM (Hz)	Experiment (Hz)
1	6072.8	6411
2	6151.8	6481

Chisel

Figure 2- 22 shows the transfer function for the retainer for the accelerometer position shown in Figure 2- 23. Again only comparison between the first five natural frequencies of FEM and experimental modal analysis for the chisel have been listed in the because as mentioned earlier the first frequency of the chisel starts from 3284 Hz which is far greater than the frequency range of interest i.e. 0-1000 Hz. These natural frequencies were too high to consider in the context of HAVS as was the case with retainer.

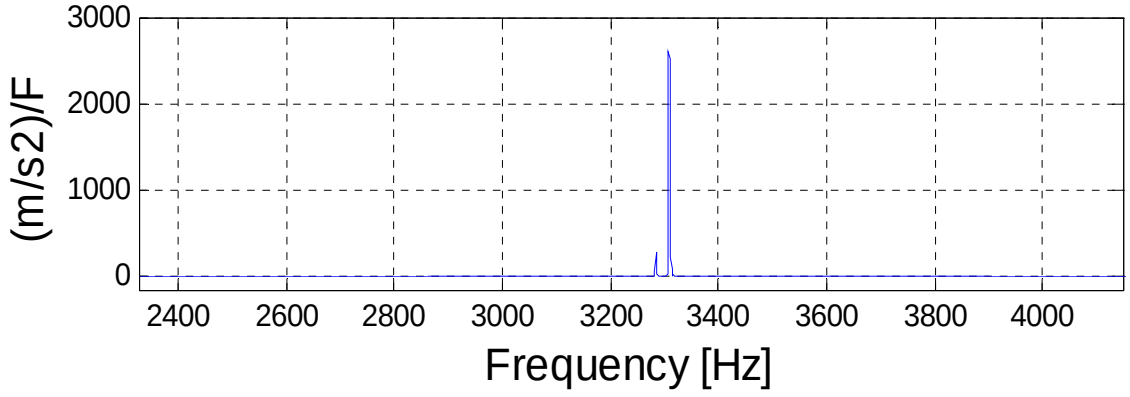

Figure 2- 22 : Transfer function of chisel from the impact location to accelerometer on chisel

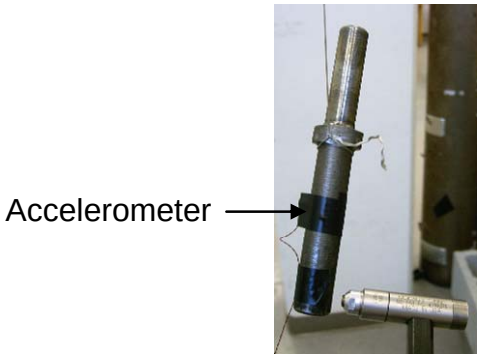

Figure 2- 23 : Modal test of the chisel

Table 2- 6 : Comparison of FEM and experimental modal analysis for chisel

Mode No.	Experimental (Hz)	FEM (Hz)
1	3284	1568.3
2	3309	1669.9

In summary, it can be said that the bending mode of the handle at 540 Hz and the twisting mode at 820 Hz are an important factors as far as hand transmitted vibration is considered.

Chapter 3. Development and Validation of the Experimental Hand-Arm Rig

The experimental rig was built in order to have a robust and repeatable test apparatus in order to evaluate the performance of the control techniques and also to avoid the uncertainties involved in the human tests as explained in section 1.2.1 previously. In this chapter the development and validation of the experimental hand-arm rig is discussed. Also the chapter explains the approach used to design the rig and the experiments carried out to validate the rig. Finally detailed results from the experiments are presented.

3.1. Experimental Hand-Arm Rig

This section deals with the design, development and building of the experimental hand-arm rig. Also it illustrates the need for the building an experimental rig.

3.1.1. Preliminary Approach towards Design of the Horizontal Beam

Initially it was thought that a mechanical model of hand-arm system would be feasible and could be built using an Aluminum beam. The model consisted of one horizontal beam and two vertical beams that support the impact hammer. The horizontal beam was a simply-supported beam configuration as shown in the Figure 3 - 1 . A finite element model of a simply supported Aluminum beam was developed to explore the idea further as shown in Figure 3- 2. The aim was that the response of the horizontal beam should simulate the dynamic behavior of the hand-arm. The design of the beam was based on the numerical model of four-degree-of-freedom developed by Reynolds et al.[2]. Figure 3 - 3 shows a comparison between the response of the beam and the response of the proposed 4-DOF

model. The response of the both models varied very significantly from each other. The 4-DOF model was made up of very small masses with very high damping and negligible stiffness. Hence the 4-DOF model behaved almost like a damper. Whereas the horizontal beam was made up of Aluminum so it has large stiffness and very negligible damping. The first resonant frequency of the aluminum beam of length 39 inch and cross section of 9 square inch occurs at approximately 73 Hz as can be seen from Figure 3 - 3. After performing simulations on the finite element model of the beam, it was realized that building the 4-DOF model with the Aluminum beam would not be practical. This is because the rig would require sufficient stiffness in order to hold the tool while in operation. In addition the rig would also need large damping and significant mass. Hence a more experimental approach was chosen instead of the numerical approach to build the experimental rig. Since it was realized that an aluminum beam can't be used to simulate hand-arm dynamics, a hollow fiber glass beam was chosen. The idea behind the hollow section was that it would be easy to add damping to the beam by adding viscous damping material in the cavity.

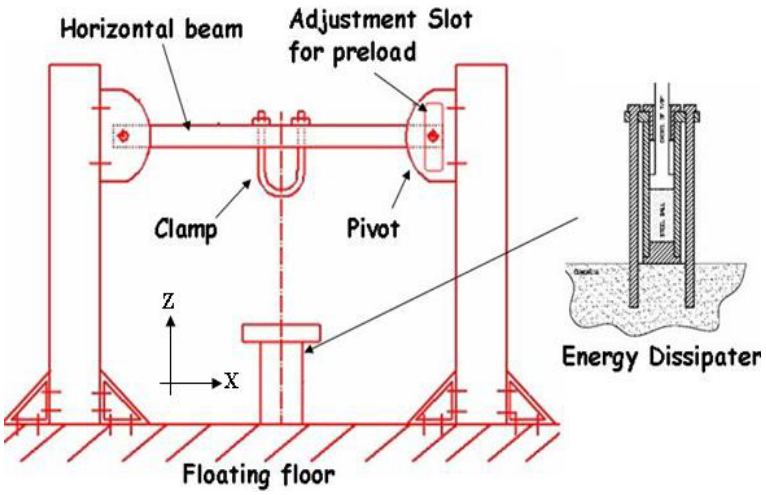

Figure 3 - 1: Schematic of the experimental hand-arm rig and energy dissipater

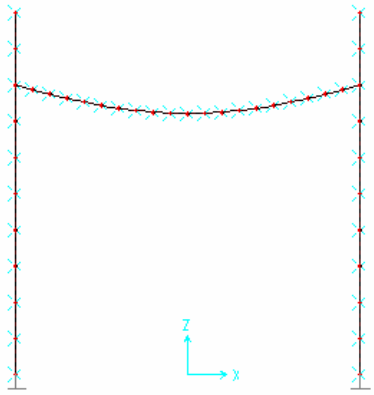

Figure 3- 2: Finite element model of the test rig

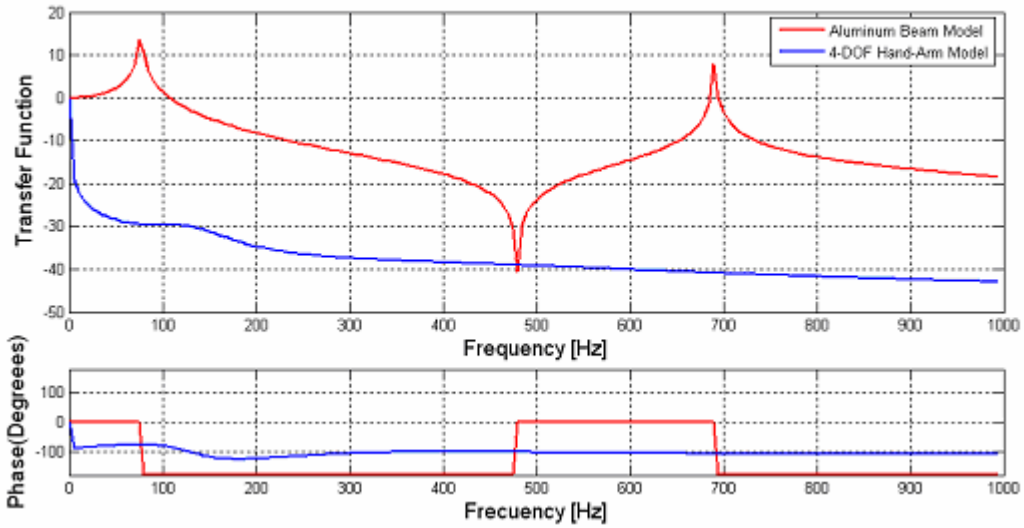

Figure 3 - 3: Transfer function and phase of the four-degree-of-freedom model and the finite element model.

3.1.2. Development of the Experimental Rig

The experimentally simulated hand-arm rig along with the tool mount and accelerometer mounting position are shown in the Figure 3 - 4-a, b and c respectively. The experimental rig was designed to simulate the hand arm dynamics as discussed previously. The experimental simulated hand-arm rig consisted of a hollow and rectangular cross-sectional fiber glass beam. The hollow portion of the beam was filled with lead balls to add mass to the system without adding stiffness. Viscous glue was added to the balls to keep them well coupled with the fiber glass beam. In addition the balls added damping to model since the

hand-arm system is heavily damped. The beam was mounted using pivot joints between two vertical extruded aluminum beams (effectively a simply-supported configuration). A simple U-shaped clamp was used to mount the tool to the experimental rig as can be seen from Figure 3 - 4 (b). A rubber grip was placed between the tool and the U-shaped clamp to simulate the interface between the tool and the palm. An adjustment slot in the pivots allows a variable preload to be applied. An accelerometer was mounted on the tool in order to measure the vibration in the direction of the axis of drilling operation another accelerometer was mounted on the horizontal beam to measure the beam response. An energy dissipater, into which the tool is driven, was manufactured as described in the ISO 8662-2 standard [8]. The dissipater was filled with rubber and steel balls. Both the dissipater and the vertical beam were mounted firmly on the floating floor in the lab.

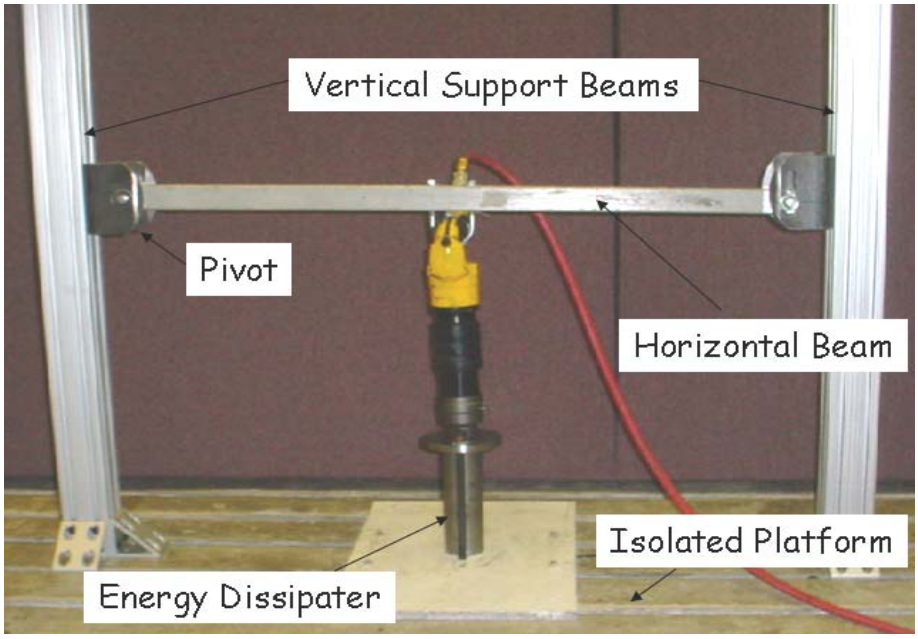

(a)

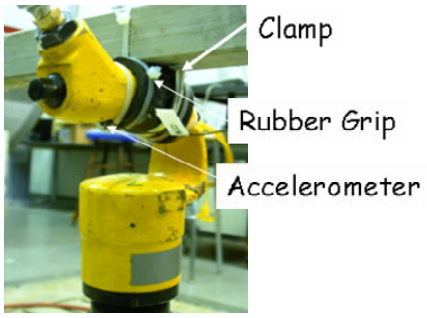

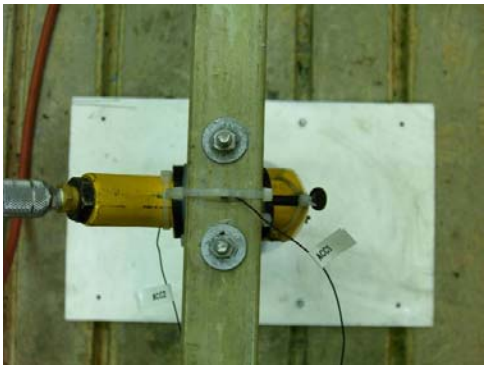

(b) **(c)**

Figure 3 - 4: Experimental rig (a) front view, (b) tool mount and (c) top view

3.2. Experimental Tests to Validate the Experimental Rig

Various experiments have been carried out using the experimental rig in order to validate the experimental approach such as a loaded vibration tests for the rig and human subjects etc. In addition various experimental test set-ups has been developed and built to carry out these tests. In this section, the description for each of the set-ups will be presented in detail.

3.2.1. Vibration Tests with the Free-Free Boundary Conditions

It is important to know the absolute vibration levels generated by the impact hammer while in operation as it helps to understand the effect of the loading conditions and hand arm system on the dynamics of the impact hammer. With the tool suspended from the top by means of a rope the compressed air of 90 psi was allowed to drive the impact hammer in a free-free (unloaded) condition. The accelerometer was mounted at the handle of the tool in the Z-direction. It was observed that the sometimes the tool does not work properly without any loads. So care was taken to ensure that the tool was running properly before and after the tests.

The free-free test shows true acceleration levels coming out from the impact hammer due to the repeated impacts while it is operating. Figure 3 - 5 shows the auto-spectrum for the hammer at the free-free (unloaded) condition. Three tests were carried out with three different chisels in order to understand the effect of the chisels on the response of the tool. Two of the chisels were provided by the tool manufacturer with the tool whereas the third chisel was manufactured as per ISO 8662-2 as explained in Appendix 4. The response of the tool for the ISO 8662-2 chisel was the same as that for the other two chisels. As a result the ISO-8662-2 chisel could be used for the further tests.

Figure 3 - 5 shows extremely high acceleration levels in the low frequency range from 0-100 Hz. Also the handle resonance occurs at 520 Hz and this underlying resonance can also be seen in Figure 3 - 5. The narrowband auto-spectrum was converted to 1/3-octave band auto-spectrum as shown in Figure 3 - 6.

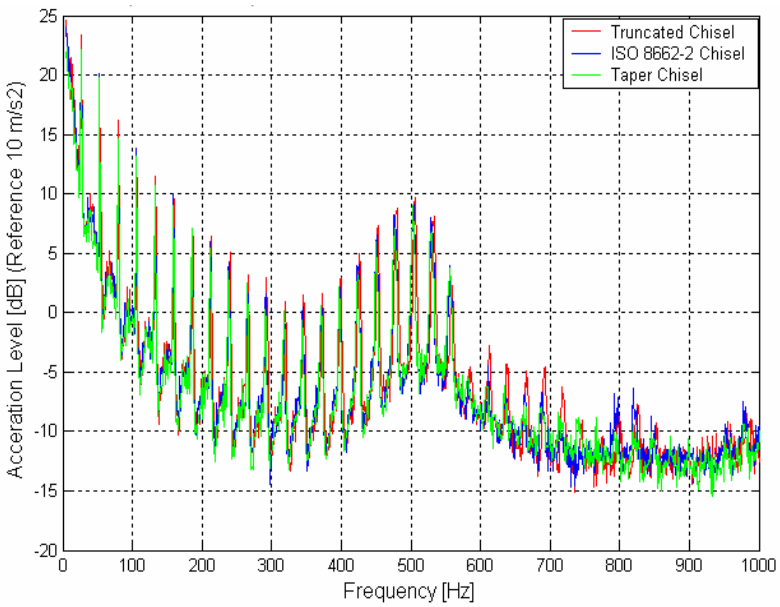

Figure 3 - 5 : Narrowband acceleration auto-spectrum (dB) of the tool handle for free-free boundary conditions

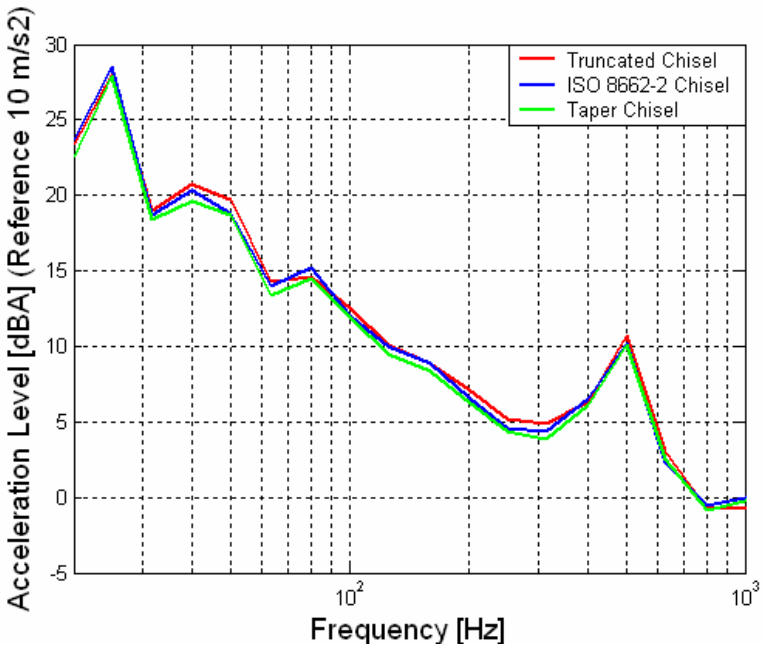

Figure 3 - 6: 1/3 Octave band acceleration auto-spectrum (dBA) for three different chisels for free-free boundary conditions

3.2.2. Vibration Tests with the Human Subjects

The vibration test of the impact hammer was taken with three different human subjects. All the human subjects chosen for the tests were VAL graduate students. One subject carrying

out the vibration test is shown in the Figure 3 - 7. These tests were carried out in order to understand the basic nature of the vibration levels when a human is operating the hammer and later to validate the experimental rig performance. The subjects were asked to hold the hammer while applying specified preloads. The digital weighing scale was used for maintaining a constant preload on the hammer throughout the test as can be seen from Figure 3 - 7. Tests were run for almost one minute continuously. These tests were repeated three times to check the repeatability of the human subjects. Each of the test sets was carried out on three consecutive days.

Figure 3 - 7 : Human vibration tests

3.2.3. Vibration Tests with the Experimental Rig

Figure 3 - 8 shows the typical auto-spectrum of the acceleration of the tool-handle when mounted on the experimentally simulated hand-arm and during the three human tests for the 200N preload case. The auto-spectrum of the tool is dominated by densely packed peaks consisting of the harmonics of the blow frequency of the tool with a background broadband

acceleration. The response of the rig matches very well with that of the human subjects for the case shown. Figure 3 - 9 illustrates the operating frequency of the impact hammer which is approximately 27 Hz. In addition the 520 Hz harmonic can still be seen in the data (Figure 3 - 8).

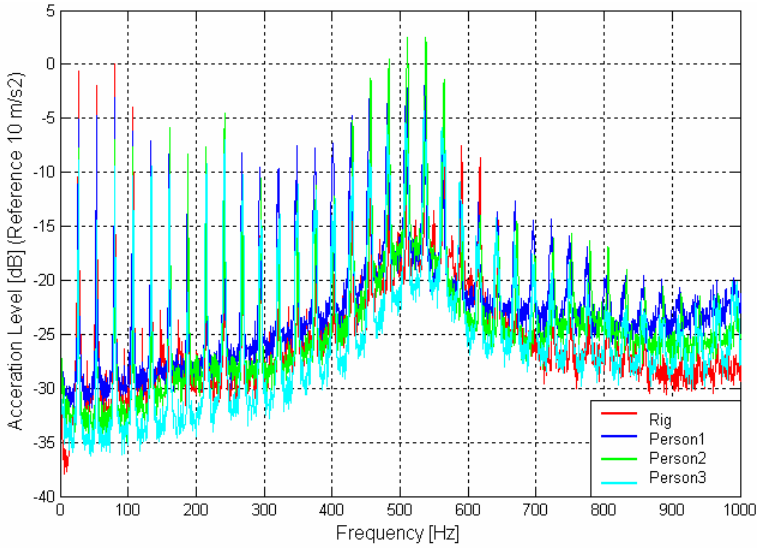

Figure 3 - 8 : Narrowband acceleration auto-spectrum (dB) of the tool-handle for rig and human subjects

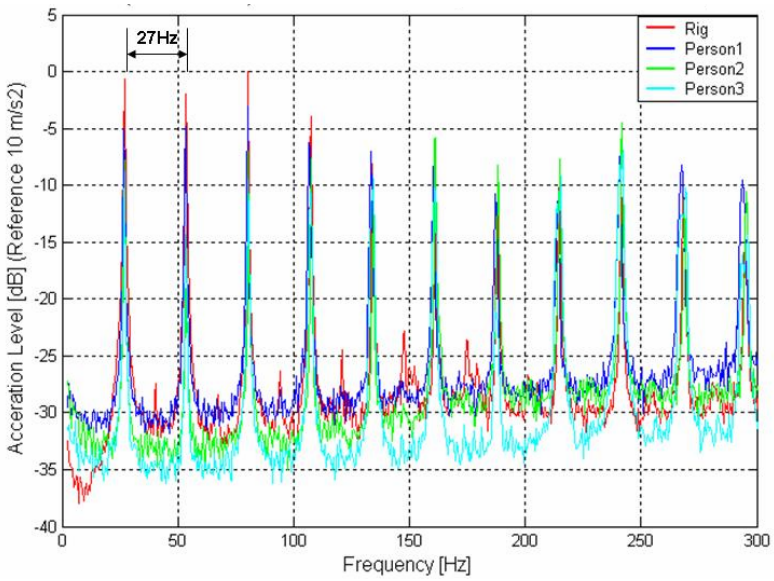

Figure 3 - 9 : Operating frequency of the impact hammer

3.3. Results

This section presents with the results obtained from the tests mentioned above. In order to obtain an easier comparison between cases the RMS accelerations levels were plotted in 1/3 octave bands and is presented in this section in detail.

3.3.1. Comparison between the Free-Free and Loaded Test

Figure 3 - 10 demonstrates the comparison between the free-free and loaded test for the human subjects. There is a drastic drop in the vibration levels in the lower frequency range 0-300 Hz. This may be due to a combination of two factors. Application of the feed force by the subjects in the Z-direction introduces mechanical impedance which tends to suppress the vibration levels due to the primary impact frequency of the tool. Secondly, there is large energy absorption in the low frequency range area. The vibration levels drop approximately 20db. Interestingly there has been comparatively less energy absorption in the high frequency range 300-1000 Hz. The vibration levels drop about 5 db. This is also in line with the previously published research in this area according to which the maximum damage to hands happens in the low frequency.

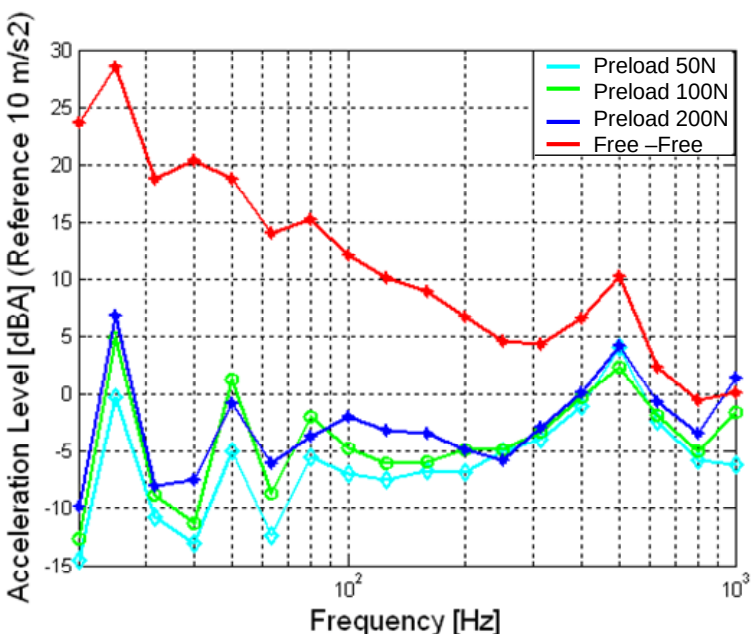

Figure 3 - 10: Comparison of 1/3 Octave band acceleration auto-spectrum (dBA) of tool handle for free-free boundary conditions versus human tests

3.3.2. Validation of the Experimental Rig

The narrowband auto-spectrum of the tool was converted into 1/3-octave band auto-spectrum as shown in the Figure 3 - 11 .The data shows that there is some variation between the responses of tool for different people for the same preload and the tool response for the experimental rig lies very close to the range of tool response for the human subjects. There is a high frequency peak in the 500 Hz band and this corresponds to the resonance of the tool handle, measured at 520Hz in an earlier impulse hammer modal test. The result shows three distinctive peaks appear in the 0- 200Hz frequency range. The first peak at 25 Hz corresponds to the impact frequency (~27 Hz) of the tool and the first and second harmonic of the blow frequency appears subsequently. The comparison is 2-3 higher at low frequencies and around 5 db lower at high frequency

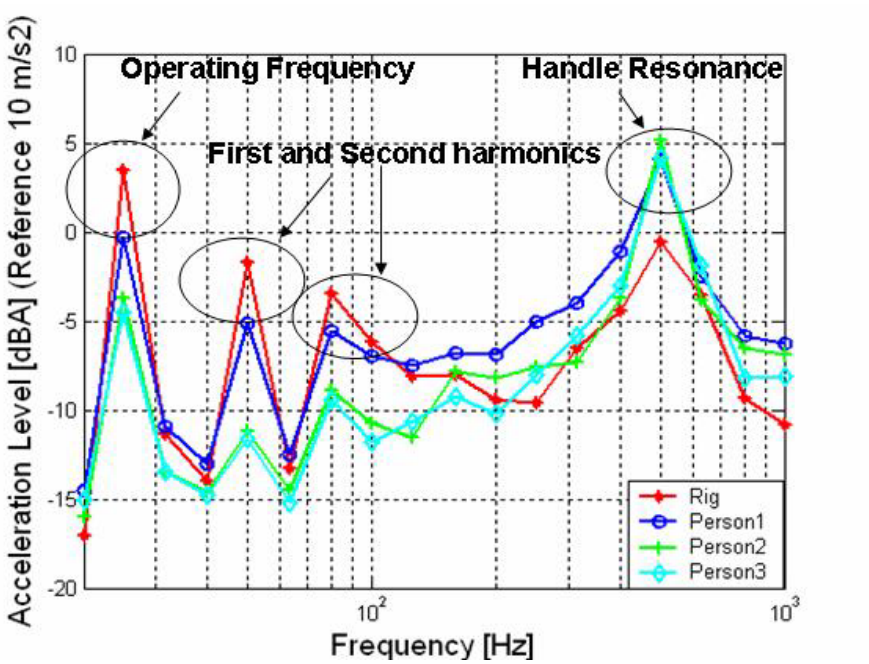

Figure 3 - 11: Comparison of 1/3 octave band acceleration auto-spectrum (dBA) of the tool-handle for human subject versus rig at 200N

3.3.3. Repeatability of the Experimentally Simulated Hand-Arm Rig and Human Test

Repeatability is a measure of reliability of the results and is very important aspect in the experimental tests. In order to investigate repeatability, two different tests were conducted for both the experimentally simulated hand-arm rig and three human subjects for each preload on different days. The comparative results are presented in this section. As an example, Figure 3 - 12 (a) shows the measured accelerations of the tool for the simulated rig for the two different tests at 50N preload. The tool response for the simulated rig is comparatively consistent particularly in the low frequency region from the 0 to 300 Hz. After 300 Hz, the response of the simulated rig becomes slightly uncertain. The maximum variation in the vibration level is 3 dbA. This could be due to the nonlinear nature of damping added to the horizontal beam and changes in the tool mounting. Figure 3 - 12 (b), (c) and (d) also shows the test results for the three 50N preload cases for three human

subjects. While the repeatability for Person 1, Person 2 appears to be very good for different tests, the repeatability for the Person 3 for the different tests seems poor. The maximum variation in vibration levels is 5 dbA. There are many factors which could contribute to this variation such as changes in the grip/push force and hand-arm position etc. Overall, it appears that there is some degree of variation in the tool response for human tests results as well as the tool response for the simulated rig results. The results for the different preload cases are presented in the Appendix D. To counter the variation in the case of the rig and human subjects, it was decided take an average of a number of tests. So, in the next sections the averages of the two different tests were plotted for the comparison. The comprehensive analyses of the results are also presented.

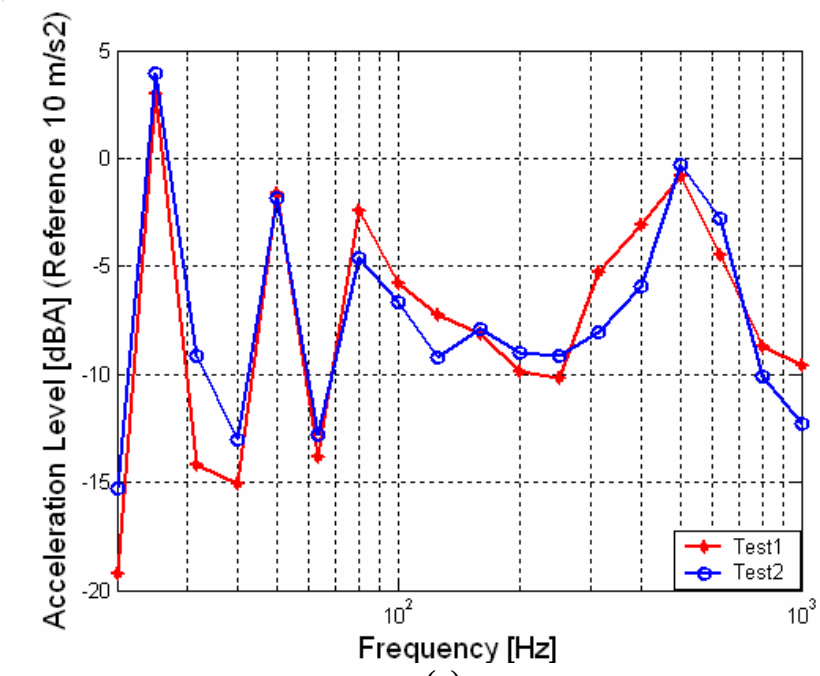

(a)

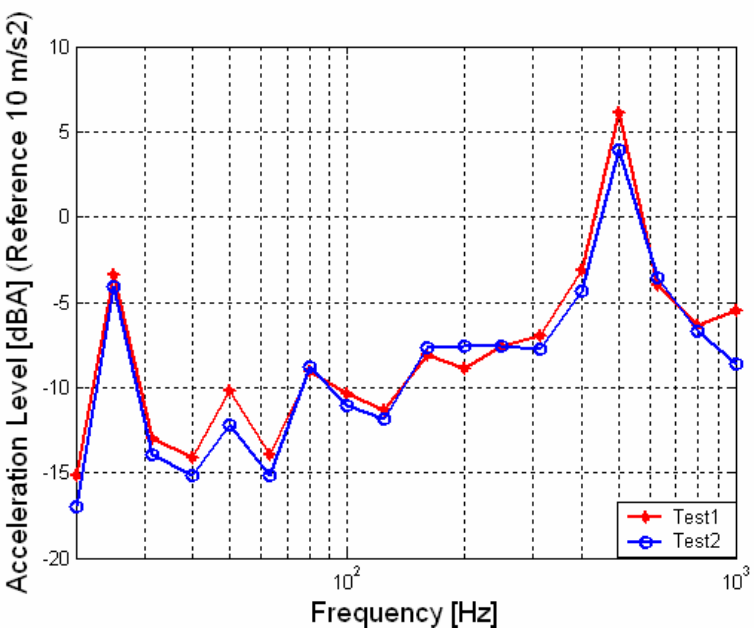
Acceleration Level [dBA] (Reference 10 m/s2)
10
5
0
-5
-10
-15
-20
10^2
10^3
Frequency [Hz]
Test1
Test2

(b)

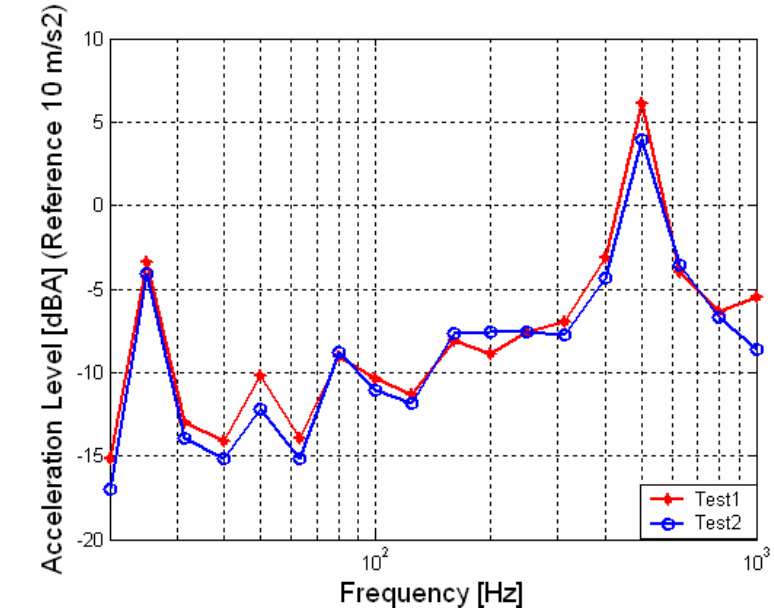
Acceleration Level [dBA] (Reference 10 m/s2)
10
5
0
-5
-10
-15
-20
10^2
10^3
Frequency [Hz]
Test1
Test2

(c)

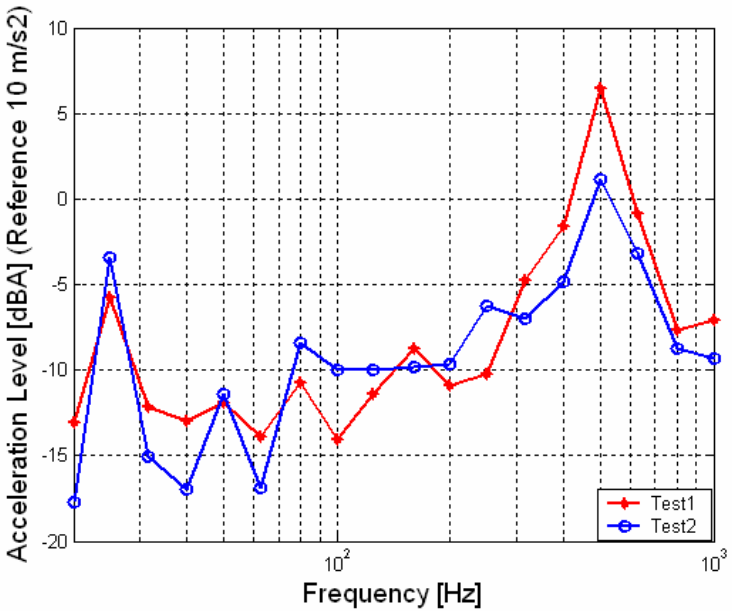

(d)

Figure 3 - 12 : Repeatability of acceleration auto-spectrum (dBA) results for two different tests (a) experimental rig tests, (b) person 1 tests, (c) person 2 tests and (d) person 3 tests (for two different days) at preload 50N

3.3.4. Variation in the Auto-Spectrum of the Tool for Different Loads

Tests were conducted for three different preloads both for the experimentally simulated hand-arm rig and the test subjects. Two sets of such tests were carried out. The results obtained are the average of two such sets as shown in Figure 3 - 13. It has been reported in the literature that an increase in preload leads to an increase in the drive point mechanical impedance[14] i.e. the amplitude of the peak accelerations decrease. The results of the human tests Figure 3 - 13 b, c, d were in agreement with those published previously. The simulated rig test results show that with increase in the preload the peak accelerations of the tool decrease but very marginally (approximately 1 dbA) compared to the human tests results (approximately 3 dbA).

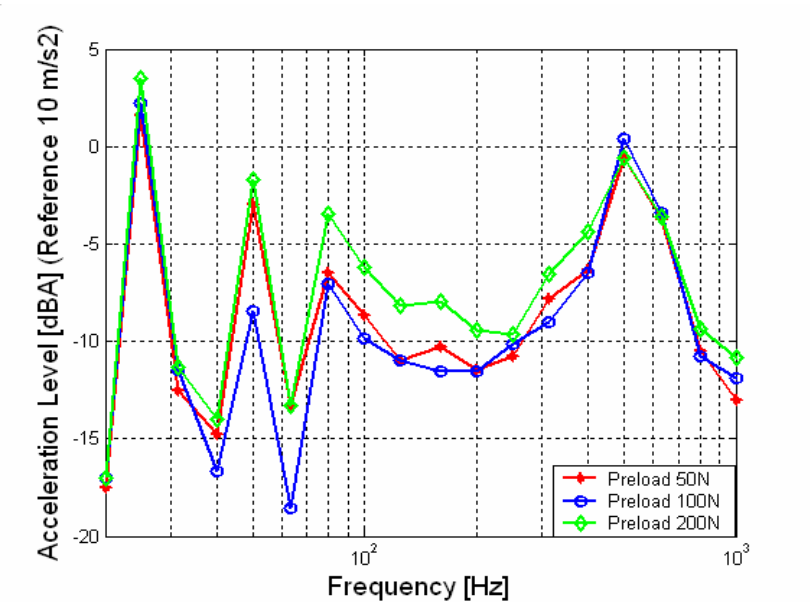
Acceleration Level [dBA] (Reference 10 m/s2)
5
0
-5
-10
-15
-20
10^2
10^3
Frequency [Hz]
Preload 50N
Preload 100N
Preload 200N

(a)

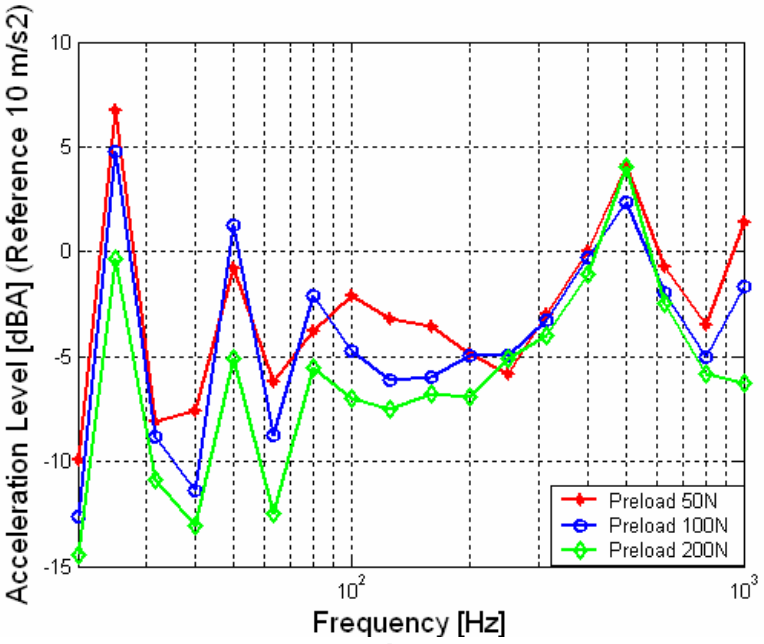
Acceleration Level [dBA] (Reference 10 m/s2)
10
5
0
-5
-10
-15
10^2
10^3
Frequency [Hz]
Preload 50N
Preload 100N
Preload 200N

(b)

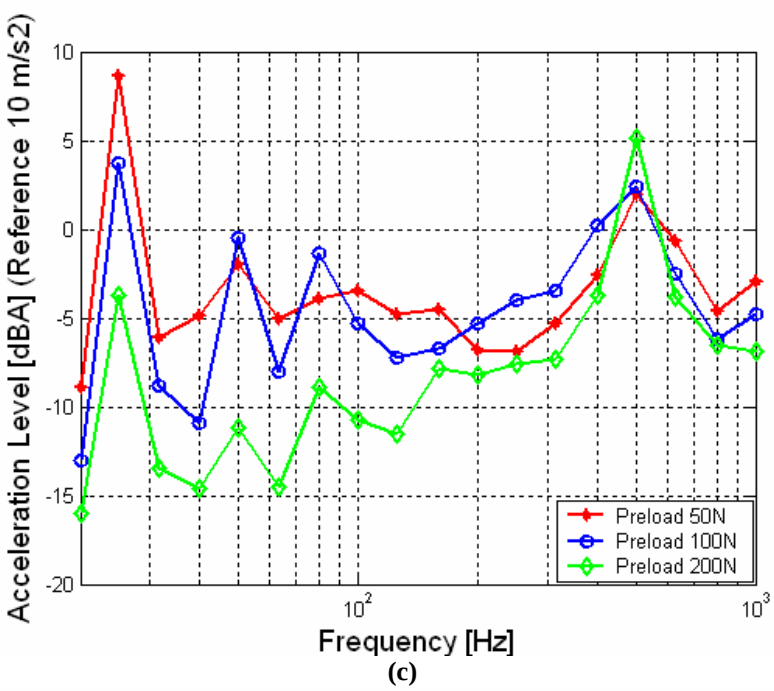

(c)

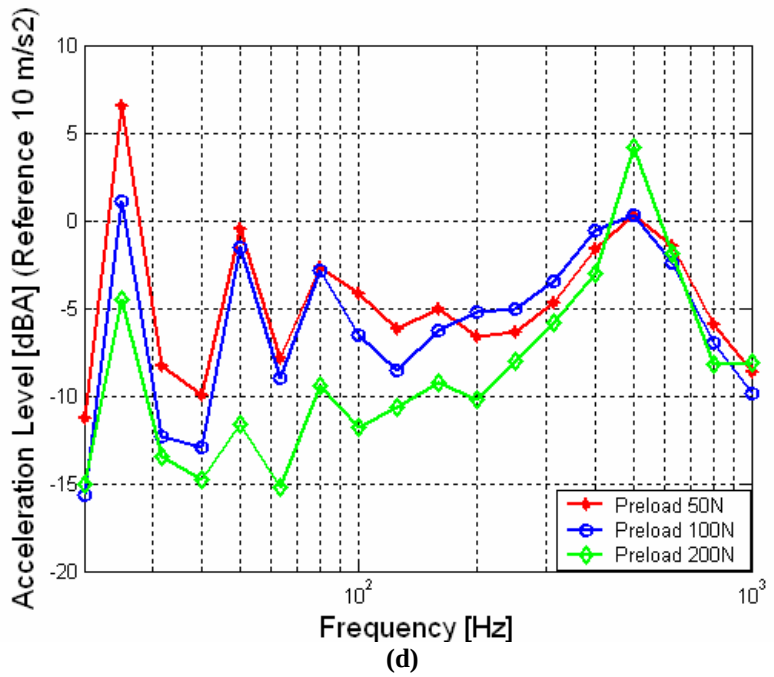

(d)

Figure 3 - 13: Variation of the acceleration auto-Spectrum (dBA) of tool handle (dBA) (two-test average) with different preloads for (a) experimental Rig , (b) person 1, (c) person 2 and (d) person 3

3.3.5. Average Acceleration Levels for Two Repeat Tests at Different Preload Cases

Figure 3 - 14 shows that the tool response for the rig and the human subjects for all the three different preload cases. For the all the cases the tool response for the rig and for the human subjects follows exactly the same trend with the peaks appearing at the same 1/3-octave frequency bands. In terms of the amplitude of the 1/3-octave band accelerations, the levels of the tool response for the rig at preload 200N are in the range of the tool response for human tests. However for the preload cases 50N and 100N, the levels of the tool accelerations for the rig are slightly lower compared to that for the human tests. The maximum acceleration level for the human subjects is 1.8 dBA (Person 1) and for the rig it is 1.4 dBA at preload 200N. The maximum acceleration level for the human subjects is 2.3 dBA (Person 1) and for the rig it is 1.4 dBA at preload 100N. The maximum acceleration level for the human subjects is 3.5 dBA (Person 1) and for the rig it is 1.3 dBA at preload 50N. Overall, the tool response for the rig simulates the tool resonance for the human subjects better at higher load i.e.100N and 200N. This could be due to smaller degree of uncertainty in applying loads in case of the rig.

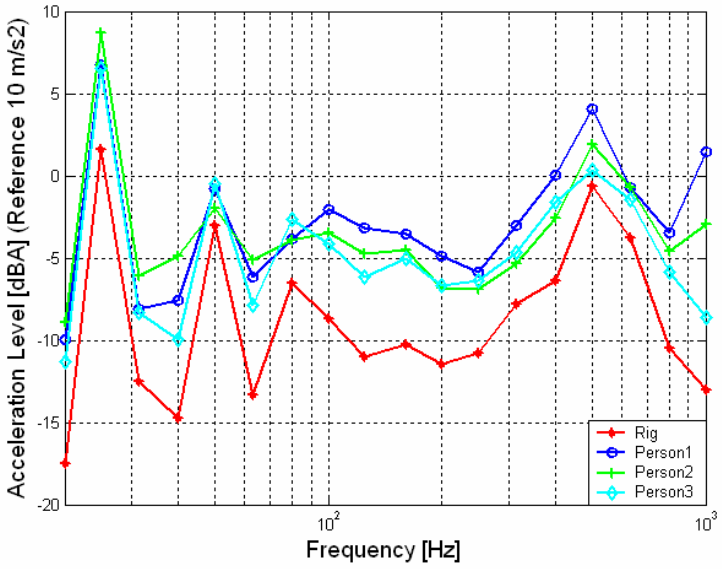
Acceleration Level [dBA] (Reference 10 m/s2)
Frequency [Hz]
Rig
Person1
Person2
Person3

(a)

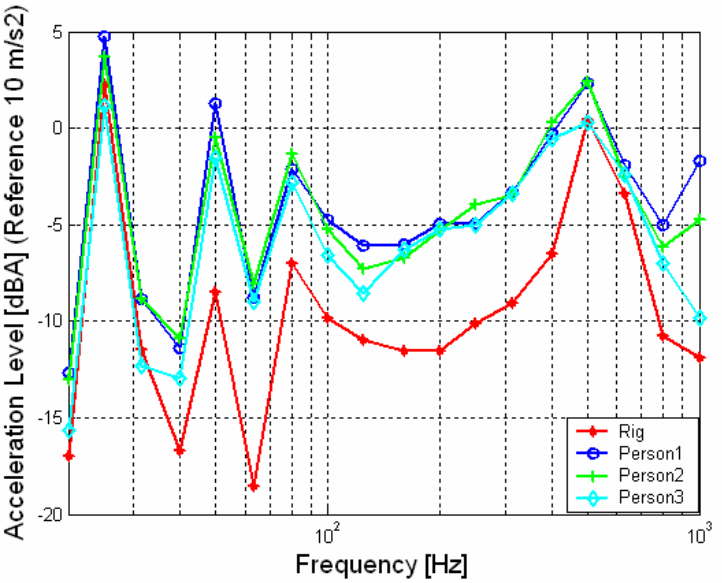
Acceleration Level [dBA] (Reference 10 m/s2)
Frequency [Hz]
Rig
Person1
Person2
Person3

(b)

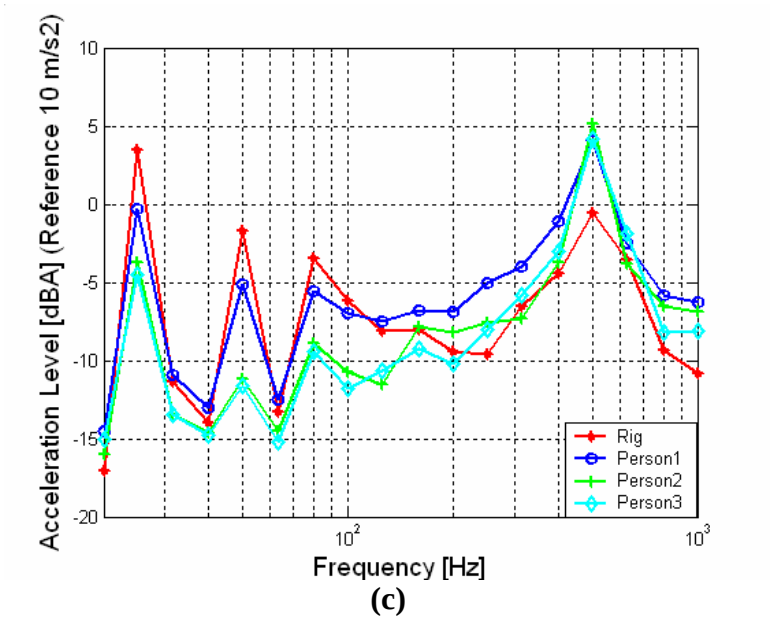

Figure 3 - 14: Comparison of acceleration (two tests averages) auto-spectrum of tool handle (dBA) for rig and human subjects for (a) preload 50N, (b) preload 100N and (c) preload 200N

3.3.6. Variance in the Acceleration for the Rig and the Human Subjects' Tests

Figure 3 - 15 , Figure 3 - 16 and Figure 3 - 17 show that the variance of acceleration for the rig and human subjects. For preload 50N case the variance of acceleration of the rig is less than that of the human subjects for in the low frequency range 0-100 Hz except for 50 Hz. Afterwards it exceeds than that of the Person1 and Person2 but remains less than that of the Person3. For the Preload 100N, the variance of acceleration for the rig was lesser than that of the Human Subjects in general barring 50 Hz and 315 Hz. For the Preload 200N, the variance of acceleration is more or less same as that of human subjects for frequency range 0-250 Hz expect for 80 Hz. At higher frequencies it exceeds than that of Person1 and Person2 but lesser than Person3. Looking at the following results it can be said that the rig is fairly consistent in lower frequency range. But at higher frequency the response of the tool for the rig is slightly uncertain.

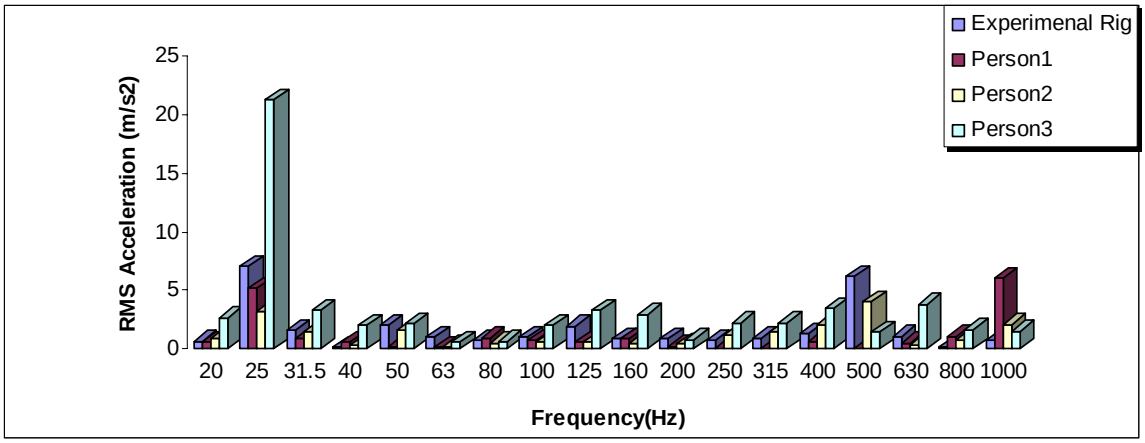

Figure 3 - 15 : Variance in the acceleration (m/s^2) for rig and human subjects tests at preload 50N

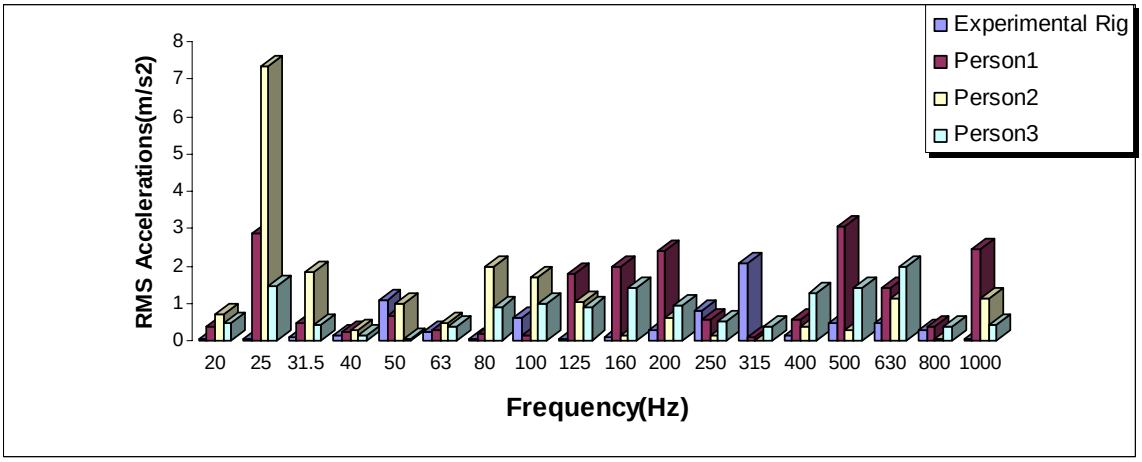

Figure 3 - 16 : Variance in the acceleration (m/s^2) for rig and human subjects tests at preload 100N

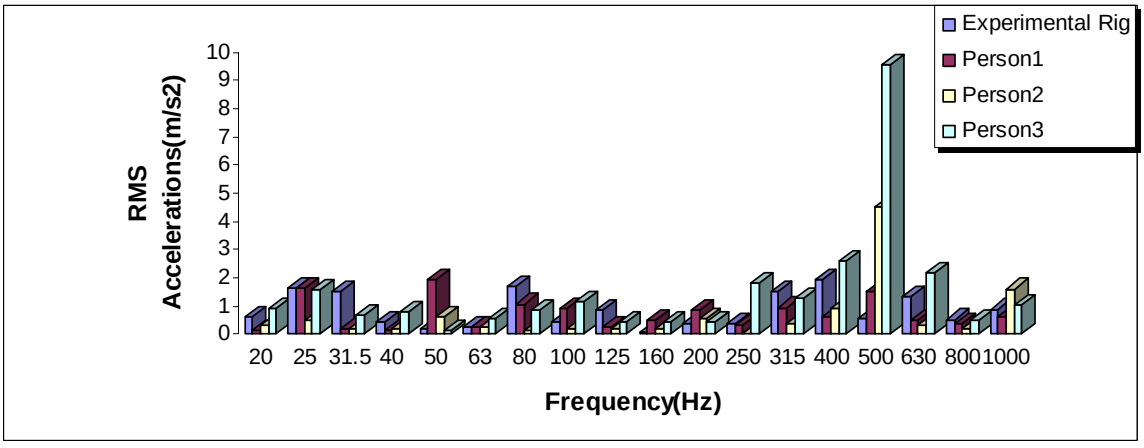

Figure 3 - 17 : Variance in the acceleration (m/s^2) for rig and human subjects tests at preload 200N

Chapter 4. Mathematical Formulation and Numerical Simulation of a Pneumatic Impact Hammer

In this chapter, a novel nonlinear numerical model for the pneumatic impact hammer is proposed and the mathematical formulation is presented. In order to validate the model, a series of experiments have been carried out to measure the exhaust jet flow rate, the chamber pressures and handle vibration. These experimental results were then compared with the numerical results in order to validate the numerical model.

The objectives behind the numerical model of the pneumatic impact hammer were to simulate the physical aspects that drive the hammer, to devise best possible vibration control techniques as well as to avoid the need for extensive laboratory experiments testing. It can also predict the displacement, velocity and acceleration of each component of the tool as well as the exhaust jet velocity profiles and their levels.

The pneumatic impact hammer has many structural components such as center body, piston etc. but the forcing input given to the hammer is pneumatic as can be seen in Figure 4- 1. The piston inside the hammer is driven by the differential pressures across the piston. Therefore these impact hammers can be fundamentally divided into two sub-models 1) a structural dynamic model and 2) a fluid flow model. Therefore, it is important to mathematically formulate both parts and then couple the models together.

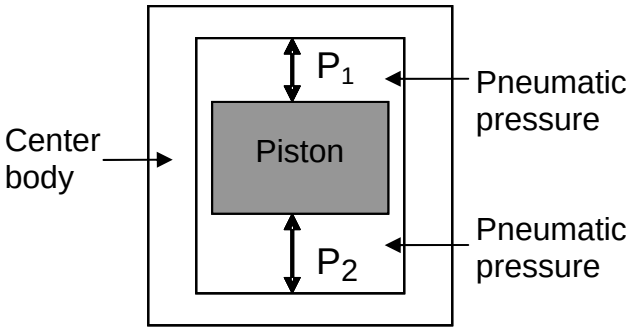

Figure 4- 1: Conceptual model of pneumatic hammer showing the structural and fluid coupling

4.1. Mathematical Formulation of the Pneumatic Impact Hammer Model

Vibrations in the impact hammer are mainly generated by the impacts between the chisel and the piston and reaction forces as the piston is accelerated. These repetitive impacts then propagate through the interconnected structural components exciting system resonances. Therefore, in order to calculate the vibration levels, the components of the impact hammer must be considered in the structural dynamic model. The piston inside the impact hammer is forced by pressurized air as explained in the section 2.2 and in order to model this forcing a fluid flow model is developed. The fluid flow model is based on the assumption of isentropic fluid flow through a bleed orifice [34].

4.1.1. Structural Dynamic Model

The structural dynamic model calculates the structural response of all the lumped masses in the impact hammer and therefore the structural model consists of a lumped mass parameter model and impact model. The modeling of impact is nonlinear in nature and therefore requires a time domain numerical integration approach. The lumped parameter and the impact models are explained in detail in the following subsections.

Lumped Mass Approximation of the Pneumatic Impact Hammer

The impact hammer model used here consists of the center body, the chisel, the piston and the handle as shown in Figure 4- 2. The Cartesian co-ordinate system is also shown in the Figure 4- 2 and the position of impact between the chisel and piston is considered to be x=0 and the maximum stroke of the piston is x=102mm. Importantly, the model takes into account the interaction between the chisel and the ground as well as interaction between the handle and the operator's hand. All these components are modeled as lumped masses connected to each other through springs and dampers [33]. Physically the piston is not connected to any of the other component during its entire cycle except when it impacts the chisel for a fraction of a second. Therefore, the impact between the piston and chisel is modeled as a nonlinear spring. Likewise, there is also a nonlinear spring at the top of the chamber which restricts the piston going beyond the maximum specified stroke. The contact between the chisel and center body is also modeled in this way. A small amount of the kinetic energy of the piston is dissipated to overcome friction between the piston and center body and this friction is included in the model as another damping term. The modeling of the friction is important because it determines the velocity of the piston and the stroke of the piston. The ground is considered to be a large energy dissipater i.e. large damping terms. The human hand is also modeled as a very heavily damped system. The stiffness and damping terms in the model are dependent on the individual stiffness and damping terms of the two connecting components as explained in Figure 4- 2. It should be noted that the structural model predicts the vibration response only in the X-direction.

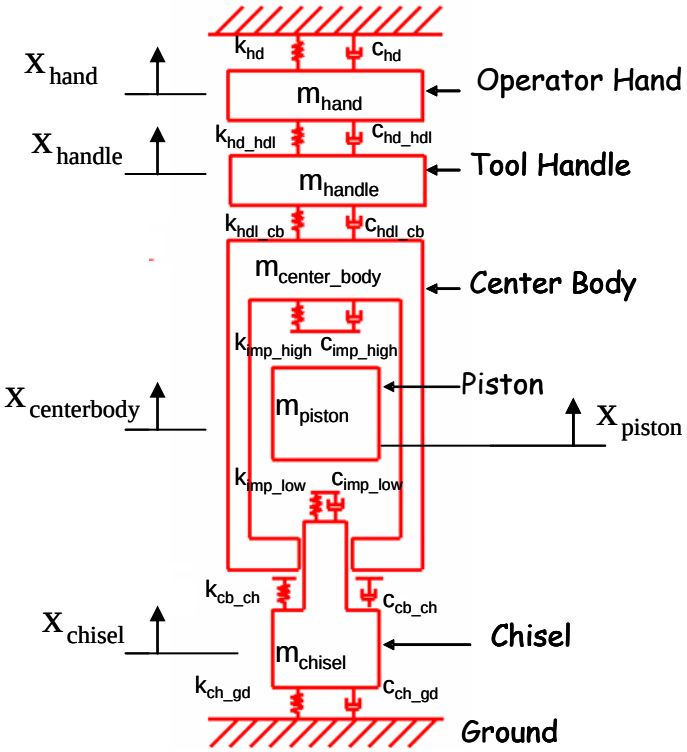

Figure 4- 2 : Structural dynamic model of the impact hammer

The forced response of the structural system is given by the following second order system of the ordinary differential equations.

$$\mathbf{M}\ddot{\mathbf{x}}(t) + \mathbf{C}(t)\dot{\mathbf{x}}(t) + \mathbf{K}(t)\mathbf{x}(t) = \mathbf{F}(t) \qquad \textbf{(4. 1)}$$

Here **M**, **K(t)** and **C(t)** are the mass, stiffness and damping matrices whereas **x** and **F(t)** are the displacement and force vectors. The stiffness matrix **K(t)**, and damping matrix **C(t)** are time dependent due to the nature of hammer operation (repetitive impacts) and the numerical modeling of these time dependent terms in the matrices **K(t)** and **C(t)** will be explained in this section afterwards . A free body diagram of each component of the impact hammer was considered to form the mass, stiffness and damping terms matrices given by,

$$\mathbf{M} = \begin{bmatrix} m_{hand} & 0 & 0 & 0 & 0 \\ 0 & m_{handle} & 0 & 0 & 0 \\ 0 & 0 & m_{center\_body} & 0 & 0 \\ 0 & 0 & 0 & m_{piston} & 0 \\ 0 & 0 & 0 & 0 & m_{chisel} \end{bmatrix} \quad \textbf{(4. 2)}$$

$$K(t) = \begin{bmatrix} k_{hd} + k_{hd\_hdl} & -k_{hd\_hdl} & 0 & 0 & 0 \\ -k_{hd\_hdl} & k_{hd\_hdl} + k_{hdl\_cb} & -k_{hdl\_cb} & 0 & 0 \\ 0 & -k_{hdl\_cb} & k_{hdl\_cb} + k_{cb\_ch}(t) + k_{imp\_high}(t) & -k_{imp\_high}(t) & -k_{cb\_ch}(t) \\ 0 & 0 & -k_{imp\_high}(t) & k_{imp\_high}(t) + k_{imp\_low}(t) & -k_{imp\_low}(t) \\ 0 & 0 & -k_{cb\_ch}(t) & -k_{imp\_low}(t) & k_{imp\_low}(t) + k_{cb\_ch}(t) + k_{ch\_gd} \end{bmatrix}$$

(4. 3)

$$C(t) = \begin{bmatrix} c_{hd} + c_{hd\_hdl} & -c_{hd\_hdl} & 0 & 0 & 0 \\ -c_{hd\_hdl} & c_{hd\_hdl} + c_{hdl\_cb} & -c_{hdl\_cb} & 0 & 0 \\ 0 & -c_{hdl\_cb} & c_{hdl\_cb} + c_{cb\_ch}(t) + c_{imp\_high}(t) & -c_{friction} - c_{imp\_high}(t) & -c_{cb\_ch}(t) \\ 0 & 0 & -c_{friction} - c_{imp\_high}(t) & c_{imp\_high}(t) + c_{friction} + c_{imp\_low}(t) & -c_{imp\_low}(t) \\ 0 & 0 & -c_{cb\_ch}(t) & -c_{imp\_low}(t) & c_{imp\_low}(t) + c_{cb\_ch}(t) + c_{ch\_gd} \end{bmatrix}$$

(4. 4)

The displacement vector **x** can be expressed as follows,

$$\mathbf{x} = \begin{Bmatrix} x_{hand} \\ x_{handle} \\ x_{centerbody} \\ x_{piston} \\ x_{chisel} \end{Bmatrix} \quad \textbf{(4. 5)}$$

The right hand side of equation 4.1 i.e. the forcing vector is obtained from the fluid flow model as explained in section 4.2.2. It is assumed that $F_{preload}$ is the force applied by the operator on the impact hammer. It is known that the force produced by the pressurized air on the piston is equal to the product of the area of the bore of the center body and the pressure differential across the piston. To balance the force on the piston, an equal and

opposite force was applied on the center body. This force is modeled as F_{piston} in the forcing vector and therefore the force vector takes the following form.

$$\mathbf{F(t)} = \begin{Bmatrix} F_{preload} \\ 0 \\ -F_{piston} \\ F_{piston} \\ 0 \end{Bmatrix} \quad \textbf{(4. 6)}$$

The time dependent force F_{piston} is calculated from the fluid flow model and is explained in section 4.1.2. The value of $F_{preload}$ can be changed for a particular preload such as those tested experimentally in Chapter 3.

Structural Response using the State Space Formulation

The force response of the M-DOF system can be solved numerically using a state-space formulation. A state space representation is a mathematical model of a physical system as a set of input, output and state variables related by the first order differential equations where the variables are expressed in matrices and vectors. As discussed previously the stiffness and damping matrices and the forcing input **F(t)** are a function of time.

$$\mathbf{M\ddot{x}(t) + C(t)\dot{x}(t) + K(t)x(t) = F(t)} \quad \textbf{(4. 7)}$$

The initial conditions for the displacement and velocity of all the masses are given by,

$$\mathbf{x(0) = x_0} \ \& \ \mathbf{\dot{x}(0) = \dot{x}_0} \quad \textbf{(4. 8)}$$

Multiplying by M^{-1} gives,

$$\mathbf{\ddot{x}(t) + M^{-1}C(t)\dot{x}(t) + M^{-1}K(t)x(t) = M^{-1}F(t)} \quad \textbf{(4. 9)}$$

These are second order dynamically coupled equations that need to be converted to the first order dynamically coupled sate space form.

In order to achieve this assume that,

$$\begin{aligned} \mathbf{y}_1(\mathbf{t}) &= \mathbf{x}(\mathbf{t}) \\ \mathbf{y}_2(\mathbf{t}) &= \dot{\mathbf{x}}(\mathbf{t}) \\ \dot{\mathbf{y}}_2(\mathbf{t}) &= \ddot{\mathbf{x}}(\mathbf{t}) \end{aligned} \quad \textbf{(4. 10)}$$

Therefore,

$$\dot{\mathbf{y}}_1(\mathbf{t}) = \mathbf{y}_2(\mathbf{t}) \quad \textbf{(4. 11)}$$

$$\dot{\mathbf{y}}_2(\mathbf{t}) = -\mathbf{M}^{-1}\mathbf{K}(\mathbf{t})\mathbf{y}_1(\mathbf{t}) - \mathbf{M}^{-1}\mathbf{C}(\mathbf{t})\mathbf{y}_2(\mathbf{t}) + \mathbf{M}^{-1}\mathbf{F}(\mathbf{t}) \quad \textbf{(4. 12)}$$

Writing these equations in a matrix form,

$$\dot{\mathbf{y}}(\mathbf{t}) = \mathbf{A}\mathbf{y}(\mathbf{t}) + \mathbf{f}(\mathbf{t}) \quad \textbf{(4. 13)}$$

Where A is the state matrix,

$$\mathbf{A} = \begin{bmatrix} \mathbf{0} & \mathbf{I} \\ -\mathbf{M}^{-1}\mathbf{K}(\mathbf{t}) & -\mathbf{M}^{-1}\mathbf{C}(\mathbf{t}) \end{bmatrix} \quad \textbf{(4. 14)}$$

The output vector and input force vector consist of,

$$\dot{\mathbf{y}}(\mathbf{t}) = \begin{bmatrix} \dot{\mathbf{y}}_1(\mathbf{t}) \\ \dot{\mathbf{y}}_2(\mathbf{t}) \end{bmatrix} \quad \textbf{(4. 15)}$$

$$\mathbf{f}(\mathbf{t}) = \begin{bmatrix} \mathbf{0} \\ \mathbf{M}^{-1}\mathbf{F}(\mathbf{t}) \end{bmatrix} \quad \textbf{(4. 16)}$$

If **f(t)** can be calculated then the system's state **y(t)** can be estimated using the previous values of the system's state ($\mathbf{y(t-\Delta t)}, \mathbf{y(t-2\Delta t)}$, $\mathbf{y(t-3\Delta t)}$,…) and the previous values of the input force ($\mathbf{f(t-\Delta t)}, \mathbf{f(t-2\Delta t)}, \mathbf{f(t-3\Delta t)}$,…).

Modeling the Impact

The time dependent terms k_{imp_high}, k_{imp_low} and k_{cb_ch} in the stiffness matrix are used to model the impact as mentioned before. The impact is the most important event in the impact hammer operation and occurs when the piston impacts the chisel on its downward stroke

and the kinetic energy from the piston is transferred to the chisel. There is also a small bumper made of plastic at the top end of the chamber but the handle acceleration measurement results show that there no impact at the top end of the stroke. This could be due to the fact that the pressure builds up exponentially as the piston approaches the bumper. Figure 4- 3 is a zoomed in version of Figure 4-2 showing the three varying impact springs. Equation 4.17, 4.18 and 4.19 illustrate the mathematical modeling of the impact between chisel and piston and the piston and center body. These are nonlinear springs which have very large stiffness values when in contact and zero when not in contact.

The impact between the piston and the chisel is formulated as

$$k_{imp\_low} = \begin{cases} k_{imp\_low} & \text{if } x_{piston} - x_{chisel} \le 0 \\ 0 & \text{if } x_{piston} - x_{chisel} > 0 \end{cases} \quad \textbf{(4. 17)}$$

The impact between piston and center body

$$k_{imp\_high} = \begin{cases} k_{imp\_high} & \text{if } x_{piston} - x_{centerbody} \ge \text{Length of piston stroke} \\ 0 & \text{if } x_{piston} - x_{centerbody} < \text{Length of piston stroke} \end{cases} \quad \textbf{(4. 18)}$$

The impact between the center body and the chisel is modeled similar to the above impact formulation.

$$k_{cb\_ch} = \begin{cases} 0 & \text{if } x_{piston} - x_{centerbody} \le 0 \\ k_{cb\_ch} & \text{if } x_{piston} - x_{centerbody} > 0 \end{cases} \quad \textbf{(4. 19)}$$

The time dependent terms c_{imp_high}, c_{imp_low} and c_{cb_ch} in the damping matrix are modeled in the similar way.

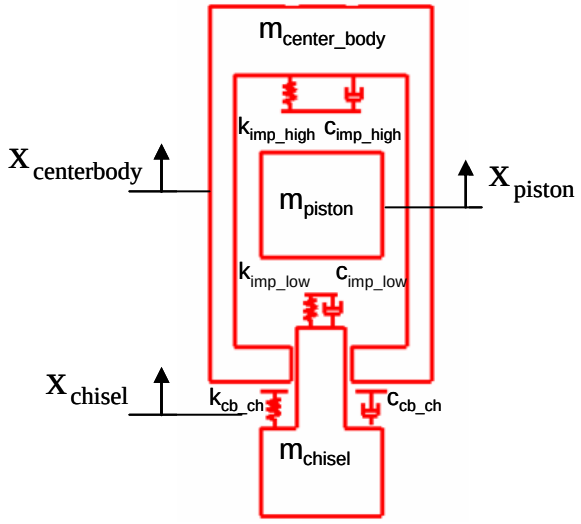

Figure 4- 3: Impact model

4.1.2. Fluid Flow Model

The fluid flow model calculates the effective mass flow rates coming into the upper and lower chambers. Form this, the pressures inside the chambers and the time varying forcing input given to the piston can be calculated. In this section the general theory behind the fluid flow model is given.

Some assumptions were made while modeling the fluid flow behavior and these are as follows,

1) The supply pressure is assumed to be constant at all times.
2) It is assumed that the ideal equation of state applies to the air.
3) The air flow through a bleed orifice is assumed to be a quasi steady-state isentropic flow.
4) The discharge coefficient of all orifices is assumed to have constant value i.e. C=0.65 [35].

Mass Flow Rate through a Bleed Orifice

When a gas stored under pressure in a closed volume is discharged to the atmosphere through a hole or other opening, the gas velocity through that opening may be choked (i.e., has attained a maximum) or non-choked. Choked velocity, which is also referred to as sonic velocity, occurs when the ratio of the absolute source pressure to the absolute downstream ambient pressure is equal to or greater than $\left[\frac{\gamma+1}{2}\right]^{\frac{\gamma}{(\gamma-1)}}$, where γ is the specific heat ratio of the discharged gas. For many gases, γ ranges from about 1.09 to about 1.41, and thus $\left[\frac{\gamma+1}{2}\right]^{\frac{\gamma}{(\gamma-1)}}$ ranges from 1.7 to 1.9 which means that choked velocity usually occurs when the absolute source vessel pressure is at least 1.7 to 1.9 times as high as the absolute ambient atmospheric pressure.

When the gas velocity is choked, the equation for the mass flow rate is

$$\dot{m} = (CAP_u)\sqrt{\left(\frac{\gamma g_c M}{RT}\right)\left(\frac{2}{(\gamma+1)}\right)^{\frac{(\gamma+1)}{(\gamma-1)}}} \qquad \textbf{(4. 20)}$$

Here, the terms P_u is the pressure upstream of the orifice, A is area of the orifice, C is the discharge constant, M is air molecular weight, R is the universal gas law constant, T is temperature, γ is the specific heat constant and g_c is an units conversion factor. The values of the all the constants are given the Table 4- 3.

Although the gas velocity reaches a maximum and becomes choked, the mass flow rate is not fixed and can still be increased if the source pressure is increased. This can be

explained as follows. With the increase in the pressure ratio across the orifice, the density of the air increases as given by equation 4.35.

Whenever the ratio of the absolute source pressure to the absolute downstream ambient pressure is less than $\left[\frac{\gamma+1}{2}\right]^{\frac{\gamma}{(\gamma-1)}}$, then the gas velocity is non-choked (i.e., sub-sonic) and the equation for the mass flow rate is,

$$\dot{m} = (CA\,P_u)\sqrt{\left(\frac{2g_c M}{RT}\right)\left(\frac{\gamma}{(\gamma-1)}\right)^{\frac{(\gamma+1)}{(\gamma-1)}}\left(\left(\frac{P_d}{P_u}\right)^{\frac{2}{\gamma}} - \left(\frac{P_d}{P_u}\right)^{\frac{(\gamma+1)}{\gamma}}\right)} \qquad \textbf{(4. 21)}$$

Here P_d is the pressure downstream of the orifice. Since the terms C, M, R, T, γ and g_c are constants (given in Table 4- 3), the mass flow rate can be expressed as,

$$\dot{m} = f_{nc}(A, P_u, P_d) \qquad \textbf{(4. 22)}$$

If $\left(\frac{P_d}{P_u}\right) \geq 1.8$ then the flow is choked, therefore equation 4.20 will be valid.

If $\left(\frac{P_d}{P_u}\right) < 1.8$ then the flow isn't choked, therefore equation 4.21 will be valid.

The function form of the equation 4.20 and 4.21 will be used instead of rewriting the entire equation.

As an example Figure 4- 4 shows the mass flow rates through an orifice with diameter 6 mm for different ratios of $\left(\frac{P_d}{P_u}\right)$ ranging from 1 to 4. A sharp change in mass flow rates can be observed when the flow is choked at $\left(\frac{P_d}{P_u}\right) = 1.8$.

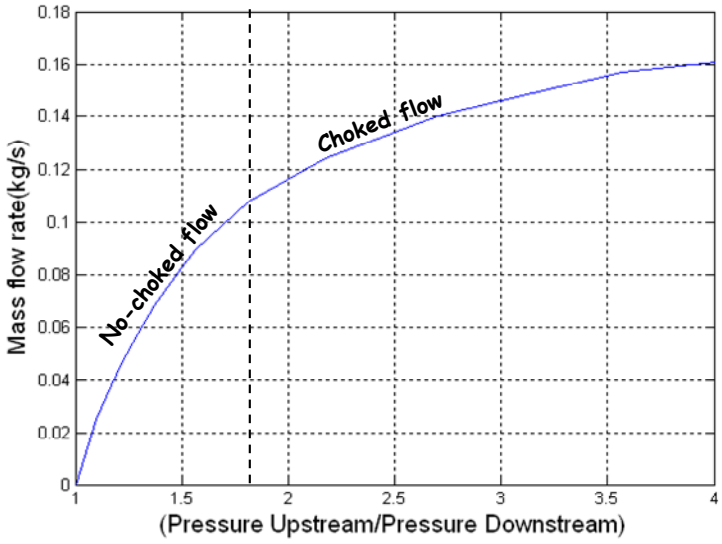

Figure 4- 4: Effect of choking phenomenon on mass flow rate

Calculation of the Pressure inside a Control Volume

In this section an example is presented which illustrates the calculation of pressure inside a control volume as can be seen in Figure 4- 5 . The control volume is supplied with pressure P_{supply} which is greater than internal chamber pressure P_i. There is also an exhaust port which releases P_i to the atmosphere.

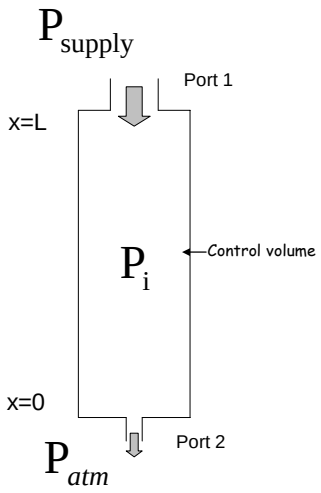

Figure 4- 5 : Fluid flow model of control volume

Using equation 4.22, the mass flow rate entering into the control volume is given by,

$$\dot{m}_{in} = f(A_{port1}, P_{supply}, P_i) \quad \textbf{(4. 23)}$$

and the mass flow rate leaving the control volume is given by,

$$\dot{m}_{out} = f(A_{port2}, P_i, P_{atm}) \quad \textbf{(4. 24)}$$

Total mass of fluid inside the control volume at any time 't' is given by,

$$M_{total}(t) = M_{(t=0)} + \int_0^t (\dot{m}_{in} - \dot{m}_{out})dt \quad \textbf{(4. 25)}$$

The pressure inside the control volume V is given by the ideal gas equation,

$$P_i(t) = \frac{M_{total}(t)\,RT}{V} \quad \textbf{(4. 26)}$$

Calculation of the pressure inside a Control Volume with a Free Moving Piston

This section presents the example of a free moving piston placed in the control volume. In this case, the control volume gets subdivided into two smaller volumes and will be referred to as the upper chamber and the lower chamber. The important thing is that the piston is free to move and therefore the volumes of the chambers are not constant over time. Also the total force on the piston is calculated using the pressure differential between the two chambers. An exhaust port is added to the control volume as shown in the Figure 4- 6.

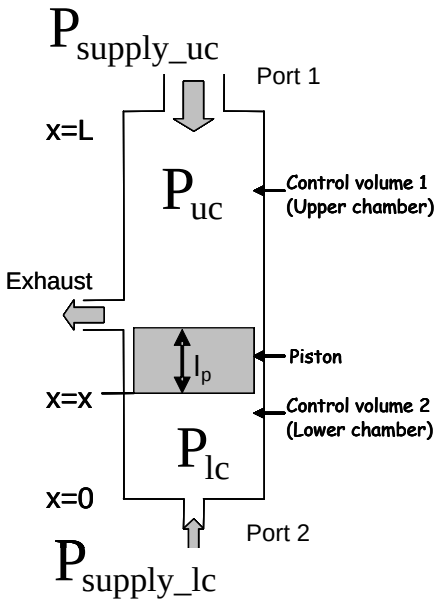

Figure 4- 6 : Fluid flow model of a control volume with a moving piston inside

Using equations for the mass flow rate to the upper chamber and the lower chamber, the pressure in the upper chamber and lower chamber can be calculated.

Using equation 4.22, the mass flow rate entering into the upper chamber is given by,

$$\dot{m}_{in\_uc} = f\,(A_{port1}, P_{uc}, P_{supply\_uc}) \qquad \textbf{(4. 27)}$$

Here A_{port1} is area of the port1, P_{uc} is the pressure in the upper chamber and P_{supply_uc} is the supply pressure. The mass flow rate leaving the control volume is given by,

$$\dot{m}_{out\_uc} = f(A_{exhaust}, P_{uc}, P_{atm}) \qquad \textbf{(4. 28)}$$

Here $A_{exhaust}$ is the area of the exhaust port and P_{atm} is the atmospheric pressure. If the mass flow rate is calculated using equation 4.22, then the pressure in the upper chamber P_{uc} can be calculated using the formulation given by equation 4.27. This assumes that the exhaust port is not blocked by the piston as shown in Figure 4- 6. If it is blocked by the piston, then

$A_{exhaust}$ and $\dot{m}_{out\_uc}$ will be zero. Following a similar procedure for the lower chamber, the pressure in the lower chamber P_{lc} can also be calculated. The net force acting on the piston at any time 't' can be calculated by multiplying the differential pressure by the cross sectional area,

$$F_{piston}(t) = A(P_{uc}(t) - P_{lc}(t)) \quad \textbf{(4. 29)}$$

4.1.3. Coupling between the Structural and Fluid Model

In addition to the displacement and velocity of the individual components of the structural model, the masses of air in the upper and lower chambers must also be formulated as states. The mass of air in the upper chamber m_{uc} and the mass of air in the lower chamber m_{lc} are calculated by integrating the difference between the mass flow rate entering and leaving the respective chambers as explained in detail in section 4.2.2. The mass flow rates are a function of time and can not be modeled as part of the state matrix in the state space formulation. Runge-Kutta-4 was used for numerically integration. Here they are modeled as augmented state vectors and can be written as,

$$\dot{y}_a(t) = \begin{bmatrix} \dot{y}(t) \\ \dot{m}_{uc}(t) \\ \dot{m}_{lc}(t) \end{bmatrix} \quad \textbf{(4. 30)}$$

The resulting vector $y_a(t)$ would give the displacement and the velocity of all the masses in the structural model and the mass of air in upper and lower chamber.

4.2. Modeling an Atlas Copco TEX-317

This section deals with measurement and estimation of parameters such as mass and stiffness for the Atlas–Copco TEX-317 impact hammer. Some parameters such as the masses of the components of the impact hammer can be measured directly. Other parameters such as the mass and stiffness of the hand as well as the stiffness of ground are obtained from literature [33]. Finally, some variables such as stiffness and damping between components need to be estimated and adjusted using the model.

4.2.1. Extraction of the Stiffness and Damping between Components

Calculating the correct stiffness and damping terms are important for the structural model. To get stiffness values for individual components, finite element models of the individual components were built. A distributed unit force was applied to the finite element model and the corresponding deformation for the model was used to estimate the stiffness. Together these stiffness values were used to estimate the stiffness between elements.

Hand and Ground

The damping and stiffness values for the hand mass and the ground were obtained from literature [33]. However the parameters for the human hand change from individual to individual and the same apply to the different ground conditions as well. Therefore the stiffness and damping values of the hand and ground can be varied to account for these changes.

Handle

A distributed load was applied to the handle at the area where the hand grips the handle. The base of the handle was fixed and the deformation caused by that force was used to calculated the stiffness as k=1.75e7 N/m.

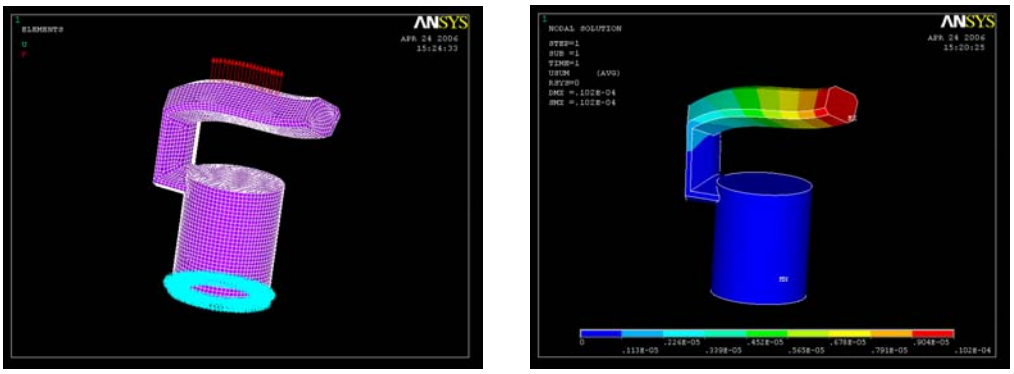

Figure 4- 7 : Finite element model of the handle

Center body

Similarly the center body was subjected to distributed-loading at the top where it connects with the handle and the base fixed. The deformation at the top was measured and the calculated stiffness is given by k=1.4749e7 N/m

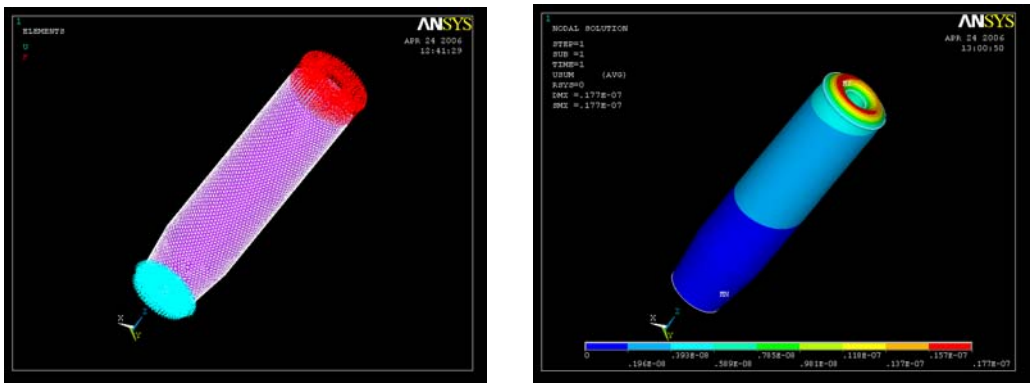

Figure 4- 8 : Finite element model of the center body

Chisel

Chisel is impacted by the piston at the top therefore the distributed forces have applied to the top of the chisel. The maximum deformation also occurs at the top end. The associated stiffness is given by, k=3.7244e7 N/m

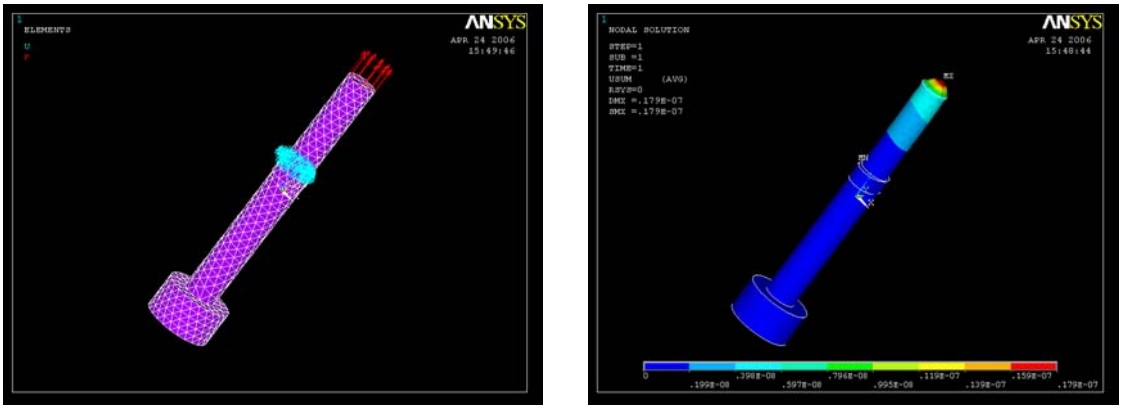

Figure 4- 9 : Finite element model of chisel

The stiffness for the impact was assumed to be very large compared to the component stiffness and was arbitrarily chosen as 3e9 N/m. The stiffness and damping terms used in the model are function of stiffness and damping terms of the two connected components. Therefore these values can't be used as they are but act as a guide to find the true values. After numerous trial and errors, the stiffness and damping values of the lumped masses were obtained so as to match the structural dynamic model as closely as possible. Following tables list the stiffness and damping terms used in the numerical model. It should be noted that the values of k_cb_ch and c_cb_ch are nonlinear in nature as explained in the previous section.

Table 4- 1: Stiffness' of the lumped masses (N/m).

Parameter	Value
k_hd	3.9478e5
k_hd_hdl	6e3
k_hdl_cb	1.5e7
k_cb_ch	4e8
k_ch_gd	3e5

Table 4- 2 : Damping terms of the lumped masses (Ns/m).

Parameter	Value
c_hd	30
c_hd_hdl	40
c_hdl_cb	k_hdl_cb*0.0001
c_cb_ch	6000
c_ch_gd	6000
c_friction	0.00001

=

More work is required to find more accurate stiffness and damping parameters. This can be done by building more detailed assembly model of the impact hammer with correct set of contact elements between different components.

4.2.2. Case Dependent Calculation of the Mass Flow Rate in the Upper and Lower Chamber

Figure 4- 10 shows all the potential fluid flow pathways for of the Atlas Copco impact hammer. The impact hammer is divided into three closed volumes as shown in the control volume-(1) Source Chamber, control volume-(2) Upper chamber (chamber above piston) and control volume-(3) Lower chamber (chamber below the piston). Source chamber pressure is assumed to be constant i.e. 90 psi as it is directly connected to the air supply line. The source chamber is connected to the upper and lower chamber through a pneumatic on-off valve. At any instant in time, the source chamber is either connected to the upper

chamber or lower chamber. The switching of the pneumatic valve is dependent on the relative pressures in upper or lower chamber. The pressure in the upper and lower chamber depends on the position of the piston in the chamber. Changes in the position of the piston cause change in both pressures.

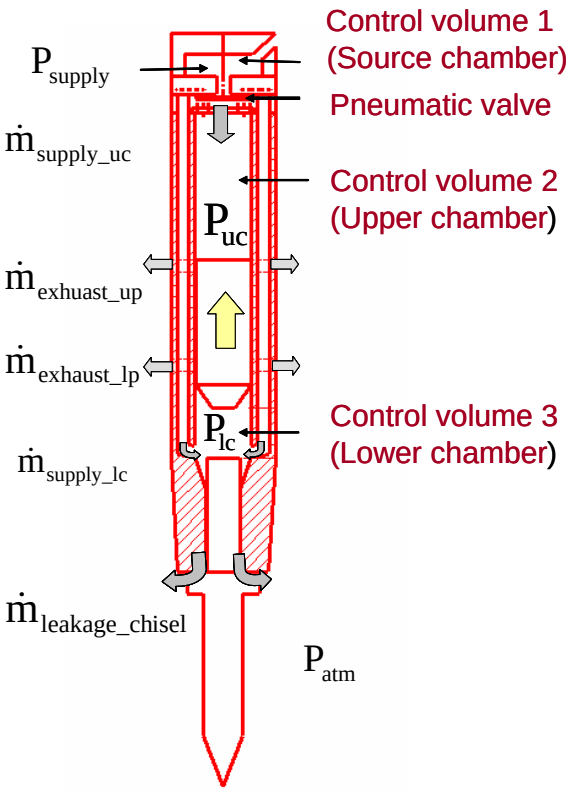

Figure 4- 10 : Potential fluid flow pathways of impact hammer

The force applied on the piston is a product of the cross sectional area of the bore of the center body and the difference in pressures on both sides of the piston. For each time step during the simulation this force is calculated. The force will cause the piston to accelerate and move to a different position which in turn causes the pressures to change in both chambers. As the piston moves up and down, it closes or opens up the upper and lower exhaust ports. As the exhaust ports opens up it exposes pressure inside a potential chamber

to atmospheric pressure. Thus these actions allow the cyclic nature of the pneumatic impact hammer operation. Some leakage is allowed around the piston from the upper chamber to the lower chamber and also around the chisel from the lower chamber to atmosphere. In addition the model allows flow to reverse in cases where the pressure in any of the chambers increases or decreases abnormally.

Figure 4- 11 illustrates the general flow chart of the overall numerical model of the pneumatic impact hammer. There are four main components, (i) input parameters and initial conditions (Green), (ii) the structural dynamic model (yellow), (iii) the fluid model (blue) and (iv) the coupling (purple). In the fluid part of the model the position of the piston is evaluated and depending on the location, the model decides which particular case to use. The cases in the numerical model are based on the different events discussed in section 2.2. The different cases for this particular impact hammer are discussed in this section.

Initial Conditions

The initial conditions for the air mass in the upper and lower chamber are as follows,

$$\left.\begin{aligned} M_{uc}(0) &= M_{uc\_0} \\ M_{lc}(0) &= M_{lc\_0} \end{aligned}\right\} \qquad \textbf{(4. 31)}$$

In addition to this, the initial conditions for the displacement and velocity of all the masses are given as,

$$x(0) = x_0 \quad \text{and} \quad \dot{x}(0) = \dot{x}_0; \qquad \textbf{(4. 32)}$$

Calculation of Volume

The volumes of the upper and lower chamber are required to calculate the pressures in the upper and lower chambers using an ideal gas equation as given in equation 4.27 and they are given by,

$$V_{uc} = A(L - x - l_p) \quad \textbf{(4. 33)}$$

$$V_{lc} = Ax \quad \textbf{(4. 34)}$$

Therefore the net force on the piston can be calculated as shown in equation 4.30. The force on the piston is substituted into force vector i.e. right hand side of equation 4.1 which is then solved iteratively to calculate the dynamic response of the system.

At this point the position of the piston is again evaluated. Depending on that a particular test case is chosen using series of conditional statements. Each of the cases is explained in detail below. The net mass flow rates coming into the upper and lower chambers are then calculated using equation 4.67 and equation 4.68.The exhaust jet velocity is assumed to be directly proportional to the mass flow rate coming out of the exhaust ports and is given by the following expression,

$$V_{exhaust} = \frac{\dot{m}_{exhust}}{\rho * A} \quad \textbf{(4. 35)}$$

Where, ρ is the atmospheric density of air and A is the cross-sectional area of the exhaust port. It is assumed that the density of air remains constant. This is only a rough approximation as it is known that the density of air is a function of air pressure and that the velocity varies as the flow expands on the downstream side of the orifice.

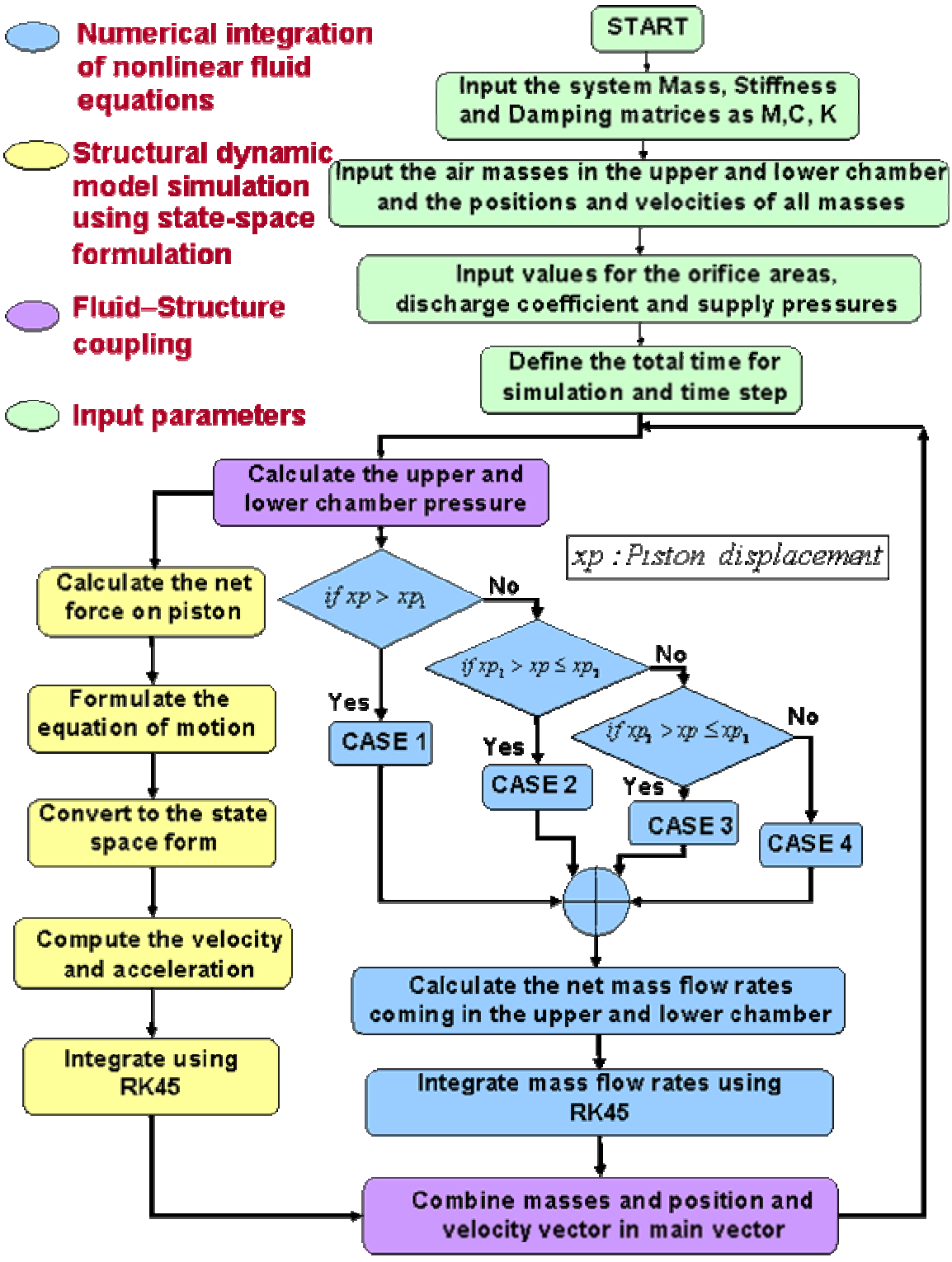

Figure 4- 11 : General flow chart to calculate time varying forcing input

Case 1: When both the exhaust ports are interacting with lower chamber (xp <0.09m)

In this case the piston is right at the top of the piston stroke. Figure 4- 12 explains the algorithm for Case1 as an example. The net flow in the upper chamber is indicated by 1 and the net flow in the lower camber is indicated by 2.

a) Supply pressure is given to the upper chamber by the pneumatic valve.

$$\dot{m}_{supply\_uc} = f(A_{supply\_orifice\_uc}, P_{supply\_uc}, P_{uc}) \quad \textbf{(4. 36)}$$

$$\dot{m}_{supply\_lc} = 0 \quad \textbf{(4. 37)}$$

b) The lower exhaust ports are opened to the lower chamber.

$$\dot{m}_{exhaust\_lp} = f(A_{exhaust\_lp}, P_{lc}, P_{atm}) \quad \textbf{(4. 38)}$$

c) The upper exhaust ports are opened to the lower chamber.

$$\dot{m}_{exhaust\_up1} = f(A_{exhaust\_up}, P_{lc}, P_{atm}) \quad \textbf{(4. 39)}$$

$$\dot{m}_{exhaust\_up2} = 0 \quad \textbf{(4. 40)}$$

d) The leakage flow is given by

$$\dot{m}_{leakage\_piston} = f(A_{leakage\_piston}, P_{uc}, P_{lc}) \quad \textbf{(4. 41)}$$

$$\dot{m}_{leakage\_chisel} = f(A_{leakage\_chisel}.P_{uc}.P_{atm}) \quad \textbf{(4. 42)}$$

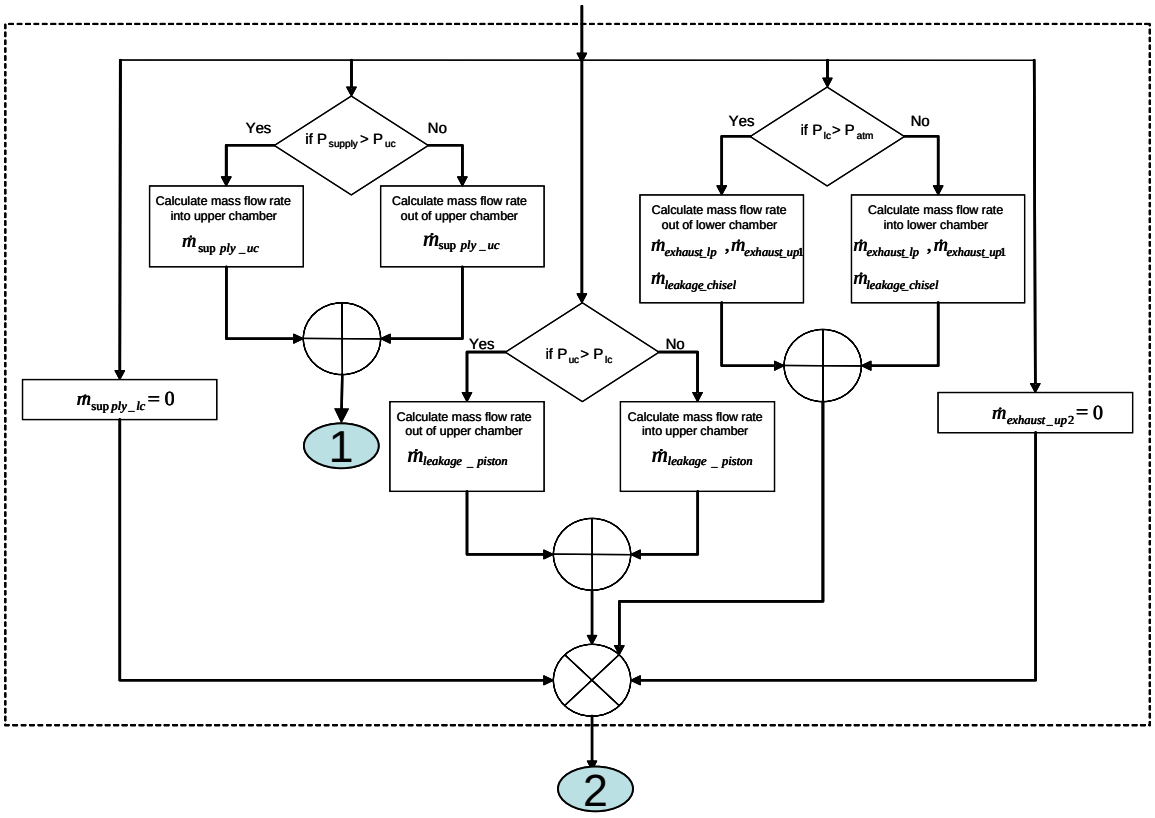

Figure 4- 12: Flow chart for Case 1

Case 2: When only lower exhaust ports are interacting with lower chamber and upper ports are blocked by piston (0.09m > xp > 0.04m)

a) Supply pressure is given to the upper chamber by the pneumatic valve.

$$\dot{m}_{supply\_uc} = f(A_{supply\_orifice\_uc}, P_{supply\_uc}, P_{uc}) \quad \textbf{(4. 43)}$$

$$\dot{m}_{supply\_lc} = 0 \quad \textbf{(4. 44)}$$

b) The lower exhaust ports are opened to the lower chamber.

$$\dot{m}_{exhaust\_lp} = f(A_{exhaust\_lp}, P_{lc}, P_{atm}) \quad \textbf{(4. 45)}$$

c) The upper exhaust ports are blocked by the piston.

$$\dot{m}_{exhaust\_up1} = 0 \quad \textbf{(4. 46)}$$

$$\dot{m}_{exhaust\_up2} = 0 \quad \textbf{(4. 47)}$$

d) The leakage flow is given by

$$\dot{m}_{leakage\_piston} = f(A_{leakage\_piston}, P_{uc}, P_{lc}) \quad \textbf{(4. 48)}$$

$$\dot{m}_{leakage\_chisel} = f(A_{leakage\_chisel}.P_{uc}.P_{atm}) \quad \textbf{(4. 49)}$$

Case 3: When both the ports are blocked by the piston (0.04m > xp > 0.035m)

There are two different sub cases in the case 3.

I) when piston is moving downward

a) Supply pressure is to given the lower chamber by the pneumatic valve.

$$\dot{m}_{supply\_uc} = f(A_{supply\_orifice\_uc}, P_{supply\_uc}, P_{uc}) \quad \textbf{(4. 50)}$$

$$\dot{m}_{supply\_lc} = 0 \quad \textbf{(4. 51)}$$

b) The lower exhaust ports are blocked by the piston

$$\dot{m}_{exhaust\_lp} = 0 \quad \textbf{(4. 52)}$$

c) The upper exhaust ports are blocked by the piston.

$$\dot{m}_{exhaust\_up1} = 0 \quad \textbf{(4. 53)}$$

$$\dot{m}_{exhaust\_up2} = 0 \quad \textbf{(4. 54)}$$

d) The leakage flow is given by

$$\dot{m}_{leakage\_piston} = f(A_{leakage\_piston}, P_{uc}, P_{lc}) \quad \textbf{(4. 55)}$$

$$\dot{m}_{leakage\_chisel} = f(A_{leakage\_chisel}.P_{uc}.P_{atm}) \quad \textbf{(4. 56)}$$

II) When the piston is moving upward

Same as above but with the supply pressure changed.

a) Supply pressure is to given the lower chamber by the pneumatic valve.

$$\dot{m}_{supply\_uc} = 0 \quad \textbf{(4. 57)}$$

$$\dot{m}_{supply\_lc} = f(A_{supply\_orifice\_lc}, P_{supply\_lc}, P_{lc}) \quad \textbf{(4. 58)}$$

Case 4: When upper ports are interacting with the upper chamber and lower ports are blocked by piston (xp <0.022m)

Here the pneumatic valve flips and the supply pressure's applied to the lower chamber.

a) Supply pressure is to given the lower chamber by the pneumatic valve.

$$\dot{m}_{supply\_lc} = f(A_{supply\_orifice\_lc}, P_{supply\_lc}, P_{lc}) \quad \textbf{(4. 59)}$$

$$\dot{m}_{supply\_uc} = 0 \quad \textbf{(4. 60)}$$

b) The lower exhaust ports are blocked by the piston

$$\dot{m}_{exhaust\_lp} = 0 \quad \textbf{(4. 61)}$$

c) The upper exhaust ports are opened to the upper chamber.

$$\dot{m}_{exhaust\_up2} = f(A_{exhaust\_up}, P_{uc}, P_{atm}) \quad \textbf{(4. 62)}$$

$$\dot{m}_{exhaust\_up2} = 0 \quad \textbf{(4. 63)}$$

d) The leakage flow is given by

$$\dot{m}_{leakage\_piston} = f(A_{leakage\_piston}, P_{uc}, P_{lc}) \quad \textbf{(4. 64)}$$

$$\dot{m}_{leakage\_chisel} = f(A_{leakage\_chisel}.P_{uc}.P_{atm}) \quad \textbf{(4. 65)}$$

At any point in time, one of these cases would be true. All the individual mass flow rates are calculated from that particular case and then the net mass flow rates into the upper and the lower chamber are calculated as following.

$$\dot{m}_{uc} = \left(\dot{m}_{supply\_uc} - \dot{m}_{exhaust\_up2} - \dot{m}_{piston\_leakage}\right) \quad \textbf{(4. 66)}$$

$$\dot{m}_{lc} = \left(\dot{m}_{supply\_lc} - \dot{m}_{exhaust\_up1} - \dot{m}_{exhaust\_lp} - \dot{m}_{chisel\_leakage}\right) \quad \textbf{(4. 67)}$$

The mass flow rates are then integrated to calculate the net masses of air in the upper and lower chamber. Resultant masses of air in the upper and lower chambers will act as new initial conditions to calculate the pressures inside the upper and lower chamber which in

turn will determine the effective force on the piston. This iterative procedure to calculate the pressures, states and forces on the piston will continue until the simulation time ends. Following table includes all the values of the parameters used in this model. The values for stiffness, damping and masses of the lumped components are already listed

Table 4- 3: Values of the parameters used in the model

Parameters used in the model	Values
m_{hd}	2 kg
m_{hdl}	1.5 kg
m_{cb}	2.180 kg
m_{pst}	0.362 kg
m_{ch}	5.515 kg
C	0.65
g_c	1 kg m / N-s ^{2}
γ	1.4
ρ	1.2 kg/ m ^{3}
M	29e-3 kg
R	1545.3 (ft-lb) / (lbmol) (°K)
Z	1
P_{supply_uc}	90 psi
P_{supply_lc}	90 psi
P_{atm}	14.7 psi
$A_{supply\_orifice\_uc}$	$6*(\pi/4)*(6e-3)^2$ m^2

$A_{supply\_orifice\_lc}$	$6*(\pi/4)*(6e-3)^2$ m^2
$A_{exhaust\_up}$	$2*(\pi/4)*(6e-3)^2$ m^2
$A_{exhaust\_lp}$	$2*(\pi/4)*(6e-3)^2$ m^2
A_{bore}	$(\pi/4)*(29e-3)^2$ m^2
$A_{leakage\_piston}$	$(\pi/4)*((29e-3)^2-(28.8e-3)^2)$
l_{stroke}	102e-3 m
l_{piston}	78e-3 m

4.2.3. Simulation Result of the Numerical Model

A simulation result of the numerical model is presented here. Figure 4- 13 (a) shows the displacements of all the lumped masses. Figure 4- 13 (b) shows the pressure profiles in the upper and lower chambers and Figure 4- 13 (c) shows the accelerations of the handle. Whenever the piston (cyan line) impacts the chisel (magenta line), sharp changes in the handle acceleration can be observed. It can also be noted that the piston never hits the center body at the top due to large pressure build up in the upper chamber. The exponential rise and decay in the pressure profiles can be seen. This happens when exhaust ports are closed or opened by the piston.

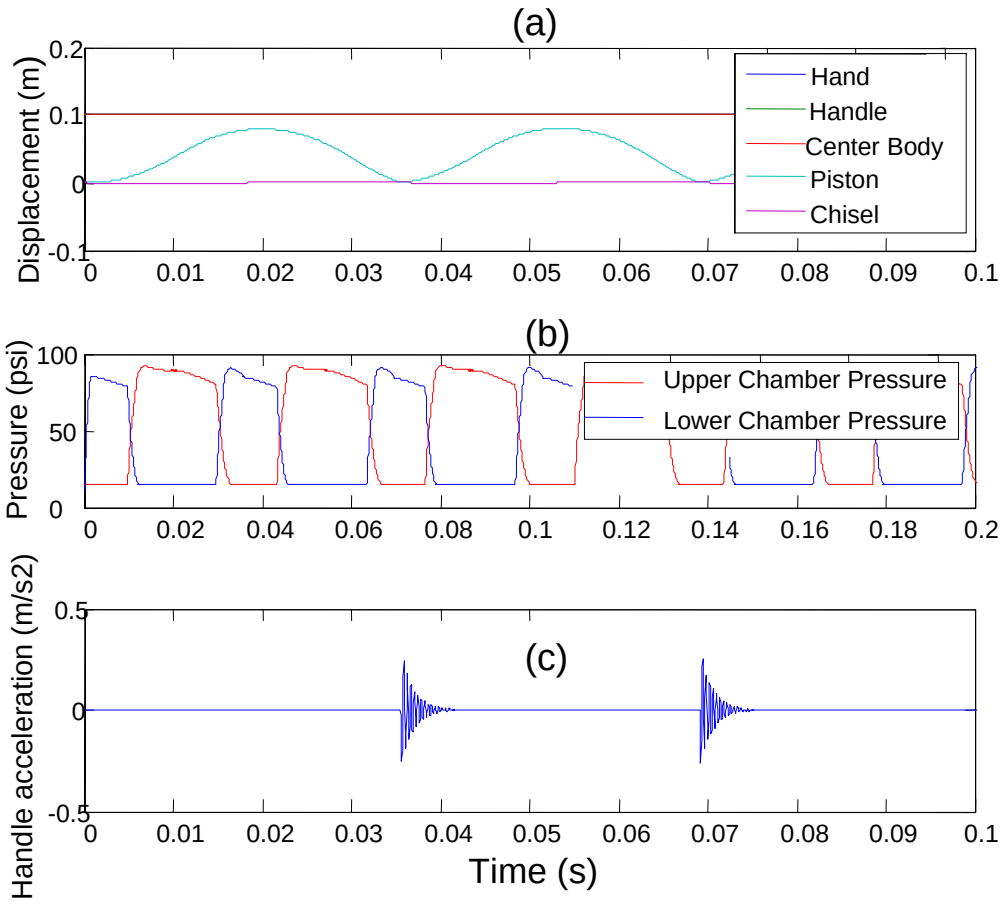

Figure 4- 13 : Simulation result of the numerical model (a) displacement of lumped masses, (b) upper and lower chamber pressure profiles and (c) accelerations of handle

4.2.4. Convergence of the Numerical Model

The convergence of the numerical model was evaluated by increasing the number of time steps for the simulation. Figure 4- 14 shows the exhaust jet velocity from the lower ports for different step sizes. The numerical solutions for 0.005 s and for 0.0005 s vary a lot from each other however the numerical solutions for 0.0005 s and 0.0003 s don't vary a lot. Therefore it can be assumed that the numerical model converges for a time step of 0.0005 s and this time step will be referred for all the simulations.

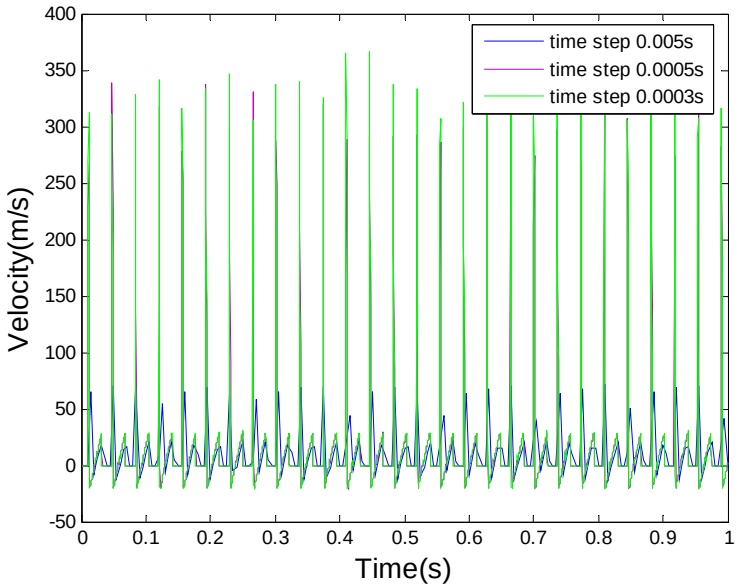

Figure 4- 14: Exhaust jet velocity from the lower ports

4.3. Experimental Tests to Validate the Numerical Model

Different experiments were carried out in order to validate the numerical model. These experiments include tool handle acceleration, hot film anemometer tests and pressure measurements in the upper and lower chamber of the impact hammer.

4.3.1. Tool Handle Acceleration Measurements

An accelerometer was mounted on the handle in the vertical direction to measure the tool handle acceleration. These accelerations are then calibrated and the power spectral density of the handle is computed. The experimentally measured power spectral density was compared with that of the numerically computed. Figure 4- 15 shows the accelerometer mounted on the handle marked by the circle.

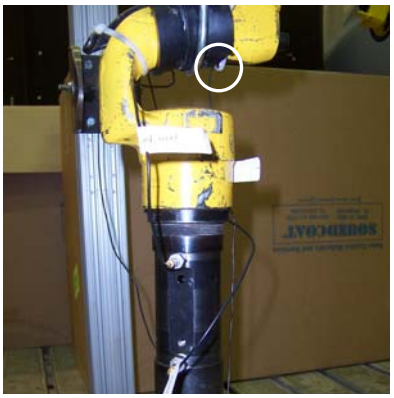

Figure 4- 15 : Handle acceleration measurement

4.3.2. Pressure Measurements in the Upper and Lower Chamber

Two different holes were drilled into the upper and the lower chamber of the impact hammer. The location of the holes was selected to be as far as possible from each other because that would help cover the maximum portion of the pressure cycle. However due to physical constraints, there is still a large portion of the cycle when the probes are blocked by the piston as represented by Figure 4- 16 and Figure 4- 17. Unfortunately the blocked portions of the cycle are those when the pressure in the chambers is the highest. During the tests the hammer was run and the both the chamber pressures were measured simultaneously. These measurements were then calibrated and compared with the numerical model results.

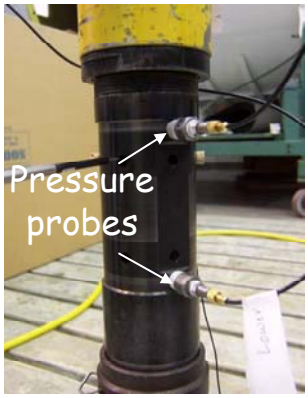

Figure 4- 16 : Pressure probe measurement

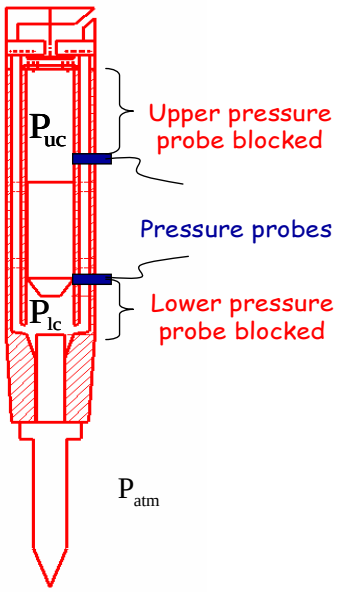

Figure 4- 17 : Schematic of the impact hammer showing the blocked portion of the cycle

4.3.3. Hot Film Anemometer Measurements

These tests and the set-up have explained previously in the section 2.3.1. Also the information about the experiment and the detailed analysis of the results have presented in by Schwartz [41].

4.4. Validation of the Numerical Model

In this section, the results obtained from the numerical model are compared to the experimental results.

4.4.1. Comparison of the Experimental and Numerical Exhaust Jet Velocities

Figure 4- 18 (a) and (b) shows the comparison between experimental and numerical exhaust jet velocities from the upper and lower exhaust ports. The results show a very good agreement both in the magnitude of the peaks as well as in the trends between them. Also

the tool impact frequency measured from the lab tests and the tool impact frequency calculated from the numerical model is approximately 27 Hz. Keeping in mind the nonlinear nature of the fluid flow model, these can be considered as very good results.

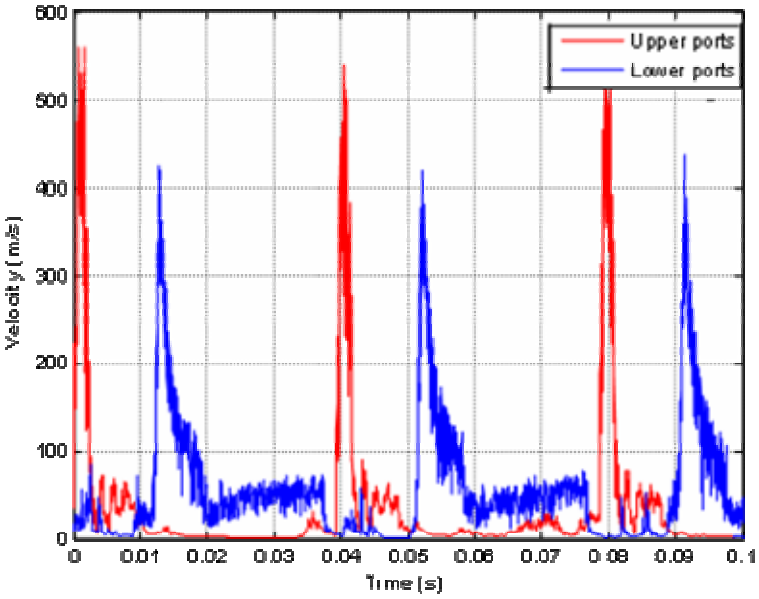

(a)

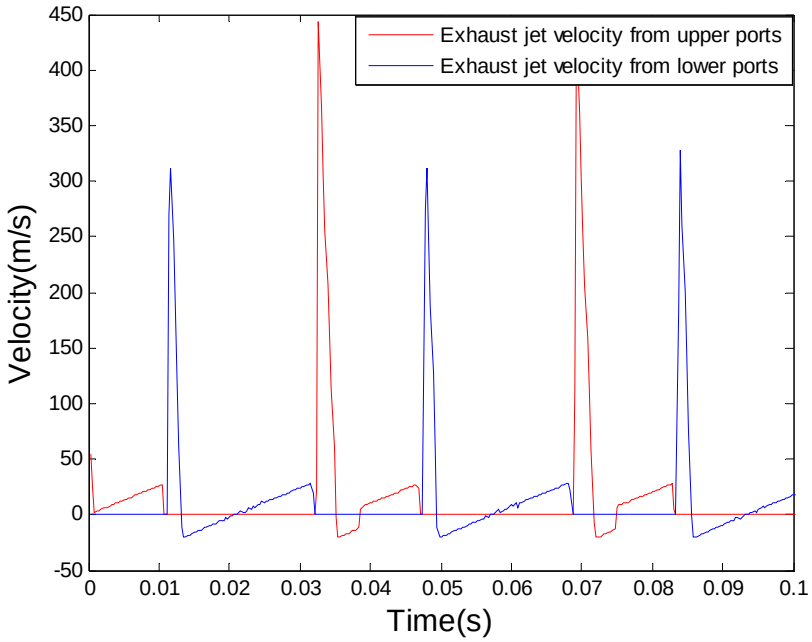

(b)

Figure 4- 18 : (a) Experimental and (b) predicted exhaust jet velocities from upper and lower ports.

4.4.2. Comparison of the Experimental and Numerical Pressures in the Upper and Lower Chambers

Figure 4- 19 shows the comparison between the experimental and numerical pressure profiles in the upper chamber. The upper pressure profiles obtained from the numerical model matches very well with the pressure profiles from the experimental tests. The model predicts the identical cycle timings as that of the experiments. Also the model predicts the pressure release point exactly to be the same as the experimental tests. Unfortunately the maximum pressure in the upper chamber couldn't be measured since the probe is blocked by the piston. To get the pressure profiles to match, the supply pressure in the numerical model was dropped to 75 psi. The drop of pressure is quite considerable compared to 90 psi supply pressure. The reasons behind the difference are not very clear but could be due to the pressure drops in through the supply valve.

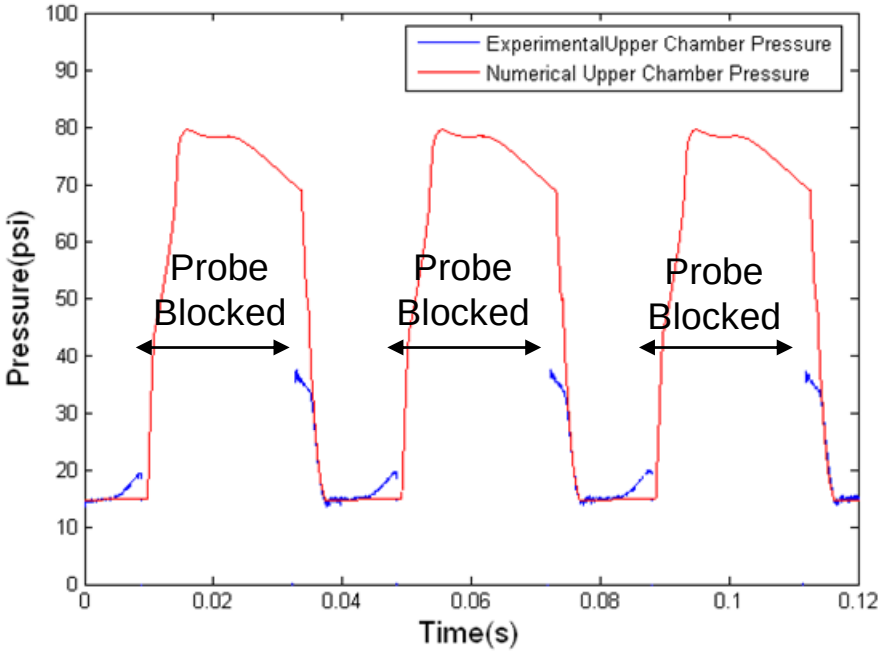

Figure 4- 19 : Comparison between the numerical and experimental upper chamber profiles

Figure 4- 20 illustrates the comparison between the experimental and numerical pressure profiles in the lower chamber. The lower chamber pressures profiles also match with the experimental pressure profile well with respect to the cycle timings. The release of the pressures from the lower chamber is exactly as predicted by the model. However the experimental results show the building of the pressures in the lower chamber is quite slow compared to the numerical model prediction. The pressure probe is blocked by the piston when the pressure in the chamber reaches the maximum value.

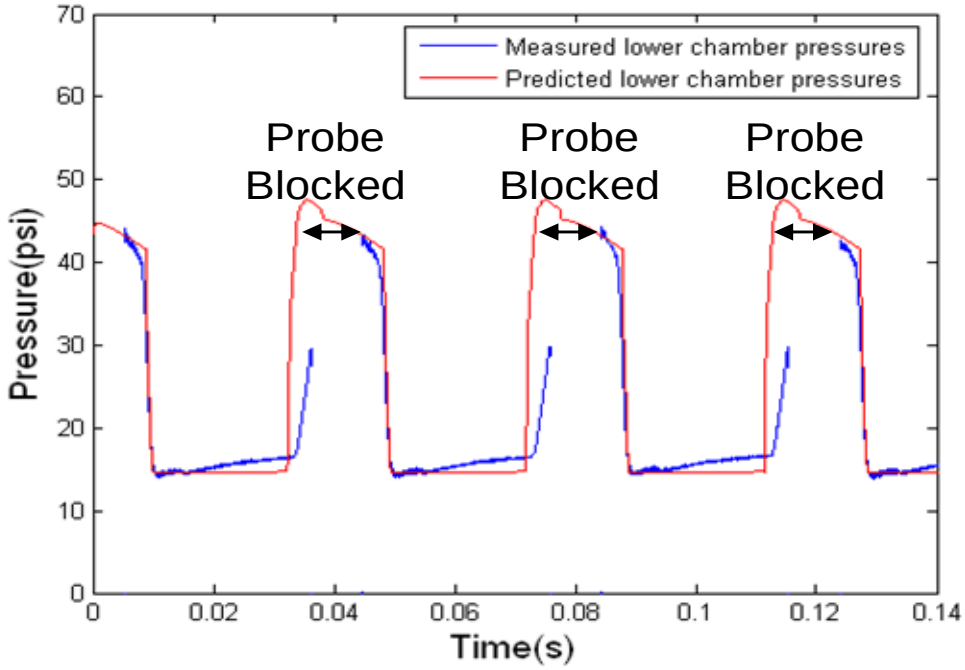

Figure 4- 20 : Comparison between the numerical and experimental lower chamber profiles

4.4.3. Comparison of the Structural Response of the Tool Handle

The experimentally measured power spectral density of the tool handle accelerations compared with that of the numerically computed the power spectral density of the tool handle as can be seen in Figure 4- 21. The numerically computed levels of accelerations

match very well with that of the experimentally measured. The model also predicts the 500 Hz handle resonance successfully. However, the model over-predicts the higher frequency vibrations. Overall the numerical response shows the same trends. The difference in the two results could be due to the fact that the model assumes dynamics of the ground and support (hand) that are not same as those tested experimentally.

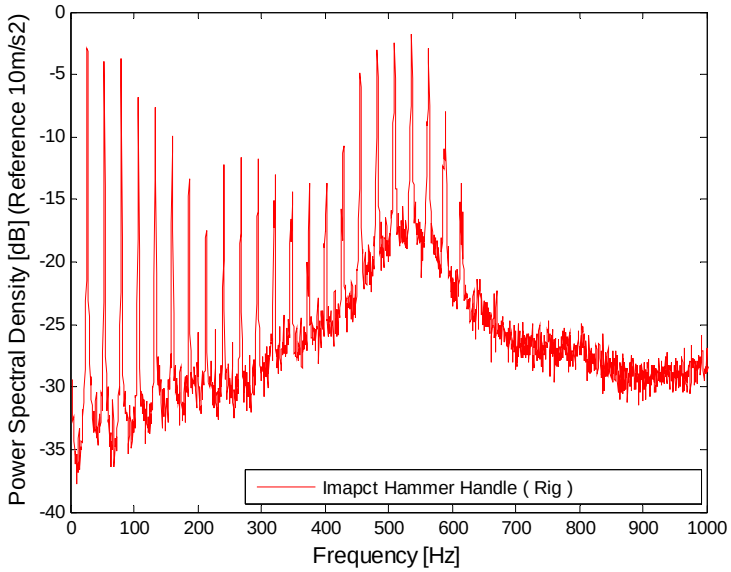

(a)

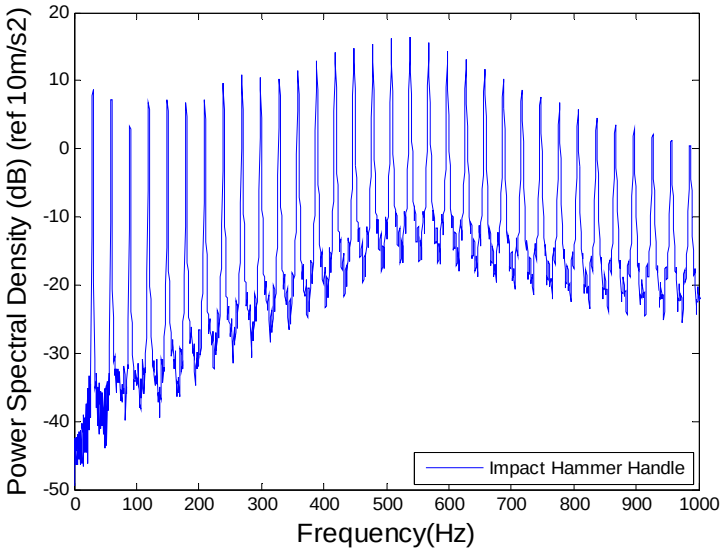

(b)

Figure 4- 21 : Comparison between the power spectral densities of the tool handle (a) experimental result, (b) numerical result

Chapter 5. Parametric Study using the Numerical Model

In this chapter, the numerical model was used to explore the different vibration control techniques and to investigate the changes in the tool behavior. The objective behind this exercise was only to demonstrate the potential of the numerical model and therefore the solutions provided here may not be implemented practically. The approach followed was to change the various structural and fluid parameters in the model and compute the tool response for example the handle vibration. The results obtained from these simulations are presented in this chapter.

5.1. Relation between the Primary Impact Frequency and the Supply Pressure

Figure 5- 1 shows the relationship between the supply pressure and the primary impact frequency. The primary impact frequency is important since it determines the work efficiency. The supply pressure was increased and the input frequency determined by observing the first harmonic in the auto-spectrum of the system vibration. The relationship between the supply pressure and the impact frequency is approximately linear before 85 psi. However rate of increase in the impact frequency became slightly slower after the 85 psi.

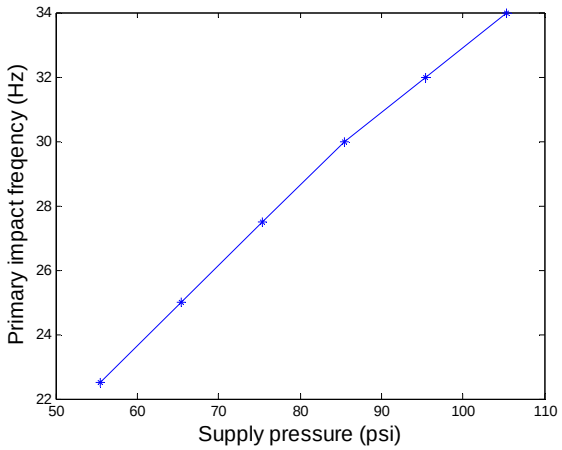

Figure 5- 1 : The relationship between the supply pressure and the primary impact frequency

5.2. Changes in the Tool Handle Parameters

In this section, the effect of changing the handle parameters on the tool response will be presented.

5.2.1. Effect of the D-handle

Figure 5- 3 shows the effect of the D-handle on the tool handle's power spectral density. It has been mentioned before that the bending mode shape of the tool handle is responsible for the 540 Hz resonance. This resonance could be a principal cause for finger injuries. The resonance at 540 Hz can be pushed beyond the frequency range of interest (0-1000 Hz) by increasing the stiffness of the handle. This can be simply achieved by changing the C-shape handle into a D-shape handle which would increase the stiffness significantly at the expense of small addition of weight. A finite element model was used to determine that the D-handle increases the stiffness by a factor of approximately 10 (i.e. 1.5e8 N/m). Implementation of D-handle resulted in vibration attenuation of 10 dB at 540 Hz resonance. The D-handles are used in commercial impact hammers nowadays.

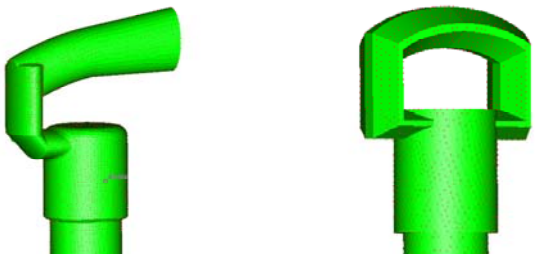

(a) (b)

Figure 5- 2 : Finite element model of (a) C-handle, (b) D-handle

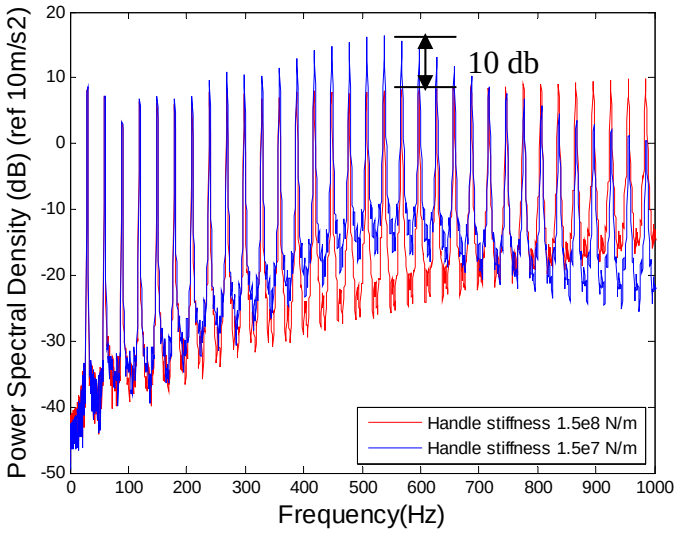

Figure 5- 3 : Effect of the D-handle on the tool handle's power spectral density

5.2.2. Changing the Handle Damping

Figure 5- 4 shows the effect of the increasing handle damping by a factor of 2 on the tool handle's power spectral density. The increase in the handle damping reduced the amplitude of the handle resonance by 5-6 db at 540 Hz. But there is no change in the primary impact and the low frequency vibration amplitudes. The handle damping could be increased by adding some visco-elastic damping to the handle.

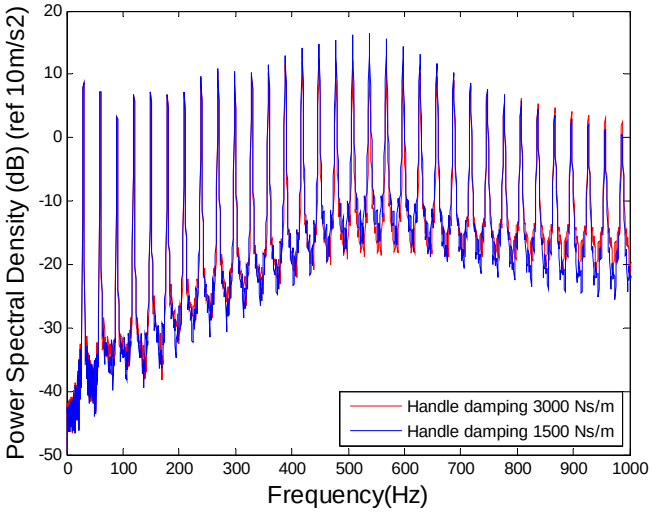

Figure 5- 4: Effect of the increasing damping on the tool handle's power spectral density

5.2.3. Changing the Handle Weight

Figure 5- 5 illustrates the effect of the increase in the handle weight by a factor of 2 on the tool handle's power spectral density. The increase in the handle weight reduces the frequency of handle resonance from 540 Hz to 390 Hz. However the handle weight doesn't have any effect on the levels at the primary impact frequency.

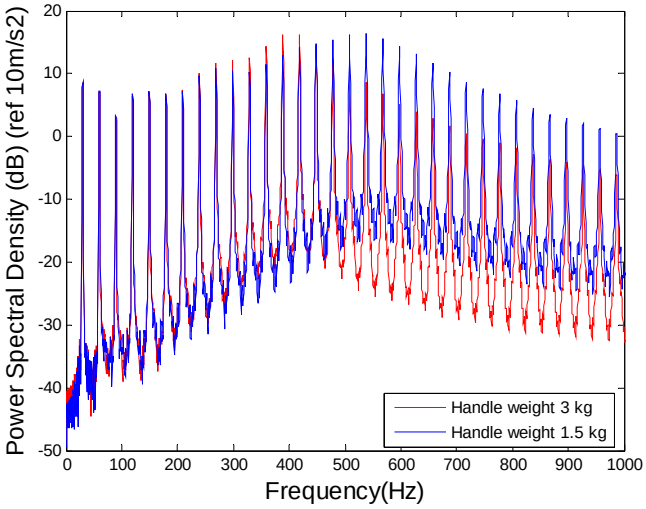

Figure 5- 5 : Effect of the increase in the handle weight on the tool handle's power spectral density

5.3. Changing the Piston Weight

Figure 5- 6 demonstrates the effect of the increased piston weight on tool handle's power spectral density. The increase in the piston weight would necessitate more force to accelerate it and in turn it would reduce the maximum velocity of the piston. Therefore the increase in the piston weight reduces the primary impact frequency by 3 Hz. The reduced piston velocity attenuates the amplitude and the frequency of the primary impact between the piston and the chisel. However the overall the power spectral density spectrum has very similar trends.

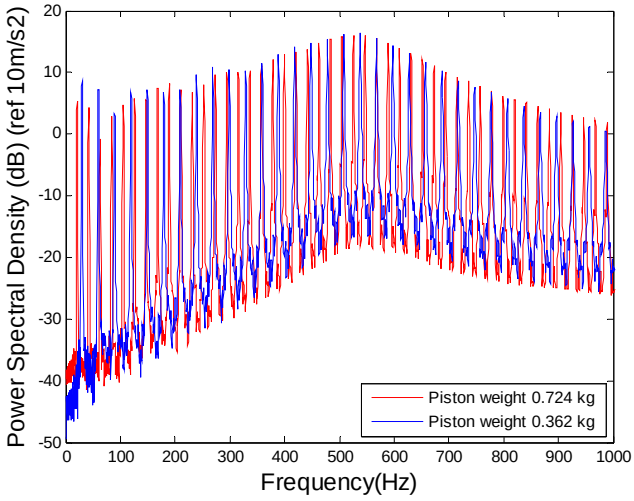

Figure 5- 6: Effect of the increased piston weight on tool handle's power spectral density

5.4. Changing the Chisel Weight

Figure 5- 7 shows the effect of the increase in the chisel weight by a factor of 3 on the tool handle's power spectral density. The increase in the chisel weight causes the higher frequency vibrations to reduce in the range 3-6 db. However the levels at the primary impact frequency between the chisel and impact remain unchanged. It should be noted that changes in the chisel are easier to implement in practice than changes in the tool itself.

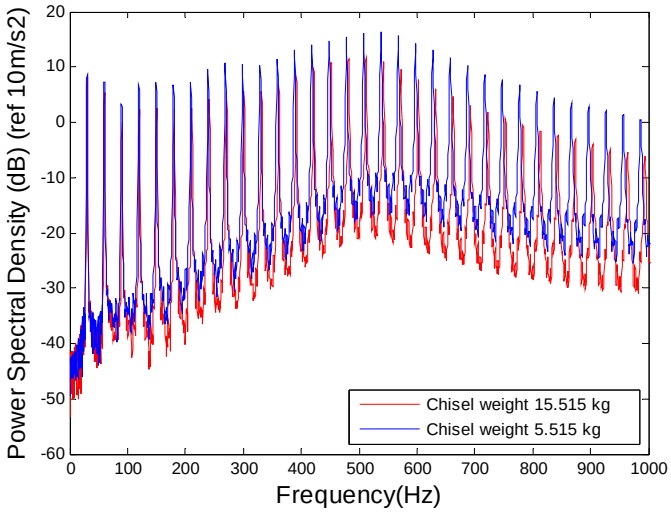

Figure 5- 7 : Effect of the increase in chisel weight on tool handle's power spectral density

5.5. Changes in the Impact Parameters between the Piston and Chisel

In this section, the effects of the changes in the impact parameters between the piston and chisel on the tool response are presented.

5.5.1. Changing the Impact Stiffness between the Chisel and Piston

Figure 5- 8 shows the effect of changing the stiffness between the piston and chisel by a factor of 10 on the tool handle's power spectral density. With the decrease in the stiffness between the chisel and the piston the accelerations at the handle reduce by about 3-5 db. In addition to this, the primary impact frequency also reduces. The overall nature of the power spectral density spectrum remains unchanged.

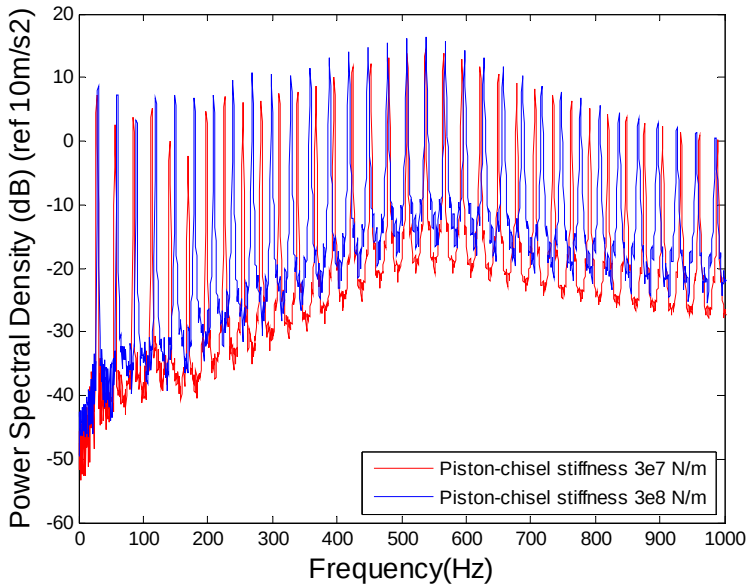

Figure 5- 8: Effect of the stiffness between the piston and chisel on the tool handle's power spectral density

5.5.2. Changing the Damping between the Chisel and Piston

Figure 5- 9 shows the effect of changing the damping between the chisel and piston on the tool handles' power spectral density. The increase in the damping between chisel and piston cause the primary impact frequency to reduce by 2 Hz and also the amplitude of the primary impact frequency to reduce by 2 db. In addition to this, the amplitude across the frequency range also reduces in the range 2-10 db. However this is likely to strongly reduce the effectiveness of the tool.

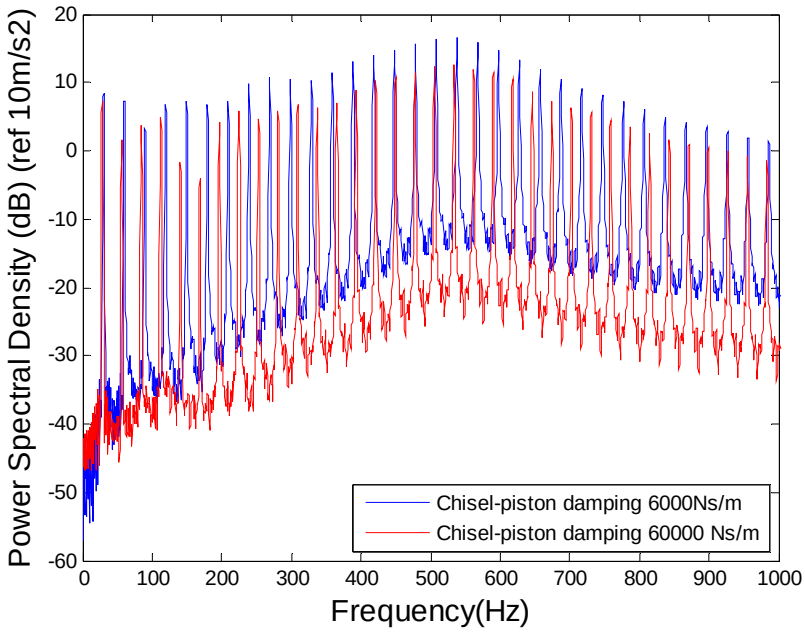

Figure 5- 9: Effects of increasing the damping between the chisel and piston on the tool handle's power spectral density

5.6. Change in the Impact Parameters between the Chisel and Center Body

In this section, the effects of the changes in the impact parameters between the chisel and center body on the tool response will be presented.

5.6.1. Changing the Stiffness between the Chisel and the Center Body

Figure 5- 10 shows the effect of the increase in the chisel-center body stiffness on the tool handle's power spectral density. The impacts occur between the chisel and the piston which thrusts the chisel into the ground. The resulting reaction forces between the ground and chisel slams the chisel back into the center body .The shock wave propagates through the center body to the handle. The vibration isolation treatment between the chisel and center body is another technique to reduce the vibration levels at the handles. This could become

very significant vibration control technique for any impact hammer. A softer spring between the chisel and center body reduced the high frequency levels in the range 3-5 db.

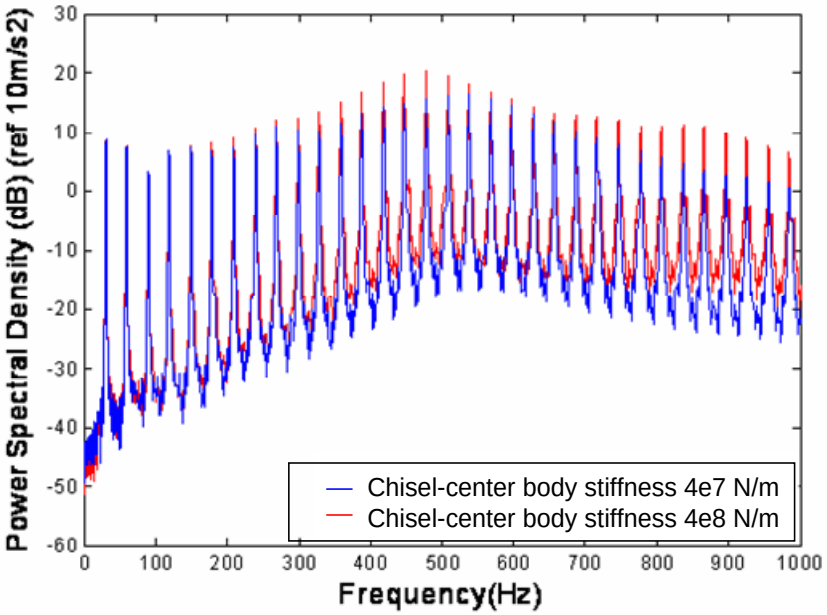

Figure 5- 10 : Effect of the increase in the chisel-center body stiffness on the tool handle's power spectral density

5.6.2. Advanced Vibration Isolator between the Center Body and Chisel

Figure 5- 11 shows the application of a visco-elastic vibration isolator between the chisel and center body. The advanced vibration isolator placed between the chisel and center body will reduce the energy transferred from the chisel to the center body. Figure 5- 12 illustrates the effect of the vibration absorber on the handle response. It can be seen that the absorber is very effective in the higher frequency range i.e. above 150 Hz. The vibration levels reduce in the range of 5-10 db above 150 Hz. However the peaks of the lower frequency response increase due to the isolator. The results also indicate that the passive methods of vibration

control aren't effective in the lower frequency range. Some random values of mass, stiffness and damping values chosen for the an vibration isolator example were as follows,

M=0.2 kg, K=4e2 N/m, C=5000 Ns/m

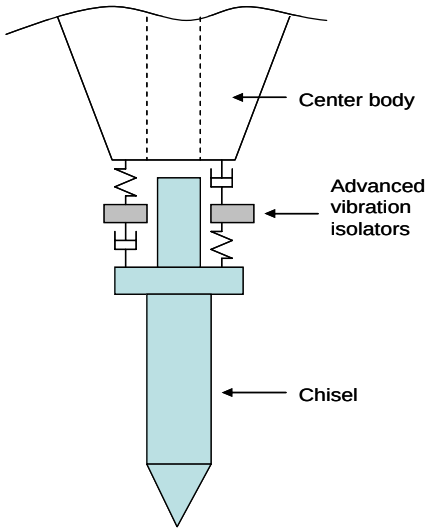

Figure 5- 11 : Advanced vibration isolator between the chisel and center body

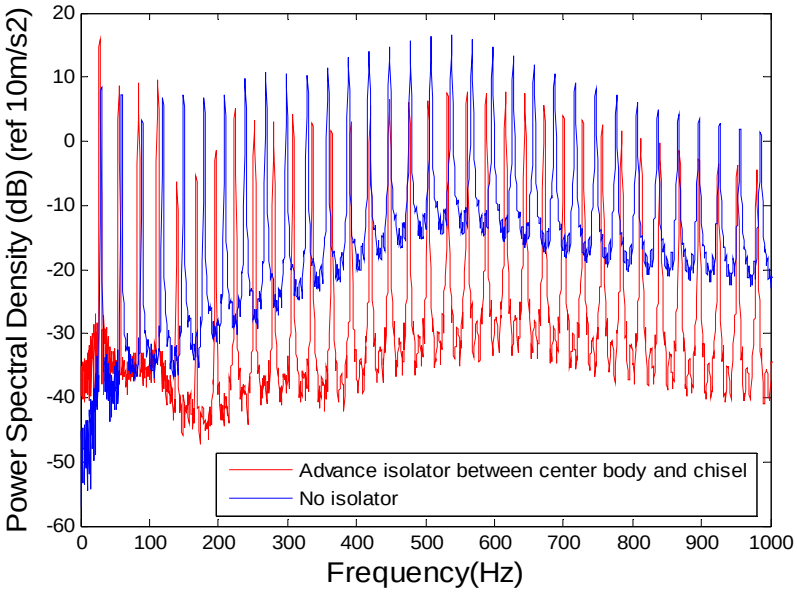

Figure 5- 12 : Effect of vibration absorber on the handle response

5.7. Changing the Ground Damping

Figure 5- 13 shows the effect of the increase in the ground damping by factor of 10 on the tool handle's power spectral density. The response of the handle changes significantly with

change in the ground damping. The power spectral density spectrum dropped significantly (about 3-20 db) with the increase in the ground damping across the frequency band. This implies that more energy gets dissipated in the more damp ground. This is an important result because in actual working environment, the ground keeps on changing very frequently.

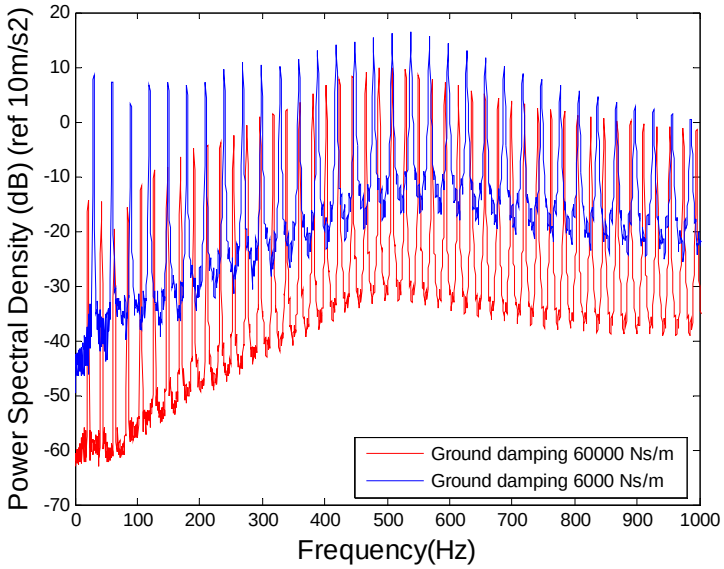

Figure 5- 13 : Effect of the increase in the ground damping on the tool handle's power spectral dnesity

Chapter 6. Conclusions and Future Work

This chapter deals with the conclusions drawn from the above work and the future work required to take the work further.

6.1. Conclusions

The analytical 4-DOF models had been proposed previously by different researchers to model the hand-arm system. They were highly damped models and actual hand arm data validates the damper like behavior. One problem is that the masses used in the model are extremely small and therefore it may not be possible to build such models practically. Therefore a beam like rig was developed.

Vibration levels of the impact hammer were measured using the experimentally simulated hand-arm rig and three human subjects. Comparison of the test data showed that the tool response for the simulated rig lies either in the range of or very close to range of the tool response for the human subjects. The consistency of the rig is quite comparable to the consistency of the human subjects for all the preload cases. Sometimes it is even better than the consistency of the human tests. Therefore, it can be said that building the actual 4-DOF model may not be necessary to replicate the response of the hand-arm system. However, a simple heavy beam with an appropriately high amount of damping can be used to get the dynamic characteristics of hand-arm system experimentally.

A novel numerical model of the pneumatic impact hammer was also developed using a non-linear state-space method. The model primarily consisted of two sub models, a dynamic model and a fluid flow model. The model captures the basic physics of the impact hammer

very well. It can predict the displacement, velocity and accelerations of all the major component of the impact hammer as well as the upper and chamber pressure levels.

There were three experiments conducted to validate the model. They are the pressure probe measurements in the upper and lower chambers, exhaust jet velocities and the handle accelerations. After comparing various experiments and numerical results it can be concluded that the numerical model gives reasonably accurate predictions of vibrations, exhaust jet velocity and pressure levels in the upper and lower chamber.

The noise emitted from the pneumatic impact hammer is a combined effect of the noise emitted from exhaust jet velocities and the structural impacts. The numerical model can be extended to predict the sound emitted from the pneumatic impact hammer. The numerical model can then be used to design & test noise control methods.

Here the hand–arm system is modeled as a single DOF model whereas in reality the hand is a nonlinear damped system consisting of a large number of nonlinear biological elements. Therefore the model needs to be extended to include realistic hand-arm dynamics as well as the “ground”.

Extensive parametric study was performed to explore various vibration control techniques. Use of D-shape handle resulted in elimination of the bending resonance at 500 Hz. That resonance was pushed far beyond the range of interest 0- 1000 Hz. The use of dampening materials between the chisel and center body helped reduce the vibration in the higher frequency region (>150 Hz).

This model puts forward a unique approach to model pneumatic hammer. It is a very general, flexible and easy to understand. The model has given very reasonable results for

exhaust jet velocities, accelerations and the pressure profiles, however there is still considerable future work required as explained in the next section.

6.2. Future Work

The future work required is as follows;

1) The impact modeling can be formulated in terms of wave propagation.
2) The hand and ground modeling also need to be improved in order to take into account the nonlinearities.
3) There is a need to accurately find the stiffness, damping of the major components of the pneumatic hammer.
4) In the model the opening and closing of the exhaust ports is instantaneous. The opening and closing of the exhaust ports can be made more gradual.
5) The accuracy of the mass flow rate equations need to be determined using experimental results.

Bibliography

1. M Fritz, “An improved biomechanical model for simulating the strain of the hand-arm system under vibration stress.” J Biomech. 1991; 24(12):1165-71
2. D.D. Reynolds, Falkenberg, “A study of hand vibration on impact and grinding operators-Part-II”, J. of Sound Vibration(1984) 95(4)
3. D.D. Reynolds, E.N. Angevine, “Vibration transmission characteristics of hand arm system”, J. of Sound Vibration(1977) 51
4. C W Suggs , “Modeling of dynamic characteristics of human hand arm system”, The Vibration Syndrome, Academic Press
5. C. F. Abrams, “A study of transmission of high frequency vibration in the human arm”. MS Thesis, North Carolina State University, 1977
6. D.D. Reynolds, W Sodel , “Dynamic response of the human hand arm system to a sinusoidal input”, J. of Sound Vibration(1967) 21
7. R. Gurram, S. Rakheja, PE Boileau, GJ Gouw, “Development of a grip force dependent hand-arm vibration model.” Cent Eur J Public Health. 1996 Feb; 4(1):65-8.
8. G Jancik, M D Bochum , “Blood supply disturbances caused by vibrations”, International hand-arm conference 1975, Cincinnati, USA
9. A J Zweifler , “Detection of occlusive arterial disease in the hand and its relevance to occupational hand disease” International hand-arm conference 1975, Cincinnati, USA

10. D Koradecka, “Peripheral blood circulation under the influence of occupational exposure to hand-transmitted vibration” International hand-arm conference 1975 Cincinnati, USA
11. R M Nerem, “Vibration enhancement of blood–arterial wall macromolecular transport”, International hand-arm conference 1975, Cincinnati, USA
12. A. M. Ehary, “Treatment of sever secondary Ranyaud’s disease” International hand-arm conference 1975, Cincinnati, USA
13. L. Loud , E Lukas, “Hygienic aspect of occupational hand-arm vibration” International hand-arm conference 1975, Cincinnati, USA
14. R. G. Dong, T. W. McDowell, D. E. Welcome., C. Warren and A. Schopper W. “An evaluation of the standardized impact hammer test specified in ISO 8662-2”. The Annal of Occupational Hygiene, Vol. 48, No. 1, pp. 39-49, 2004
15. M.J.Griffin, “ Handbook of Human Vibration” , Academic Press; New Ed edition (November 19, 1996)
16. R Dong, S Rakheja, A. W. Schopper, B. Han and Smutz, W. P. 2001. “Hand-transmitted Vibration and biodynamic response of the human hand-arm: A critical review”, Critical Reviews in Biomedical Engineering, 29, 393-439.
17. W Taylor, J C G Pearson, G D Keighley, “A longitudinal Study of Raynaud’s Phenomenon in Chain saw Operators”, International hand-arm conference 1975
18. Lindstorm I.M , “Vibration Injury in Rock drillers, Chiselers and Grinders”, International hand-arm conference 1975, Cincinnati, USA

19. Rafalski H, Bernacki K , Switoniak T., “The diagnostics and epidemiology of vibration disease and hearing impairment in Motor Sawyers”, International hand-arm conference 1975, Cincinnati, USA
20. Leonida D , “Ecological Elements of Vibration Syndrome” International hand-arm conference 1975, Cincinnati, USA
21. Reynolds D D, “Hand-arm vibration :A review of three years of research”, International hand-arm conference 1975, Cincinnati, USA
22. Hempstock T.I., O’Connor D E, “Evaluation of human exposure to hand transmitted vibration”, International hand-arm conference 1975, Cincinnati, USA
23. Suggs C W, Mishoe J W ,” Hand –arm vibration: implications drawn from lumped parameter models”, International hand-arm conference 1975, Cincinnati, USA
24. Wood L.A. , Suggs C W , “A distributed parameter dynamic model of the human response”, International hand-arm conference 1975, Cincinnati, USA
25. Frood A D M, “Test Methods and some of the problems involved in measuring the vibration of hand-held pneumatic tools”, International hand-arm conference 1975
26. Kitchner R , “Measurement of hand arm vibration in industry”, International hand-arm conference 1975, Cincinnati, USA
27. Abrams C F, “A study of transmission of high frequency vibration in the human arm”, M. S, Thesis, North Carolina State University, 1977
28. ISO 8662-2 (1992), “Hand held portable power tools –Measurement of the vibrations at the handle-Part 2”
29. ISO 5349 : “Mechanical vibration-measurement and evaluation of human exposure to hand-transmitted vibration"

30. ISO 8727:1997, “Mechanical vibration and shock -- Human exposure -- Biodynamic coordinate systems”

31. ISO 8041:2005, “Human response to vibration -- Measuring instrumentation”

32. S. S. Pang, W. Goldsmith, “A model of a pneumatic jackhammer system”, Rock Mechanics and Rock Engineering, Volume 25, Issue 1, Jan 1992, Pages 49 – 61

33. E. V. Golycheva, V. I. Babitsky and A. M. Veprik, “Dynamic Correction of in Handheld Electro-Pneumatic Percussion Machines”, Journal of Sound and Vibration (2003) 259(4), 829–843

34. Y T Wang, R Singh, H C Yu, D A Guenther, “Computer Simulation of a Shock-Absorbing Pneumatic Cylinder”, Journal of Sound and Vibration (1984) 93(3), 353-364

35. **“**Perry's Chemical Engineers”, Handbook, Sixth Edition, McGraw-Hill Co., 1984

36. Miwa, T. et al. 1979. “Vibration isolators for portable vibrating tools, Part 1”. A grinder. Ind. Health 17: 85-101.

37. Strydom, J.P.D., Heyns,P.S. & Van Niekerk,J.L. “Development of a vibration absorbing handle for rock drills”, Journal of the Institute of Mining and Metallurgy, vol.102, no.3, April 2002, pp.167-172.

38. Oddo R, Loyau T, Boileau PE, Champoux Y (2004), “Design of a suspended handle to attenuate rock drill hand-arm vibration: model development and validation”, J Sound Vib **275**, 623–40.

39. K. Prajapati and P. Hes, “Reduction of hand-arm transmitted vibration on pneumatic jackleg rock drills” , The Canadian Mining and Metallurgical Bulletin, Volume 94,Num. 1047,February. 2001

40. Attala N, “Analyses des performances acoustiques et vibrations du fleuret a foreuse TWITEX”, November 1998 ,A-204,IRRST

41. Kyle Schwartz, “Acoustic charecterization and noise control of pneumatic impact hammer”, July 2006,MS thesis

42. Atlas Copco TEX 317 Specifications

Appendix 1: Dimensions of Chisel

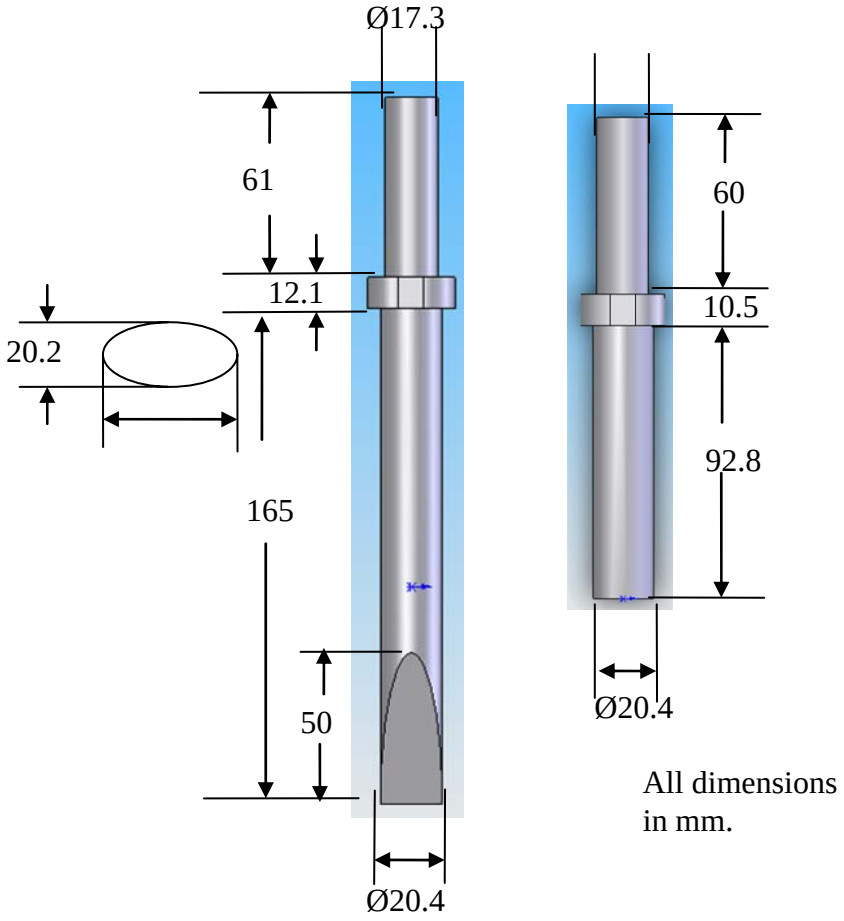

Figure A- 1. Dimensions of the long and short chisel used in conjunction with the Atlas Copco impact hammer.

Appendix 2: Mode Shapes of the Retainer and Chisel

This appendix explains the first two mode shapes of the retainer and the chisel as discussed in section 2.3.1

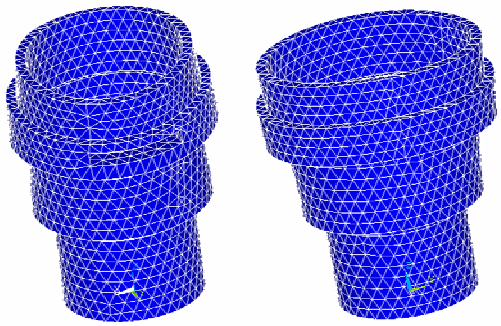

Figure A- 2 : Mode shape of the retainer at frequency 6072.8 Hz

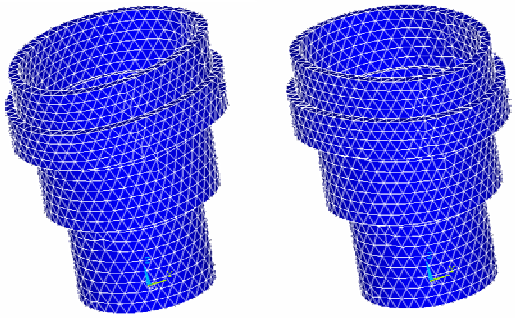

Figure A- 3 : Mode shape of the retainer at frequency 6151.8 Hz

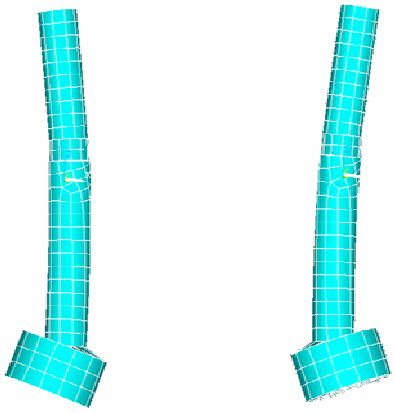

Figure A- 4 : Mode shape of the chisel at frequency 3210 Hz

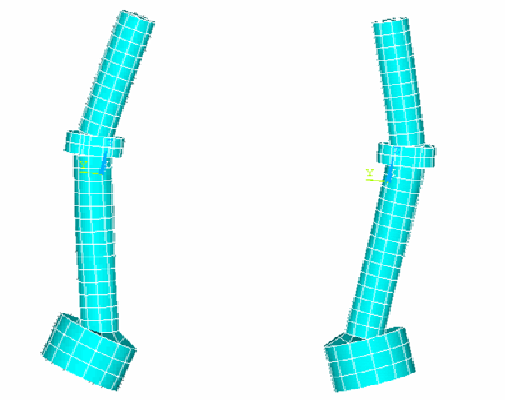

Figure A- 5 : Mode shape of the chisel at frequency at 3459 Hz

Appendix 3: Results obtained from the Vibration Tests

This appendix includes the results obtained from the vibration tests using the experimental rig as well as the human subjects

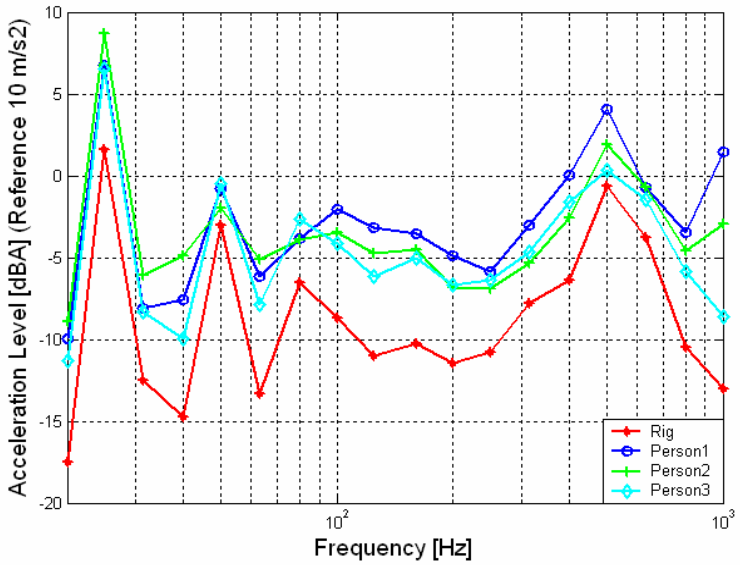

Figure A- 6 : 1/3 Octave band Acceleration Auto-spectrum (Two Test Averages) of Tool-Handle (dBA) at 50N

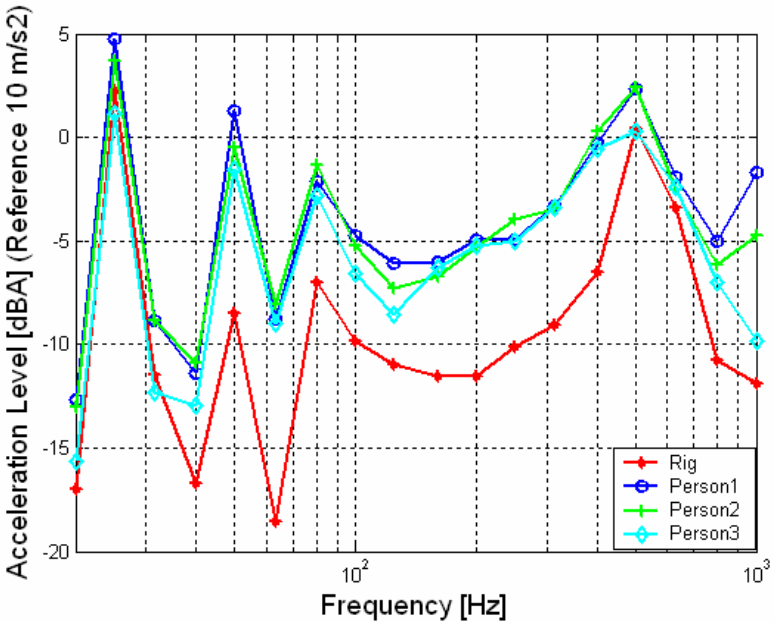

Figure A- 7 : 1/3 Octave Acceleration Auto-Spectrum (Two Test Averages) of Tool-Handle (dBA) at 100N

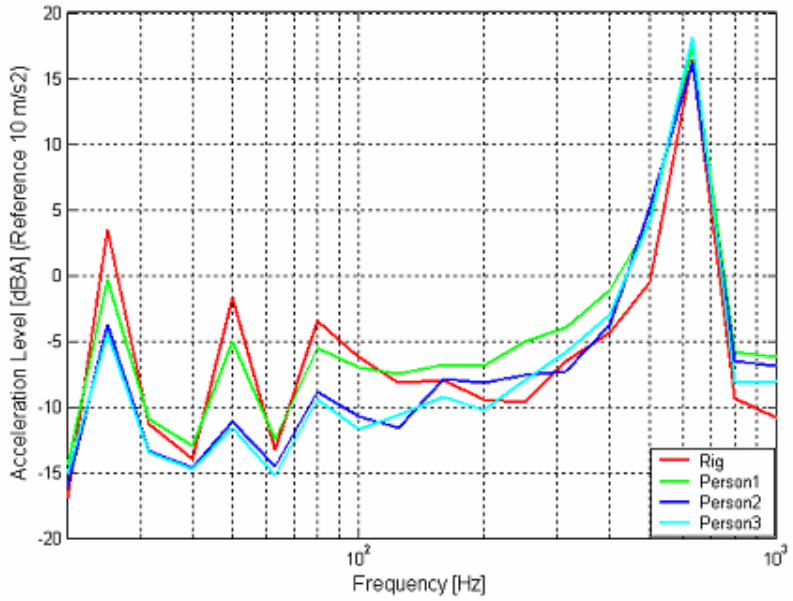

Figure A- 8 : 1/3 Octave Acceleration Auto-Spectrum (Two Test Averages) of Tool-Handle (dBA) at 200N

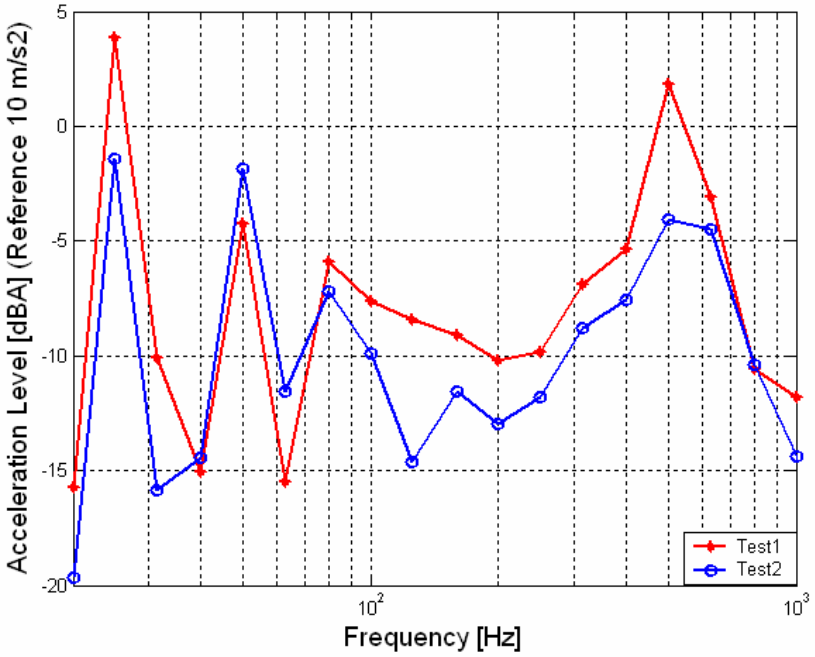

Figure A- 9 : Repeatability of 1/3 Octave Band Acceleration Auto-spectrum (dBA) at 50N for the Rig

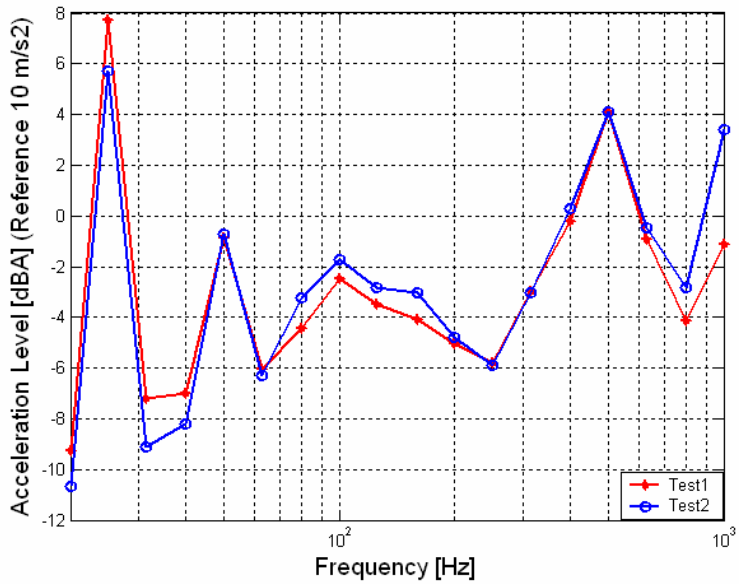

Figure A- 10 : Repeatability of 1/3 Octave Band Acceleration Auto-spectrum (dBA) at 50N for the Person1

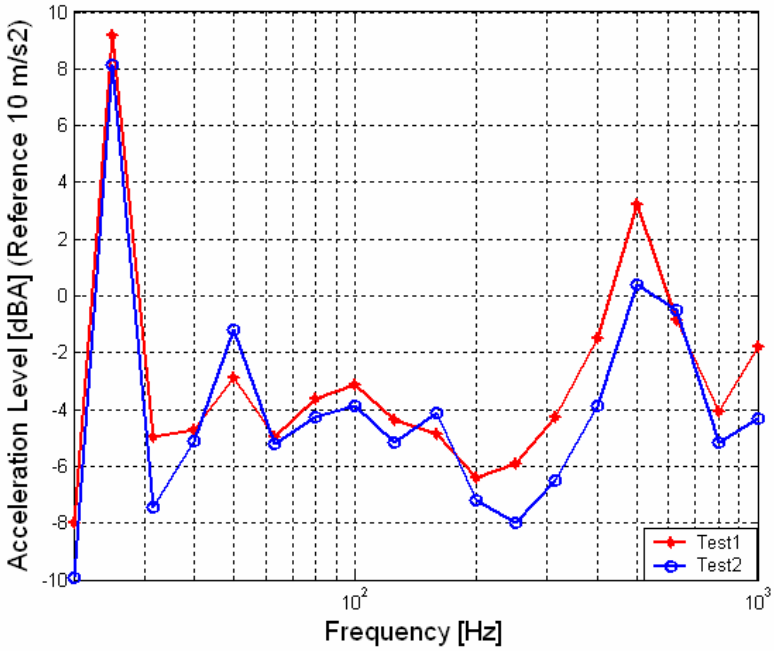

Figure A- 11 : Repeatability of 1/3 Octave Band Acceleration Auto-spectrum (dBA) at 50N for the Person2

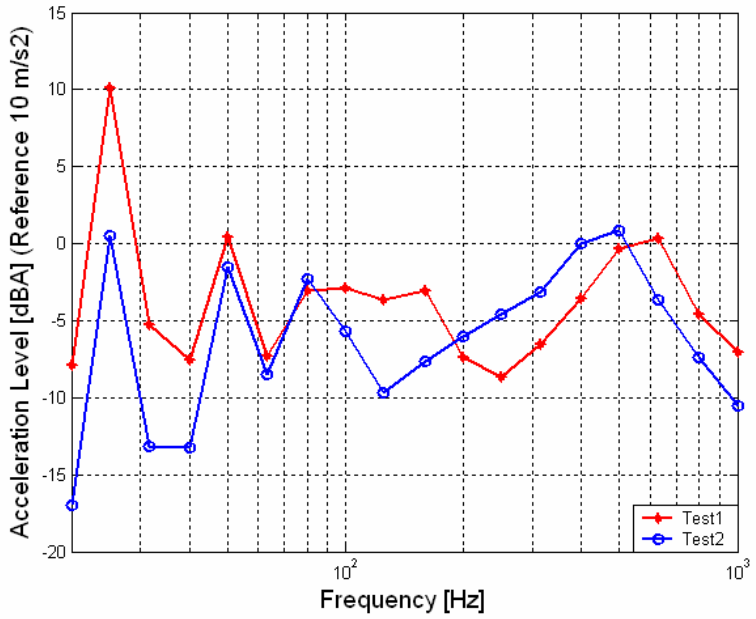

Figure A- 12 : Repeatability of 1/3 Octave Band Acceleration Auto-spectrum (dBA) at 50N for the Person3

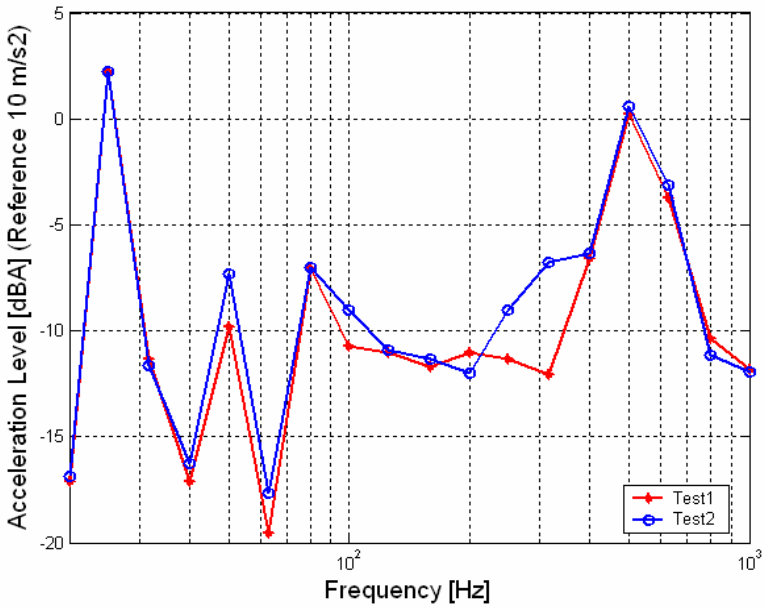

Figure A- 13 : Repeatability of 1/3 Octave Band Acceleration Auto-spectrum (dBA) at 100N for the Rig

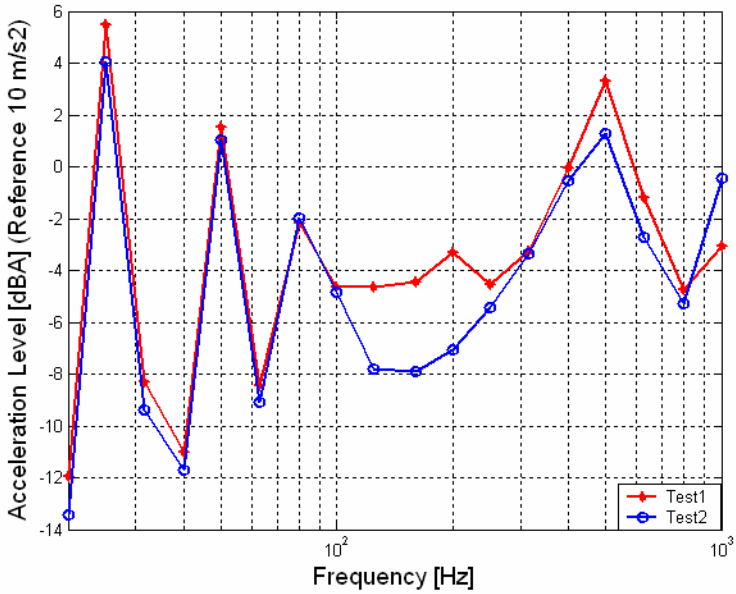

Figure A- 14 : Repeatability of 1/3 Octave Band Acceleration Auto-spectrum (dBA) at 100N for the Person1

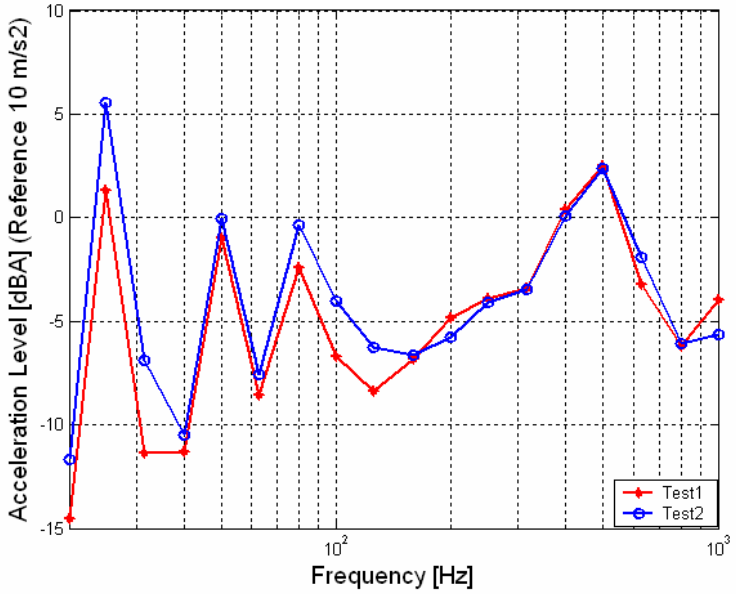

Figure A- 15 : Repeatability of 1/3 Octave Band Acceleration Auto-spectrum (dBA) at 100N for Person2

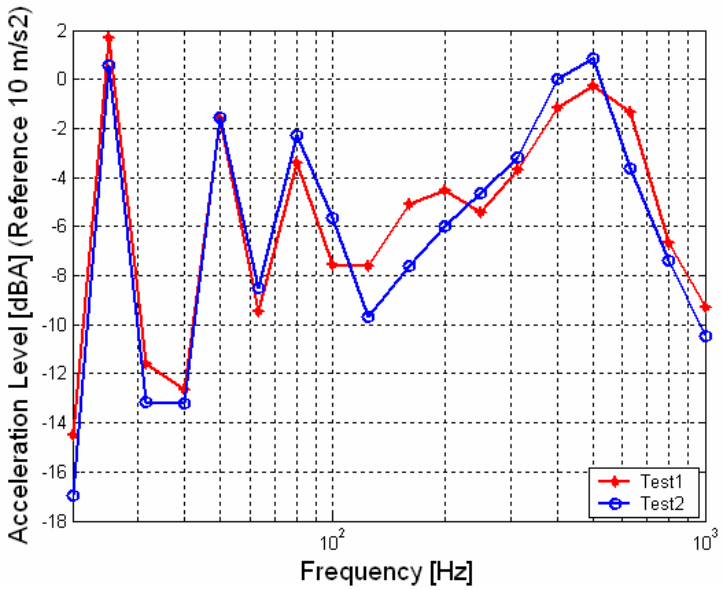

Figure A- 16 : Repeatability of 1/3 Octave Band Acceleration Auto-spectrum (dBA) at 100N for the Person3

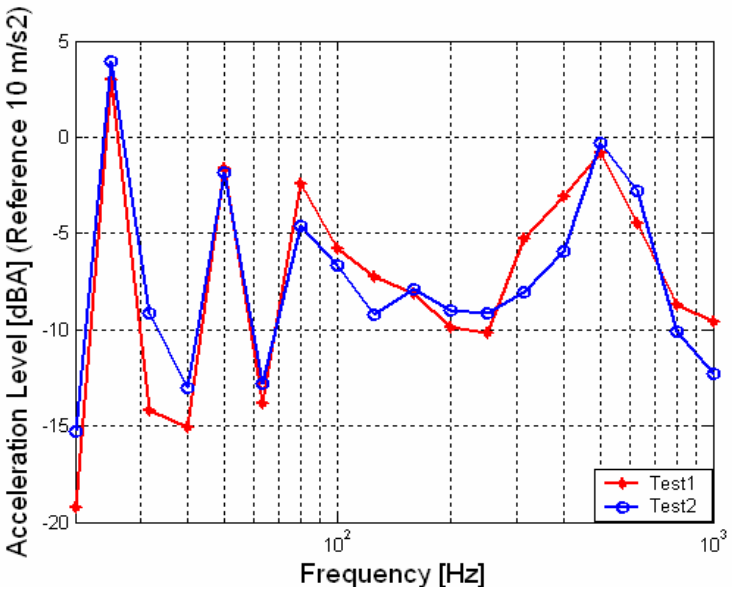

Figure A- 17 : Repeatability of 1/3 Octave Band Acceleration Auto-spectrum (dBA) at 200N for the Rig

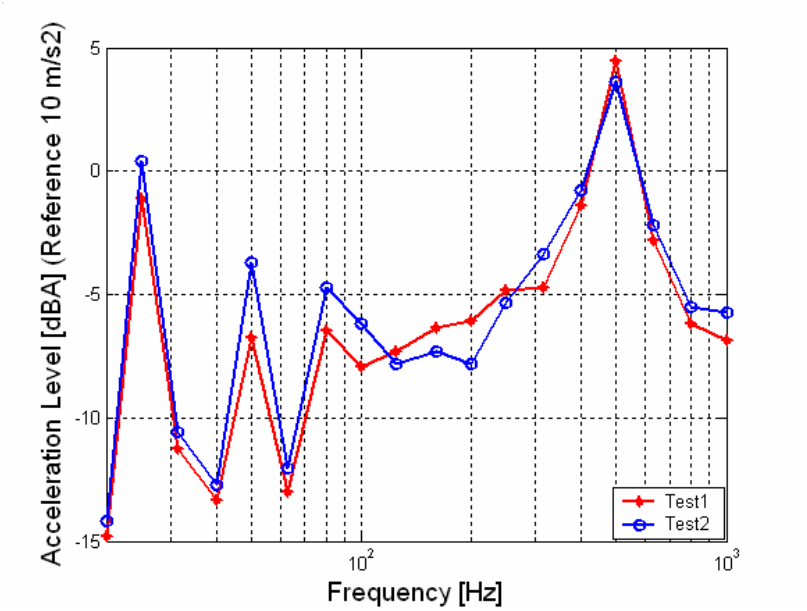

Figure A- 18 : Repeatability of 1/3 Octave Band Acceleration Auto-spectrum (dBA) at 200N for the Person1

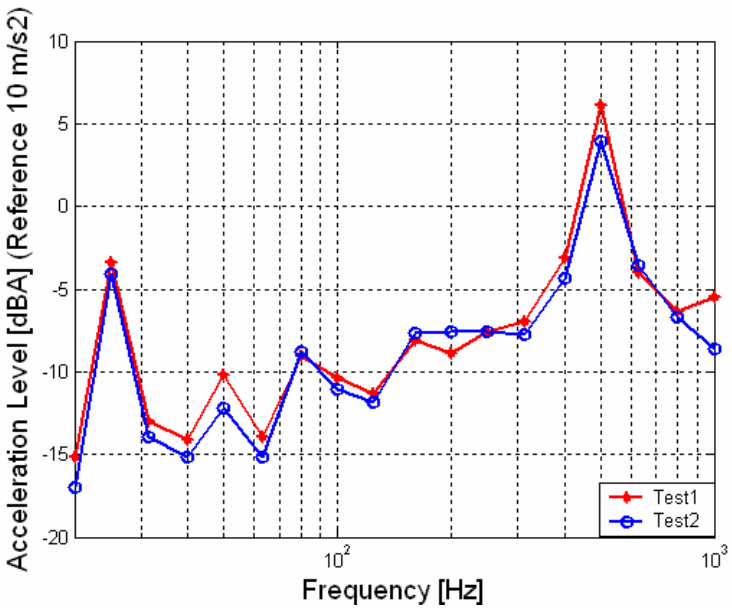

Figure A- 19 : Repeatability of 1/3 Octave Band Acceleration Auto-spectrum (dBA) at 200N for the Person2

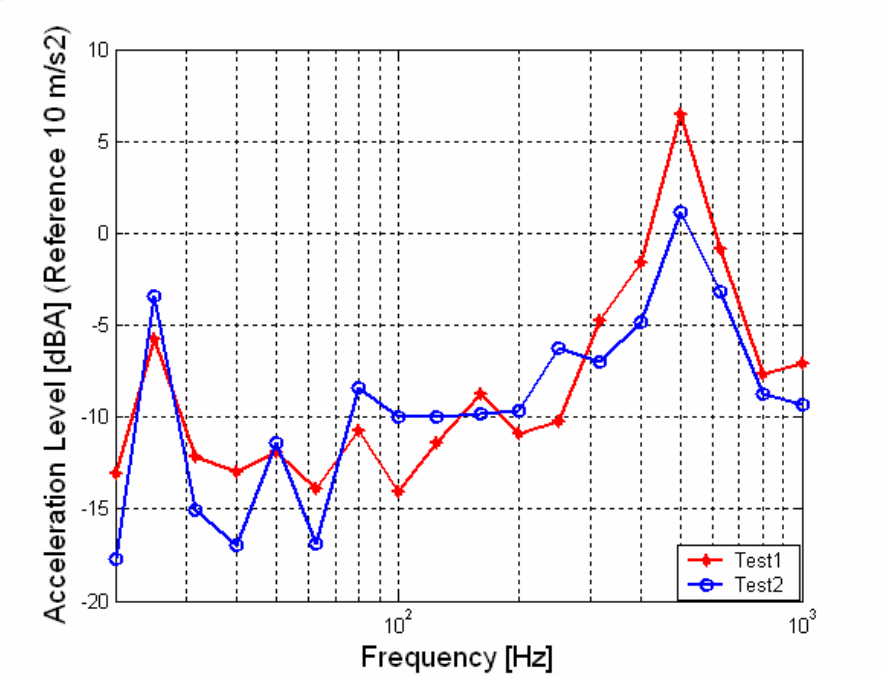

Figure A- 20 : Repeatability of 1/3 Octave Band Acceleration Auto-spectrum (dBA) at 200N for the Person3

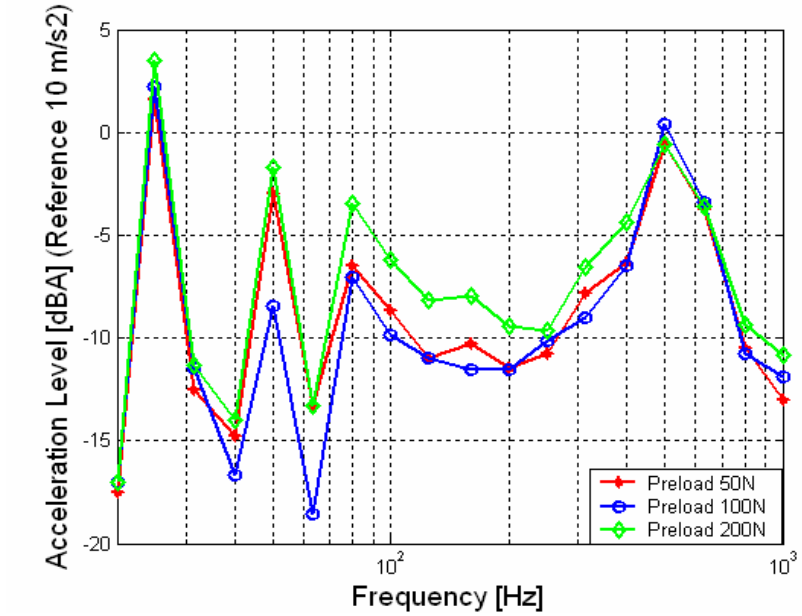

Figure A- 21 : Variation of 1/3 Octave Band Acceleration Auto-spectrum (dBA) with different preloads for the Rig

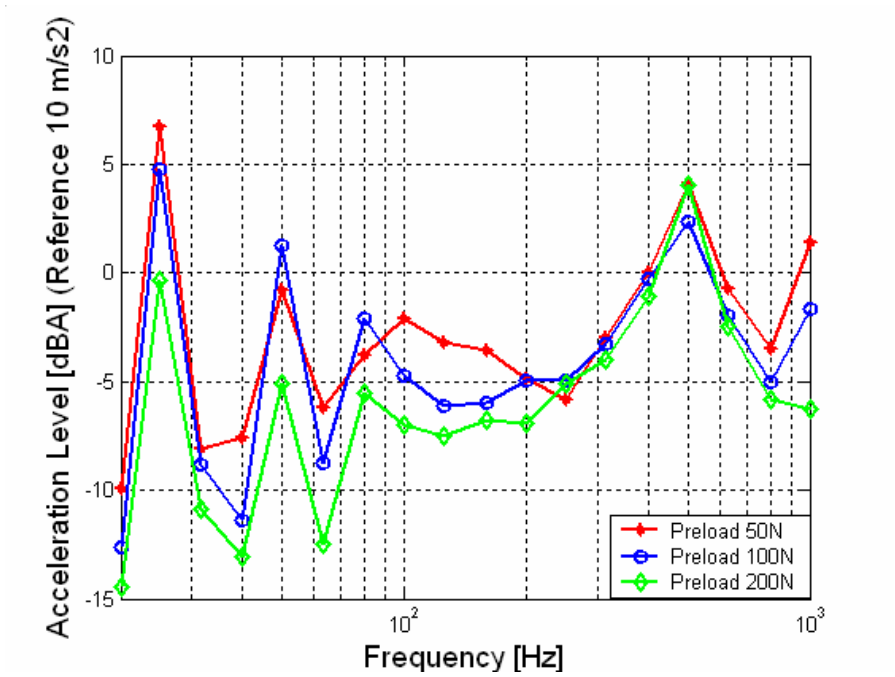

Figure A- 22 : Variation of 1/3 Octave Band Acceleration Auto-spectrum (dBA) with different preloads for the Person1

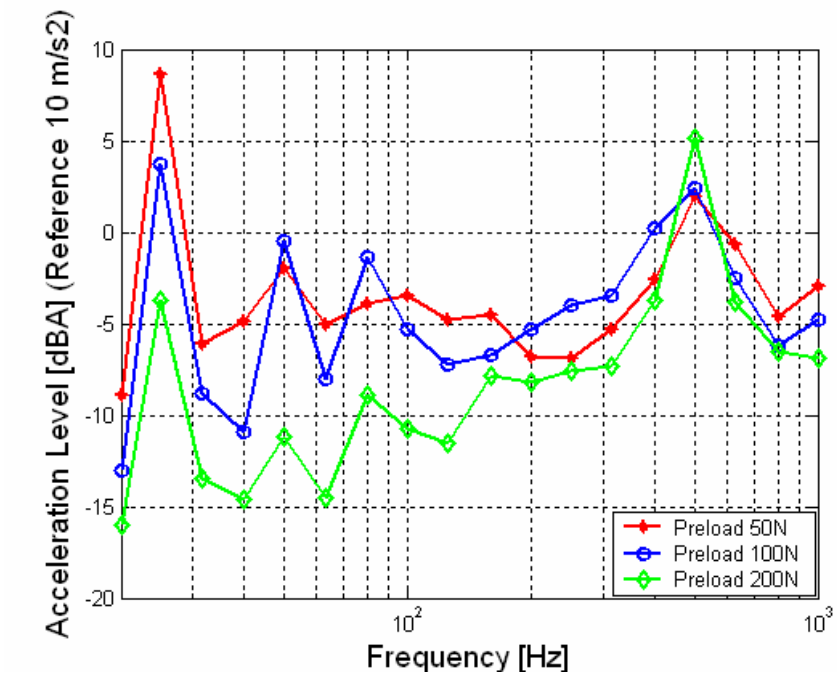

Figure A- 23 : Variation of 1/3 Octave Band Acceleration Auto-spectrum (dBA) with different preloads for the Person2

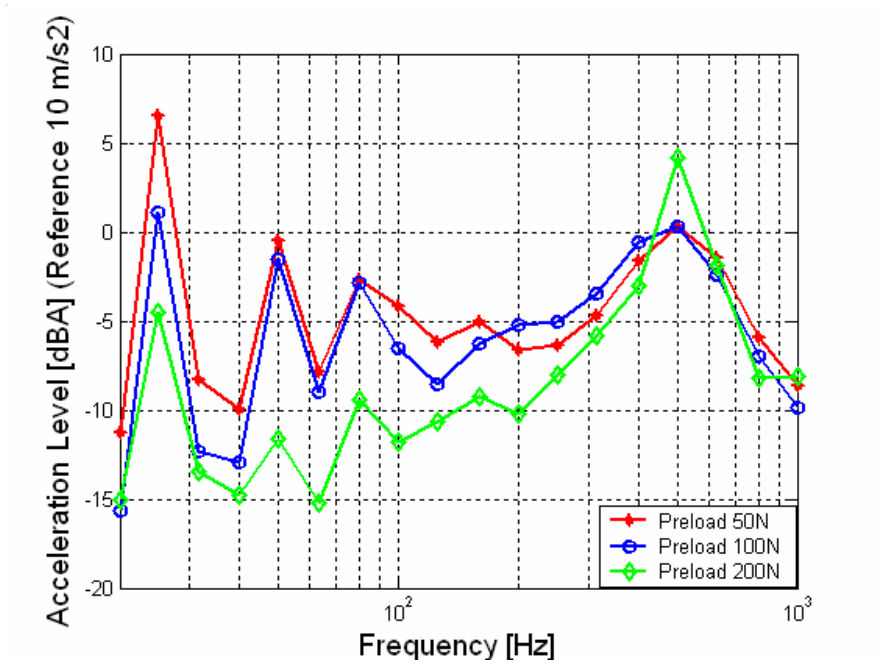

Figure A- 24 : Variation of 1/3 Octave Band Acceleration Auto-spectrum (dBA) with different preloads for the Person3

Appendix 4: ISO Standards and Co-ordinate system for Hand-Arm Vibrations:

International Standards' Organization has laid down standards for hand-arm vibration measurements namely ISO 5349 and ISO 8662-2. In this section a brief account of these standards has been given.

i. ISO 8662 [28]

These standards define the laboratory method for measuring the vibrations at the handles hand-held power driven impact hammers and riveting hammers. It is a type test procedure for establishing the magnitude of vibration in the handle of a power tool operating under specified load. The standards specify the dimension for the design of energy dissipater and the modified chisel for the impact hammer as can be seen from Table A- 1. The energy dissipater and the chisel have been built according to the specifications. The chisel has a broad end instead of a conventional taper end. The chisel was manufactured as can be seen in Figure A- 25.

Figure A- 25 : Modified chisel (ISO 8662-2)

Table A- 1: Design criteria for the energy absorber

Shank diameter d (mm)	Steel tube diameter D (mm)	Steel ball diameter (mm)	Ball column height H (mm)
d>=13	40	4	100

ii. Coordinate System for Hand-Arm Vibration Measurement

Figure A- 26 represents the biodynamic and basic-centric coordinate system for hand-arm system as per defined by ISO 8727 [30]. The basic-centric co-ordinate system centered on the vibrating surface is generally used to take the vibration measurements. The x-axis is generally taken parallel to biodynamic x-axis. The y-axis is along the central axis of the handle and the z-axis is perpendicular to both axes. The idea behind this measurement procedure is to measure at the point where vibration actually enters the human body. This approach is also useful to insure the repeatability of the results.

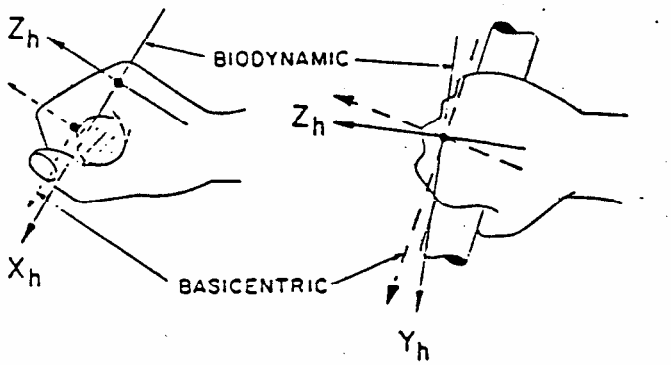

Figure A- 26 : Hand-arm vibration measurement co-ordinate system

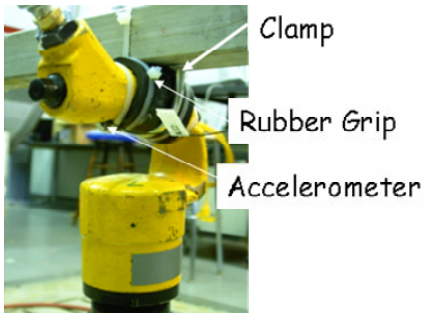

Figure A- 27 : Position of accelerometer

Appendix 5: Matlab Code for Impact Hammer Model

Main code

```
% This code is simulation of the pneumatic impact hammer. The hammer is
% driven by pneumatic pressure .Code simulates the general physics of the
% tool i.e. displacements, velocity and acceleration and exhaust jet
% profiles. The model can be extended to predict the noise radiated from
% the tool.


 clc
 clear all
 format short

 % Structural parameters

 global m_hd  m_hdl m_cb m_pst m_ch;
 %mass terms
 m_hd=2;%mass of hand
 m_hdl=1.5;%mass of handle
 m_cb=2.180;%Center body
 m_pst=0.362;%Piston
 m_ch= 5.515;%Chisel

 global k_hd k_hd_hdl k_hdl_cb k_cb_ch k_ch_gd;
 %stiffness terms
 k_hd=3.9478e5;
 k_hd_hdl=6e3;
 k_hdl_cb=1.5e7;
 %  k_cb_ch=3.7244e8;
 k_ch_gd=3e5;

global c_hd c_hd_hdl c_hdl_cb c_cb_ch c_ch_gd c_friction;
%damping terms
 c_hd=30;
 c_hd_hdl=40;
 c_hdl_cb=k_hdl_cb*0.0001;
 % c_cb_ch=1000;
 c_ch_gd=6000;
 c_friction=0.00001;

 % geometrical parameters of the impact hammer
 global A_l1 A_uc A_lc A_up A_lp A_l2 A_bore ;%area2
 nports_up=6; % no of upper ports
 nports_lp=6; % no of lower ports
 A_l1=(pi/4)*((28.4e-3)^2-(28.39e-3)^2);%area of leakage between piston
                                        and center body
 A_uc=2*(pi/4)*((6e-3)^2);% area of orifice between supply pressure and
                          upper chamber
 A_lc=2*(pi/4)*((6e-3)^2);% area of orifice between supply pressure and
                          lower chamber
```

```
A_up=nports_up*(pi/4)*((6e-3)^2);% area of upper exhaust port
A_lp=nports_lp*(pi/4)*((6e-3)^2);% area of lower exhaust port
A_l2=(pi/4)*((17.4e-3)^2-(17.3e-3)^2);%area of orifice between lower
                                      chamber and atmosphere
A_bore=(pi/4)*((28.4e-3)^2);% Area of the bore inside center body
Vc_lc=1000e-8;% volume of the lower chamber when the piston impacts
               chisel

% gas parameters
global r R g T C;
r=1.41;%specific heat ratio
R=8.3144e3/29;%gas Constant
g=1;%gravitational Constant
T=293;%temperature
C=0.7;%discharge coefficient

%initial conditions for the all the structural masses and air masses in
%the upper and lower chamber
x0=[0; 0; 0;0.0001;0;0;0; 0;0;0;8.3391e-005;8.3391e-006;0;0];
% time step for the simulation
ts=[0:0.00005:4];
% the ode45 function
[t,x]=ode45('param5_t8_rahul3_refine2',ts,x0);
%  time span
tds=t(2)-t(1);
%  no of ports for upper exhaust
nports_up=6;
% no fo ports for lower exhaust
nports_lp=6;
% Acceleration of piston
Acc_pst=diff(x(:,9))/tds;
% Volume of upper chamber
Vuc=(A_bore*(0.102-x(:,4)+x(:,3)));
% Volume of lower chamber
Vlc=(A_bore*(x(:,4)-x(:,5))+Vc_lc);
% Pressure in upper chamber
P_uc=(x(:,11)*R*T)./(Vuc*6894.76);
% Pressure in lower chamber
P_lc=(x(:,12)*R*T)./(Vlc*6894.76);
% Density of air in upper chamber
den_uc=1.2;
% Density of air in lower chamber
den_lc=1.2;
% Area of exhaust port*density of air
Aden_uc=(den_uc*(pi/4)*((6e-3)^2));
% Area of the exhaust port * density of air
Aden_lc=(den_lc*(pi/4)*(6e-3)^2);
% velocity of exhaust through upper ports
Vexh_up=(diff(x(:,13)))/(nports_up*tds*Aden_uc);
% velocity of exhaust through lower ports
Vexh_lp=(diff(x(:,14)))/(nports_lp*tds*Aden_lc);
% mass flow rates through upper ports
mdot_exhaust_up=diff(x(:,13))/tds;
% mass flow rates through lower ports
mdot_exhaust_lp=diff(x(:,14))/tds;
% Exhaust jet velocity from upper port
```

```
Vexh_up=(mdot_exhaust_up)/(nports_up*Aden_uc);
% Exhaust jet velocity from upper port
Vexh_lp=(mdot_exhaust_lp)/(nports_lp*Aden_lc);
% acceleration of the handle
Acc_hdl=(diff(x(:,7))/tds);

% calculating the power spectral density of the handle accelerations
[psd_hdl,freq] = PWELCH(([Acc_hdl(5000:end)']'),[],[],[40000],1/tds);

% calculating the band averaged spectrum of the power spectrum
Gbb=psd_hdl;
l1=[1:100]*0;
l2=[1:100]*0;
l1(1)=32;
l2(1)=96;
for k=2:100
  l1(k)=l2(k-1);
  l2(k)=l1(k)+64;
end
for k=1:100
  [a(k) b(k)]=max(Gbb(l1(k):l2(k)))
end
b=[64:64:2500];
a=[0,a];
b=[0,b];
freq_band=b./2;

   figure(1)
   % plotting the displacement of all the mass components
   plot(t,x(:,1)+0.101,t,x(:,2)+0.101,t,x(:,3)+0.101,t,x(:,4),t,x(:,5));
   ylabel('Displacement(m)','fontsize',14)
   legend('Hand','Handle','Center
   Body','Piston','Chisel',5,'fontsize',14)
   title('Displacement of Piston (m)','fontsize',14)

   figure(2)
   % plotting the exhaust jet velocities from the upper and lower ports
   plot(t(2:end),Vexh_up,'r',t(2:end),Vexh_lp,'b')
   xlabel('Time(s)','fontsize',14)
   ylabel('Velocity(m/s)','fontsize',14)
   legend('Exhaust jet velocity from upper ports','Exhaust jet velocity
   from lower ports',2)
   title('Velocity of Jet through Exhaust Ports vs Time','fontsize',14)

   figure(3)
   % plotting velocity of piston
   plot(t,x(:,9),'b')
   legend('Piston Velocity')
   xlabel('Time(s)','fontsize',14)
   ylabel('Velocity of Piston(m/s)','fontsize',14)

   figure(4)
   % plotting acceleration of handle
   plot(t(2:end),diff(x(:,7)),'b')
   legend('Handle Acceleration')
   xlabel('Time(s)','fontsize',14)
```

```
ylabel('Acceleration of handle (m/s)','fontsize',14)

figure(5)
% Plotting presure profiles in the upper and lower chamber
plot(t(1:end-50),P_uc(51:end),'r',t(1:end-50),P_lc(51:end),'b');
xlabel('Time(s)','fontsize',14)
ylabel('Pressure(psi)','fontsize',14)
title('Pressure in Upper and Lower Chmaber vs Time','fontsize',14)
legend('Upper Chamber Pressure','Lower Chamber
Pressure','Acceleration(Scaled)','fontsize',14)
xlim([0 0.12]);ylim([0 100]);

figure(6)
% plotting the power spectral density of the tool handle
plot(freq,10*log10(psd_hdl/10))
xlabel('Frequency(Hz)','fontsize',14);
ylabel('Power Spectral Density (dB) (ref 10m/s2)','fontsize',14);
legend('Impact Hammer Handle')
xlim([0,1000])

figure(7)
% plotting band averaged power spectrum
plot(freq_band(1:39),10*log10(a(1:39))/10)
xlabel('Band averaged power spectrum (m/s2)^2','fontsize',14)
ylabel('Frequency (Hz)','fontsize',14)
xlim([0 1000])
```

Function param5_t8_rahul3_refine2

```
% This function nonlinear state-space model which calculates structural
% response .It accepts the initial condition vector and the time vector.
% for each time step it calculates the state vector v which then will be
% integrated to get the displacement, velocity and acceleration

function [v]=param5_t8_rahul3_refine2(t,x);

%global variables used in the main code

 global m_hd m_hdl m_cb m_pst m_ch;
 global k_hd k_hd_hdl k_hdl_cb k_cb_ch k_ch_gd;
 global c_hd c_hd_hdl c_hdl_cb c_cb_ch c_ch_gd c_friction;
 global A_l1 A_uc A_lc A_up A_lp A_l2 A_bore Vc_lc;
 global r R g T C;

 %Volume in the chambers
 V_uc=A_bore*(0.103-x(4)+x(2));%Upper chamber
 V_lc=(A_bore*(x(4)-x(5)))+1000e-8;%Lower chamber

 %calculating pressures
 %Ps_uc is the pressure supplied to the upper chamber
 %Ps_lc is the pressure supplied to the lower chambe
 %P_uc is the pressure in the upper chamber
 %P_lc is the pressure in the lower chamber
```

```
 %Patm is Atmospheric pressure

 Patm=14.7*6894.76;%Atmospheric pressure
 Ps_uc=(85.4*6894.76);%supply pressure in upper chamber
 Ps_lc=(85.4*6894.76);%supply pressure in lower chamber
 P_uc=x(11)*R*T/(V_uc);%pressure in upper chamber
 P_lc=x(12)*R*T/(V_lc);%pressure in lower chamber


%modeling impact between chisel and center body

  if sign(x(9))==1 & (x(4)-x(5))<0e-3
      k_cb_ch=0;
     else
      k_cb_ch=4e8;
 end

%modeling damping between chisel and center body
 if sign(x(9))==1 & (x(4)-x(5))<0e-3
      c_cb_ch=0;
     else
      c_cb_ch=1000;
 end

 %force calculations
 fpst=A_bore*(P_uc-P_lc);%force on piston

 f=[100;0;-fpst;fpst;0];%force between center body and piston. Assumed no
interaction with chisel

 %Mass matrix
 Mass=      [m_hd      0        0       0      0     ;
               0      m_hdl      0       0      0     ;
               0       0        m_cb     0      0     ;
               0       0         0     m_pst    0     ;
               0       0         0       0    m_ch   ] ;

 %used to model impact stiffness in three stages
 %Impact stiffness between piston and chisel

 if x(4)-x(5)<=0
     kimp_low=4e8;
     kimp_high=0;
% impact between piston and main body
 elseif x(4)-x(3)>=102e-3
     kimp_low=0;
     kimp_high=4e8;
 else
     kimp_low=0;
     kimp_high=0;
 end
 % Impact damping between piston and chisel
 if x(4)-x(5)<=0
     cimp_low=6000;
     cimp_high=0;
```

```
% impact between piston and main body
 elseif x(4)-x(3)>=102e-3
     cimp_low=0;
     cimp_high=6000;
 else
     cimp_low=0;
     cimp_high=0;
 end

%Stiffness matrix
Stiff=[k_hd+k_hd_hdl      -k_hd_hdl            0         0             0;
       -k_hd_hdl     k_hd_hdl+k_hdl_cb    -k_hdl_cb      0             0;
      0    -k_hdl_cb     k_hdl_cb+k_cb_ch+kimp_high  -kimp_high  k_cb_ch;
      0       0            -kimp_high     kimp_high+kimp_low  -kimp_low  ;
      0       0     -k_cb_ch      -kimp_low    k_cb_ch+k_ch_gd+kimp_low] ;

%Damping matrix
Damping=[c_hd+c_hd_hdl   -c_hd_hdl        0          0               0;
    -c_hd_hdl      c_hd_hdl+c_hdl_cb   -c_hdl_cb     0               0;
0   -c_hdl_cb c_hdl_cb+c_cb_ch+cimp_high  -c_frictio cimp_high  -c_cb_ch ;
0    0  -c_friction-cimp_high   c_friction+cimp_high+cimp_low   -cimp_low;
0    0       -c_cb_ch              -cimp_low   c_cb_ch+c_ch_gd+cimp_low] ;

%mass flow rate calculations
%mdot_supply_uc is the mass flow rate supplied to the upper chamber from
%source
%mdot_supply_lc is the mass flow rate supplied to the lower chamber from
%source
%mdot_exhaust_up1 is the mass flow rate through upper exhaust port when it
is interacting with
%lower chamber
%mdot_exhaust_up2 is the mass flow rate through upper exhaust port when it
is interacting with
%upper chamber
%mdot_exhaust_lp is the mass flow rate through lower exhaust port when it
is interacting with
%lower chamber
%mdot_leakage1 is the mass flow rate between upper and lower chamber
%because of pressure difference
%mdot_leakage2 is the mass flow rate between lower chamber and atmosphere
%because of pressure difference
  %%%%%%%%%%case A When both ports are interacting with the lower chamber

    if x(4)>=0.095
          mdot_leakage_pst=flowThroughOrifice(P_uc,P_lc,A_l1);
          mdot_supply_uc=flowThroughOrifice(Ps_uc,P_uc,A_uc);
          mdot_supply_lc=0;
          mdot_exhaust_up2=0;
          mdot_exhaust_up1=flowThroughOrifice(P_lc,Patm,A_up);
          mdot_exhaust_lp=flowThroughOrifice(P_lc,Patm,A_lp);
          mdot_leakage_ch=flowThroughOrifice(P_lc,Patm,A_l2);

%case B when only lower exhaust is interacting with lower chamber and
%upper exhaust is blocked by the piston
    elseif  x(4)<0.095 & x(4)>=0.04
```

```
          mdot_leakage_pst=flowThroughOrifice(P_uc,P_lc,A_l1);
          mdot_supply_uc=flowThroughOrifice(Ps_uc,P_uc,A_uc);
          mdot_supply_lc=0;
          mdot_exhaust_up2=0;
          mdot_exhaust_up1=0;
          mdot_exhaust_lp=flowThroughOrifice(P_lc,Patm,A_lp);
          mdot_leakage_ch=flowThroughOrifice(P_lc,Patm,A_l2);

% adjustment to open the valve in the second stage and can be true in case
the pressures are dropped.

%            if sign(x(9))==1 & x(4)<=0.020
%             mdot_supply_lc=flowThroughOrifice(Ps_lc,P_lc,A_lc);
%             mdot_supply_uc=0;
         % if the velocity of piston is negative then supply is to the
upper
         % chamber

%           else
%             mdot_supply_uc=flowThroughOrifice(Ps_uc,P_uc,A_uc);
%             mdot_supply_lc=0;
%           end

% case C: both ports are blocked by piston
    elseif  x(4)<0.04 & x(4)>=0.035
          mdot_leakage_pst=flowThroughOrifice(P_uc,P_lc,A_up);
          mdot_exhaust_up1=0;
          mdot_exhaust_lp=0;
          mdot_exhaust_up2=0;
          mdot_leakage_ch=flowThroughOrifice(P_lc,Patm,A_l2);
% if the velocity of piston is positive then supply is to the lower
          % chamber
          if sign(x(9))==1 & x(4)<0.025
            mdot_supply_lc=flowThroughOrifice(Ps_lc,P_lc,A_lc);
            mdot_supply_uc=0;
% if the velocity of piston is negative then supply is to the upper
        % chamber
          else
            mdot_supply_uc=flowThroughOrifice(Ps_uc,P_uc,A_uc);
            mdot_supply_lc=0;
          end

% case D; Upper exhaust interacts with upper chamber and lower exhaust is
blocked
    else

          mdot_leakage_pst=flowThroughOrifice(P_uc,P_lc,A_l1);
          mdot_exhaust_up1=0;
          mdot_exhaust_up2=flowThroughOrifice(P_uc,Patm,A_up);
          mdot_exhaust_lp=0;
          mdot_supply_lc=flowThroughOrifice(Ps_lc,P_lc,A_lc);
          mdot_supply_uc=0;
          mdot_leakage_ch=flowThroughOrifice(P_lc,Patm,A_l2);

    end
```

```
% calculation of the state matrix
        A1=[zeros(5) eye(5); -inv(Mass)*Stiff  -inv(Mass)*Damping];

% Calculation of the force matrix
        Force= -inv(Mass)*f;

% Calculation of the displacement and velocity vector
        v= A1*x(1:10) + [0 ;0; 0;0;0 ; Force];

%Calculation of the effective mass flow rate in the upper chamber
        v(11)=(mdot_supply_uc-mdot_exhaust_up2-mdot_leakage_pst);

%Calculation of the effective mass flow rate in the upper chamber
        v(12)=(mdot_supply_lc+mdot_leakage_pst-mdot_exhaust_up1-
              mdot_exhaust_lp-mdot_leakage_ch);

%mass flow rate through upper exhaust port
        v(13)=(mdot_exhaust_up1+mdot_exhaust_up2);

%mass flow rate through lower exhaust port
        v(14)=(mdot_exhaust_lp);

    end
```

```
% This function calculates the flow through an orifice. The input to the%
function is the upstream pressure and downstream pressure and the area of
% the orifice and gives back the mass flow rate for the orifice. The
% function takes into account the possibility of reverse flow. The
function also deals with the choked flow phenomenon
```

Function 'flowThroughOrifice'

```
function massFlowRate=flowThroughOrifice(P1,P2,A)
% global constants

global r R g T C;
ratio=P1/P2;
% if the upstream pressure is higher than the downstream pressure
if ratio>=1
    if ratio>=1.8
        % choked flow
        massFlowRate=(C*A*P1)*(((r*g)/((R*T)))*(2/(r+1))^((r+1)/(r-
                    1)))^0.5;
    else
        %no choked flow
         massFlowRate=(C*A*P1)*(((2*r*g)/(((r-
                      1)*R*T)))^0.5)*((((P2/P1)^(2/r))-
                    ((P2/P1)^((r+1)/r)))^0.5);
    end
% if the upstream pressure isn't higher than the downstream pressure
```

```
else
    if ratio<=(1/1.8)
        % choked flow
        massFlowRate=-(C*A*P2)*(((r*g)/((R*T)))*(2/(r+1))^((r+1)/(r-
                    1)))^0.5;
    else
        %no choked flow
        massFlowRate=-(C*A*P2)*(((2*r*g)/(((r-
                    1)*R*T)))^0.5)*((((P1/P2)^(2/r))-
                   ((P1/P2)^((r+1)/r)))^0.5);
    end
end
```

Vita

Rahul Kadam was born in Nashik, India on March 10, 1981. He graduated with a Bachelor of Science degree in Mechanical Engineering from the University of Pune, India, in 2002. For the next two years, he worked as a Design Engineer for Johnson Controls Inc, Pune. During his Master's studies in Virginia Tech he worked as Graduate Research Assistant in Vibration and Acoustics Labs for the Department of Mechanical Engineering. He will be joining Knowles Electronics in Chicago, Illinois in the Fall of 2006 as a Acoustic and Digital Signal Processing Engineer and will be working on the Miniaturized Microphone and Receiver Development. His areas of interest include Acoustics, Vibrations, Control systems and Digital Signal Processing.